Dissertation

Submitted to the

Combined Faculty of Mathematics, Engineering and Natural

Sciences

of the Ruperto-Carola-University of Heidelberg, Germany

for the Degree of

Doctor of Natural Sciences (Dr. rer. nat.)

Presented by
Anna Piras
March 15th, 2024

Predicting Adsorbent

and

Electronic Properties

of

Graphene-Based Materials

Abstract

Graphene-based materials (GBMs) represent one of the most promising and sustainable alternatives to metal- and silicon-based systems in a plethora of practical applications, from sensing to catalysis. However, the structural variability and lack of standard testing conditions make the efficient development of candidates for specific applications challenging. Nowadays, computational chemistry and materials science can aid experiments by providing crucial understanding of the behaviour of GBMs, but the choice of *in silico* models and theoretical methods is critical to achieve reliable and insightful results. Furthermore, compositional and structural variety and a broad range of sizes of GBMs and their molecular (nano-) variants challenge the applicability of highly accurate *ab initio* methodologies. Clearly, better guidance is needed when deciding how to simulate these functional organic materials accurately and efficiently.

The aim of this thesis is to address this need by studying how the choice of *in silico* model and of the level of theory influence computed properties of GBMs, from adsorption energetics to redox transformations. A large set of computational methods is employed, including semiempirical tight-binding, hybrid, and range-separated density functional theory in finite and periodic settings, symmetry-adapted perturbation theory and many other wavefunction theory implementations, as well as several energy and density decomposition approaches. The results are used to benchmark the performance of these methods, formulate the guidelines for the best-practice techniques, understand the chemical behaviour of the GBMs, and, ultimately, distil the design principles for new and improved materials.

The results and discussion of this work are provided in three chapters:

• In **Chapter 3** we present an extensive benchmarking of diverse theoretical approaches for the adsorption of carbon dioxide on pristine graphene across model sizes and derive a simple yet powerful extrapolation scheme for accurate estimates of the adsorption energies on infinite GBMs.

• In **Chapter 4** we present a study on nitroaromatic compounds adsorbed on diverse graphene-based sensing materials, highlighting the relationship between computed properties and experimentally determined limits of detection, and analysing how the size-dependency of these properties varies with the chemical nature of the adsorbent.

• In **Chapter 5** we transfer the established extrapolation scheme to the redox properties of GBMs, namely, ionisation energy, electron affinity, and redox potentials. Given complex electronic structures of the systems involved, we probe the reliability of single-reference approaches. We also show that, in contrast to adsorption energies, the size-dependencies of these properties are not affected by the material's functionalisation.

This works illustrates that choosing an appropriate theoretical methodology for modelling the chemistry of graphene-based materials is defined by both the balance between cost and accuracy and by the questions the simulations aim to answer.

Kurzzusammenfassung

Materialien auf Graphenbasis (GBMs) sind eine der vielversprechendsten und nachhaltigsten Alternativen zu Systemen auf Metall- und Siliziumbasis für eine Vielzahl praktischer Anwendungen, von der Sensorik bis hin zur Katalyse. Allerdings stellen die strukturelle Variabilität und mangelnde Standardtestbedingungen eine Herausforderung für die effiziente Entwicklung von Kandidaten für spezifische Anwendungen dar. Heutzutage können computergestützte Chemie und Materialwissenschaften Experimente unterstützen, indem sie ein entscheidendes Verständnis für das Verhalten von GBMs liefern, jedoch ist die Wahl der theoretischen Methoden und in silico Modelle entscheidend, um zuverlässige und aufschlussreiche Ergebnisse zu erzielen. Darüber hinaus stellen die Vielfalt der Zusammensetzungen und Strukturen sowie das breite Spektrum an Größen der GBMs und ihren molekularen (Nano-)Varianten eine Herausforderung für die Anwendbarkeit hochpräziser ab initio Methoden dar. Erkennbar ist eine bessere Führung nötig, um zu entscheiden, wie diese funktionellen organischen Materialien akkurat und effizient simuliert werden können.

Ziel dieser Arbeit ist es diesen Bedarf zu decken, indem untersucht wird, wie die Wahl des in silico Modells und des Theorieniveaus die berechneten Eigenschaften von GBMs beeinflussen, von Adsorptionsenergetiken bis zu Redoxumwandlungen. Es wird eine große Zahl computergestützter Methoden angewandt, einschließlich semiempirischer Tight-Binding-, hybrider und reichweiten-separierter Dichtefunktionaltheorie in endlichen und periodischen Umgebungen, symmetrieangepas-ster Störungstheorie und viele andere Implementierungen der Wellenfunktionstheorie, sowie verschiedene Energie- und Dichtebeitragsansätze. Die Ergebnisse werden verwendet, um die Leistung dieser Methoden zu vergleichen, Richtlinien für die besten Verfahren zu formulieren, das chemische Verhalten der GBMs zu verstehen und schließlich die Konstruktionsprinzipien für neue und verbesserte Materialien herauszuarbeiten.

Die Ergebnisse und Diskussionen dieser Arbeit werden in drei Kapiteln dargestellt:

- In **Kapitel 3** präsentieren wir ein umfassendes Benchmarking verschiedener theoretischer Ansätze für die Adsorption von Kohlenstoffdioxid an unverändertem Graphen über verschiedene Modellgrößen hinweg und leiten ein einfaches, jedoch leistungsfähiges Extrapolationsschema für präzise Schätzungen der Adsorptionsenergien an unendlich großen GBMs ab.

- In **Kapitel 4** stellen wir eine Studie über nitroaromatische Verbindungen, die an verschiedenen Graphen-basierten Sensormaterialien adsorbiert werden, vor. Wir zeigen die Beziehung zwischen den berechneten Eigenschaften und den experimentell ermittelten Nachweisgrenzen auf und analysieren, wie die Größenabhängigkeit dieser Eigenschaften mit der chemischen Natur des Adsorbens variiert.

- In **Kapitel 5** übertragen wir das etablierte Extrapolationsschema auf die Redoxeigenschaften von GBMs, namentlich Ionisierungsenergie, Elektronenaffinität und Redoxpotentiale. Angesichts der komplexen elektronischen Strukturen der beteiligten Systeme untersuchen wir die Zuverlässigkeit von Einzelreferenzansätzen. Wir zeigen auch, dass die Größenabhängigkeit dieser Eigenschaften, im Gegensatz zu den Adsorptionsenergien, nicht von der Funktionalisierung des Materials beeinflusst wird.

Diese Arbeit veranschaulicht, dass die Wahl einer geeigneten theoretischen Methode für die Modellierung der Chemie von Materialien auf Graphenbasis sowohl durch das Gleichgewicht zwischen Kosten und Genauigkeit als auch durch die Fragen, die die Simulationen beantworten sollen, bestimmt wird.

Acknowledgements

This thesis would have not been possible without the collective efforts, guidance, and unwavering support of numerous individuals.

Foremost among them is my supervisor, Dr. Ganna Gryn'ova, whose belief in my capabilities and support have been fundamental throughout the four-year journey. Dr. Gryn'ova's guidance not only shaped my scientific work but also made me a more mature and confident scientist. Her encouragement allowed me to explore freely and expand my scientific knowledge, while her constructive critique pushed me to overcome challenges and obstacles.

The completion of this thesis in its present form owes much to the invaluable contributions of Owen Paine, who meticulously proofread, edited, and assisted with formatting. I extend my gratitude to Lukas Lehr for his valuable assistance in writing the German abstract.

A special acknowledgment goes to my research group, a source of support and company throughout my PhD. Dr. Christopher Ehlert deserves special mention for his constant availability for guidance, advice and collaborations. To my fellow PhD students—Stiv, Rostislav, Alessandro, and Gregor—thank you for being both colleagues and friends. Our shared moments have made this journey so much more beautiful and helped me create wonderful memories. The great environment at the CCC group, from interns to postdocs, enriched my PhD, and I extend my appreciation to everyone who has been part of this collective experience. Special thanks are due to the Heidelberg Institute for Theoretical Studies, providing me with the opportunity to pursue my PhD in a beautiful and peaceful environment. I express my deepest gratitude to the personnel, staff, and fellow scientists who contributed to the positive atmosphere and countless memories at the Institute.

To my flatmates, who became my family in Heidelberg, I am profoundly grateful for their support, particularly during the intense period of thesis writing. In Heidelberg I met many wonderful friends, that I want to thank for all the coffee breaks, all the beers, and all the memories. I'm extremely grateful to everyone that listened to my complaints and helped me overcome the stress and difficulties of the PhD, and in particular to Anthony, who always supported me, even when it wasn't easy.

Finally, my deepest appreciation goes to my family, whose belief in me and interest in my work have been constant. Their support has been the a great help for my scientific career, and I am forever grateful.

Contents

List of Figures

List of Tables

List of Acronyms

AIMD Ab Initio Molecular Dynamics.

AO Atomic Orbital.

CBS Complete Basis Set.

CC Coupled Cluster.

CI Configuration Interaction.

COSMO COnductor-like Screening MOdel.

CVD Chemical Vapor Deposition.

DFA Density Functional Approximation.

DFT Density Functional Theory.

DFTB Density Theory Tight-Binding.

DLPNO Domain-based Local Pair Natural Orbital.

DNT 2,4-DiNitroToluene.

DORI Density Overlap Regions Indicator.

EA Electron Affinity.

EDA Energy Decomposition Analysis.

ELF Electron Localisation Function.

FOD Fractional Occupation number weighted Density.

GBM Graphene-Based Material.

GGA Generalised Gradient Approximation.

GO Graphene Oxide.

GQD Graphene Quantum Dot.

GTO Gaussian-Type Orbital.

hBN hexagonal Boron Nitride.

HF Hartree-Fock.

HK Hohenberg–Kohn.

HOMO Highest Occupied Molecular Orbital.

HPLC High-Performance Liquid Chromatography.

IE Ionization Energy.

KMC Kinetic Monte Carlo.

KS Kohn-Sham.

LCAO Linear Combination of Atomic Orbitals.

LDA Local Density Approximation.

LOD Limit of Detection.

LUMO Lowest Unoccupied Molecular Orbital.

MAD Mean Absolute Deviation.

MD Molecular Dynamics.

MO Molecular Orbital.

MTD MeTaDynamics.

NAC NitroAromatic Compound.

NCI Non-Covalent Interaction.

NEB Nudged Elastic Band.

PAH Poly-Aromatic Hydrocarbon.

PBC Periodic Boundary Condition.

PCM Polarisable Continuum Model.

PES Potential Energy Surface.

PT Perturbation Theory.

QTAIM Quantum Theory of Atoms In Molecules.

rGO reduced Graphene Oxide.

RI Resolution-of-the-Identity.

RIJCOSX RI-J for Coulomb integrals and COSX numerical integration for HF exchange.

RMSD Root Mean Square Deviation.

RPA Random Phase Approximation.

SAPT Symmetry-Adapted Perturbation Theory.

SCF Self-Consistent Field.

SMD Solvation Model based on Density.

STO Slater-Type Orbital.

TAO-DFT Thermally-Assisted-Occupation Density Functional Theory.

TNT 2,4,6-TriNitroToluene.

TS Transition State.

vdW van der Waals.

WFT WaveFunction Theory.

XC eXchange-Correlation.

Chapter 1

Introduction

1.1 Background and motivation

Climate change and the depletion of natural resources are among the most pressing challenges facing humankind [1]. Science plays an essential role in ensuring sustainable development towards new and more efficient green technologies and in remediating the anthropological damage to the environment. Nowadays, the majority of industrial processes rely on inorganic materials - metals and silicon - to catalyse reactions, shuttle electrons in energy applications, etc. Yet many metals, particularly rare and noble ones, can be expensive, the raw material is of low availability, and the associated waste can be dangerous and polluting. Furthermore, inorganic compounds present safety hazards since their large scale utilisation requires robust reactors operating under harsh reaction conditions and undergoing frequent maintenance. The use of metalloids, such as silicon, is also not sustainable, because of the limited resources available and the conditions necessary for production and processing. For these reasons, there has been an extensive search for sustainable and industrially-viable alternatives. Examples of such approaches include enzymes [2] and organic molecules [3] to catalyse industrial processes.

Carbon-based materials have been employed across chemical sciences for almost a century. For example, the oxidation of oxalic acid by charcoal was reported in 1926 [4]; the use of graphite as a lubricant is another long-standing example. Diverse carbon allotropes entered the chemical domain with the synthesis of carbon nanotubes [5], which comprise a cylindrical honeycomb lattice of carbon atoms. But the greatest breakthrough in the practical applications of carbon-based materials arrived in 2004 with the first synthesis of pristine graphene [6], a planar hexagonal lattice of sp^2-hybridised carbons. Graphene can be created by mechanically exfoliating graphite or by depositing methane or polycyclic molecules on metallic substrates. Pristine graphene is a zero-gap semiconductor characterised by excellent mechanical properties that can be broadly exploited in materials science and electronics. While its high stability makes it difficult to apply pristine graphene in chemistry, its versatility, which arises from the possibility of functionalising [7] or doping [8] the material (Fig.1.1) and thus generating an entire class of graphene-based materials (GBMs), unlocks an extensive tunability of properties and, therefore, a variety of applications.

GBMs are currently considered to be one of the most promising and sustainable alternatives to metal- and metalloid-based compounds for catalysis, sensing, electronics, and many other applications [9]. The waste from their use in industry is less polluting than that from inorganic alternatives. Moreover, with GBMs not only it is not necessary to extract, purify, and transform metals, but graphene and its derivatives can be obtained from organic raw materials [10], ensuring sustainability of large-scale production and processing.

Depending on the chemical nature of the functionalisation GBMs can be separated into three main classes, which also correspond to their respective synthetic approaches:

- graphene oxide (GO): prepared by oxidation and exfoliation of graphite, it contains several oxygenated functional groups, such as epoxides and hydroxyls. The aromaticity, with respect to pristine graphene, is partially lost because of the presence of sp^3-hybridised carbons, defects, and vacancies;

- heteroatom-doped graphene: usually contains N, P, S and/or B atoms that are incorporated during the synthesis; their presence alters the electronic and chemical properties of the

1
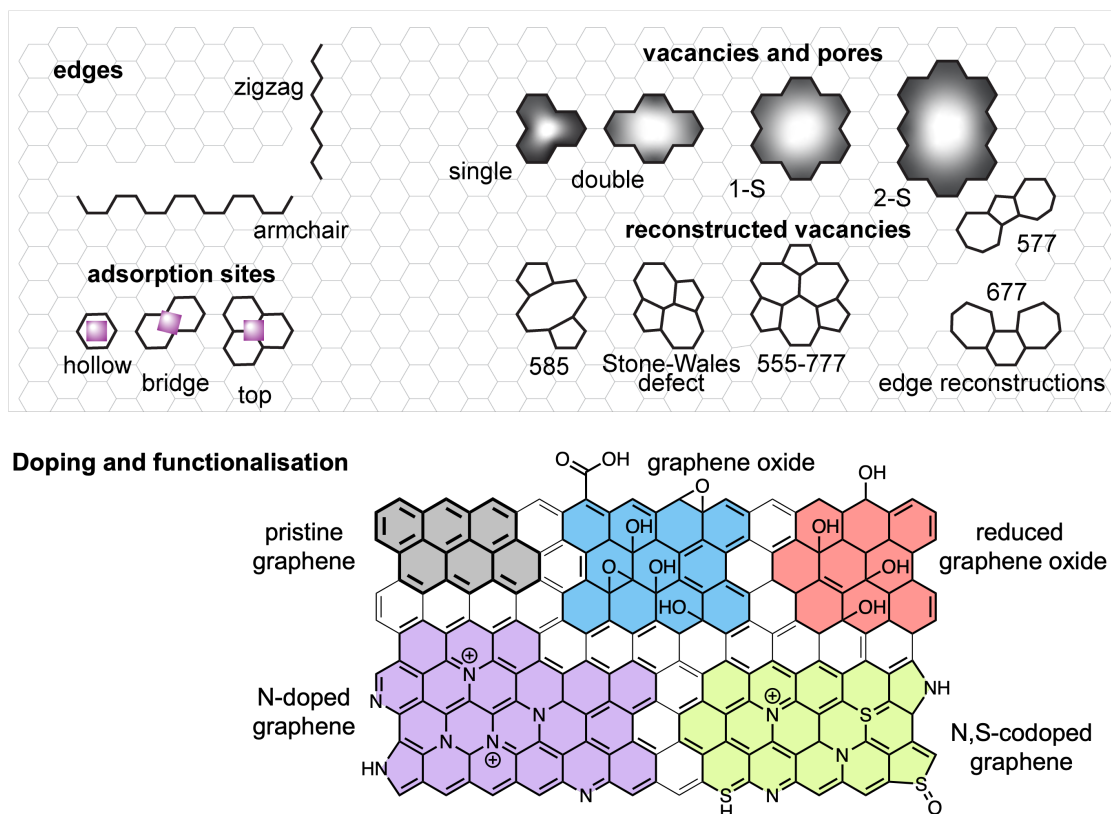
Figure 1.1: Examples of graphene-based materials and their many modifications.

graphene sheet;

- covalently functionalised graphene: functional groups, such as sulfonate, are attached to the surface during synthesis.

The process of obtaining GO *via* oxidation and exfoliation of graphite is a top-down approach. The exfoliation is eased by the repulsion between oxygenated groups. The oxidation can be performed with sodium nitrate, sulfuric acid, and potassium permanganate (the so-called Hummers and Offeman method [11]), sulfuric and/or nitric acids with potassium chlorate (the Staudenmaier method [12]), or nitric acid and sodium chloride oxide (the Brodie method [13]). Oxidation introduces functional groups along with various defects and vacancies. The most accurate model of GO, capturing the distribution of oxygenated groups and defects, is the Lerf-Klinowski model [14] (see Figure 1.2).

Introducing heteroatoms into the lattice through doping induces polarisation of the carbon network and affects various physico-chemical properties of the material. Among many approaches to the synthesis of doped graphene [15], chemical vapor deposition (CVD) is one of the most widely used methods. It is a bottom-up synthesis of graphene that allows controlling the quantity of heteroatoms by depositing methane and dopant-containing gas (e.g., ammonia to obtain N-doped GBMs) on a metallic film in the desired stoichiometric ratio. Alternative synthetic procedures involve substitution of carbon atoms in the lattice by annealing or plasma treatment in the presence of a gas containing dopant atoms.

Functional groups can be attached to the surface of graphene to increase its solubility, to introduce new properties (e.g., adding chromophores for colour), and/or to open the band gap of the material. There are two main approaches to perform covalent functionalisation of graphene [7]:

- free radicals (e.g., obtained by heating diazonium salts of aryls), or dienophiles (e.g. azomethine ylide), attack the double bonds of a pristine graphene lattice;

- organic functional groups are attached to the oxygenated groups of GO, e.g., *via* formation of amides if the functional group to be attached contains a terminal amine.
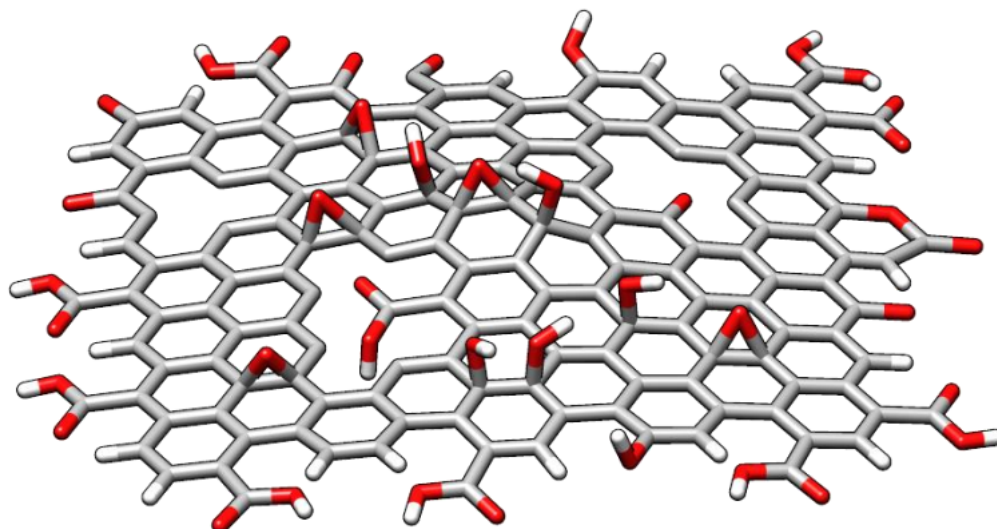
Figure 1.2: The Lerf-Klinowski model of graphene oxide.

GBMs can include a single or a few layers. They can also be distinguished by the size of individual layers, as follows:

- infinite (extended) GBMs, represented by a repeating primitive unit cell;

- fragments of graphene under 100 nm in diameter, considered to possess "molecular nature". Depending on the field of research, application, etc., these molecular graphene fragments are variously called graphene nanoparticles, graphene nanoflakes, nanographenes, graphene quantum dots (GQDs), and polyaromatic hydrocarbons (PAHs).

The ability to tailor graphene's properties and to synthesise new GBMs is an immense advantage of this class of materials. However, it hinders efficient development of an optimal material for a specific application, given the excess of possible graphene derivatives [16]. Furthermore, the lack of standard testing and characterisation approaches [17, 18] complicates the comparison between measured performance indicators reported by different research laboratories. Establishment of guidelines, insights, and descriptors predictive of GBMs' performance is crucial to enable fast and efficient development of new materials. Computational chemistry offers a solution to the lack of more standardised data and the insufficient quantity of experimental results. Increase in computing power and improvement of algorithms continuously push the capabilities of *in silico* modelling. Simulations have proven an efficient tool to design materials for specific applications, to predict their properties, and to screen large databases of potential candidates. However, the accuracy and reliability of *in silico* predictions greatly depend on the computational protocol employed; for this reason, we cannot consider computational chemistry a black box, but have to carefully think about our choices of methods and models.

1.2 State of the art

Computational chemistry has been used extensively to study GBMs to resolve experimental challenges and provide design guidelines. It helped gain insights into how GBMs are synthesised, understand their structures, predict their properties, and design new derivatives for specific applications *in silico*[19, 20, 21].

Simulating GBMs synthesis is challenging because of the complexity of both the material's structure and its growth mechanism. The growth of graphene on copper by CVD was studied with molecular dynamics (MD) to identify the key mechanistic steps and understand how to tune the temperature and deposition rate to increase the quality of the GBM[22]. A similar study of CVD-based graphene synthesis, in which the substrate was semi-molten copper, compared the results of classical and *ab initio* molecular dynamics (AIMD), illustrating the general agreement between the two approaches and the role that simulations can play in finding ideal conditions for a controlled

synthesis of graphene[23]. Experiments and molecular dynamics simulations on the growth of graphene from carbon nanoclusters, combined with the density functional theory (DFT) modelling of the adsorption of the initial clusters on the substrate, in this case strontium titanate, elucidated the growth mechanism and identified other materials that can be grown in a similar manner [24]. Kinetic Monte Carlo (KMC) was employed to model the growth of graphene on iridium and to identify a kinetic-dominated mechanism for the growth of N-doped graphene on copper [25]. Effects of pyrolysis and annealing on the formation of graphene oxide were also investigated *in silico*. Given the evolution of the chemical nature and the formation of defects and vacancies under extreme conditions, a reactive force field (ReaxFF) had to be used in molecular dynamics simulations [26]. DFT was employed to elucidate the mechanism and identify the structure of reduced graphene oxide (rGO), obtained *via* reduction of GO [27].

Precise composition and structure of GBMs are rarely known in experiment, because defects and impurities are introduced during the synthesis and detailed characterisation of the material is challenging. Simulations can be used to predict stable structures and rationalise experimental data. Yet, when designing models for *in silico* studies, one by necessity introduces bias as to which functional groups to place, and where; manual construction of various structural possibilities is long and laborious. For this reason, several methods for automatic generation of GBM structures have been developed. Random forest algorithm using a small set of features corresponding to chemical functionalities has been successfully employed to generate and analyse diverse graphene oxide structures [28]. In the case of GO nanoflakes, machine learning allowed finding 25 archetypal structures that capture full compositional and structural diversity and variability of this material [29]. Another approach to generate GO structures of different complexity and with defined features is the modular tiling strategy, which creates large structures from small subunits [30]. Other tools to generate a variety of GBMs, including features such as covalent functionalisation and vacancies, exist as well [31]. Yet another key bias introduced in materials simulations is the choice of the model - infinite/periodic *versus* finite (Fig.1.3). While periodic models are more realistic, it might sometimes be desirable to work with simple finite models, either to gain deeper insights into particular properties, or to perform more accurate and, consequently, more expensive computations. Molecular (finite) models are sometimes used to model extended systems simply because particular computational methods are not yet developed or implemented for periodic simulations [21, 19].
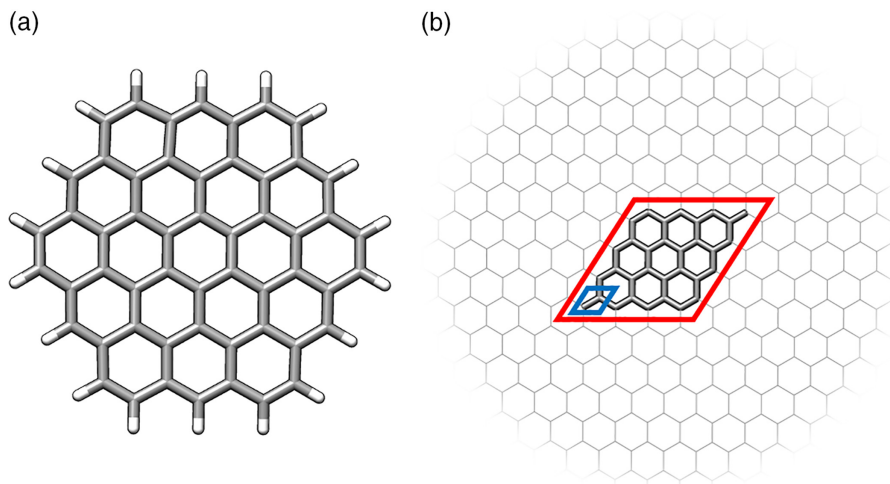
Figure 1.3: Examples of graphene models: (a) a circumcoronene molecule, used as a nanoflake model for pristine graphene; (b) a periodic model of pristine graphene with a supercell of 32 carbon atoms (in red) obtained from a primitive unit cell containing two carbon atoms (in blue). Taken from Ref. [21]

.

Computational modelling of GBMs allows simultaneous investigation of their chemistry and finding descriptors with predictive power, and therefore facilitates the design of GBMs for target applications, such as sensing [21], energy storage and conversion [32, 33], filtering [34], and catalysis [35, 36]. For example, computations of optical and electric field properties, *i.e.* electric field

enhancement and the effective localization area of the field, were employed to design graphene-based plasmonic hot spots (nanostructures with strong localised electromagnetic fields) [37]. These systems are able to detect single molecules with a performance similar to metal-based compounds.

Computational chemistry can be used to evaluate an extensive set of material properties, from enthalpy of formation to band gap and beyond. In this thesis, we focus on the following properties, relevant to the application of GBMs as electrochemical sensors [21] and catalysts [38, 39]:

- interaction energy (E_{int}): contribution to the total energy of an A-B complex due to an interaction between A and B;

- electron affinity (EA): amount of energy released when an additional electron is attached to a molecule or an atom [40];

- ionization energy (IE): amount of energy required to remove an electron from a molecule or an atom [40];

- solvation free energy (ΔG_{Solv}): the change in free energy due to a molecule or ion being transferred from the gas phase into solvent [40].

In this thesis, several Chapters describe the non-covalent interactions (NCIs) between a graphene-based material and a small molecule, *i.e.*, CO_2 (**Chapter 3**) and nitroaromatic compounds (**Chapter 4**). Quantification and analysis of non-covalent interactions has been extensively addressed by the computational chemistry community, yet a complete and accurate understanding of these forces is not easily achieved [41]. This is because computing the interaction energy itself is often insufficient to understand the chemical behaviour or to design better materials; the nature of these interactions, their geometrical features, and the ways to tune them can be just as crucial. A number of computational studies on the non-covalent interactions involving GBMs have been published in the last 15 years. Various flavours of DFT (see **Chapter 2**) were used to study interactions between GBMs and nitrocompounds [42, 43], benzene [44], drug candidates [45], and volatile organic compounds [46]. Given the variety of computational approaches applicable to the quantification of interaction energy, benchmarking studies are critical to select appropriate *in silico* methodology. For example, a series of increasingly large graphene nanoflakes were used as models of infinite graphene, and their interaction with benzene was computed with different DFT methods [47]. The PW6B95-D4 hybrid meta-GGA functional enabled the reproduction of experimental data and, as could be expected, large models better represented infinite graphene [47]. Lazar *et al.* [48] compared DFT, wavefunction theory (WFT), and empirical approaches for computing the interaction energies for a set of organic molecules, confirming that accurate computational methods, such as *ab initio* molecular dynamics employing the non-local optB88-vdW functional, can reproduce experimental adsorption enthalpies. The authors also showed that these interactions are always dominated by dispersion, even in the case of polar adsorbates. When modelling adsorption, it is important to identify the adsorption site on the extended material [21]. This can be achieved by relaxing the structure of the complex [46, 42, 47] or with a more extensive search of the adsorption site, e.g. through *ab initio* molecular dynamics [48]. Furthermore, in order to better understand the nature of the adsorption, methods for decomposing energies, densities, and wavefunctions, such as Quantum Theory of Atoms In Molecules [45] or Symmetry-adapted perturbation theory (SAPT) [48] (**Chapter 2**), can be employed.

Redox properties, such as IE and EA, are crucial to understand the behaviour of GBMs in electrochemistry [49], sensing [21], energy storage and conversion [50], as well as under extreme conditions such as in the interstellar space [51]. In line with the topic of this thesis, several studies demonstrated how the size of the GBM affects its redox properties [52, 53, 54, 55]. Chai *et al.* [52] used thermally-assisted-occupation density functional theory (TAO-DFT) to compute singlet-triplet gaps, IEs, and EAs for increasingly large circular graphene nanoflakes, up to hundreds of atoms, showing the convergence of the electronic properties and the appearance of polyradicalic character with increasing size of the nanoflake. The same approach was used to study triangulenes (triangle-shaped graphene nanoflakes) [53], showing similar convergence for IE and EA and an even stronger polyradical character than in the circular counterparts. The latter was attributed to the fact that active orbitals tend to become more localised at the periphery of the molecules when their size increases. Azulene-based allotropes of graphene containing 5-membered unsaturated rings arranged in a rhomboidal shape also show a decrease in the singlet-triplet gap and IP and increase in EA with the increasing size of the molecule [54]. A good agreement between computed

(SMD/B3LYP/6-31G+(d) level of theory) and experimental redox potentials was achieved for diverse nanoflakes across a wide range of external potentials [55].

Finally, in many practical applications, such as electrochemical sensing, the GBM is solvated (e.g., in water), and the corresponding effects have to be included in *in silico* models if the goal is to reproduce experimental adsorption energies or redox properties [21]. The solvent can be treated implicitly as a continuum, or explicitly with a relatively small number of solvent molecules (see **Chapter 2**). The former approach can be used to approximate experimental conditions in a cost-efficient manner [56], while the latter affords a more realistic representation but often comes at a of prohibitive computational cost [57].

1.3   Aims and scope

The central goal of this thesis is to aid a more efficient development of high-performance graphene-based materials for electrochemical sensing and, more generally, environmental remediation. Key to these applications are the interactions of GBMs with common pollutants (such as carbon dioxide and nitroaromatic compounds), as well as their redox properties. Specifically, we investigate how computable properties can be employed as descriptors to qualitatively or quantitatively predict the performance of GBMs and deduce the key structure-property relationships facilitating rational design of these materials. Correspondingly, significant research effort in this thesis is dedicated to establishing reliable yet affordable computational methodologies that provide in-depth insights into the pertinent physico-chemical properties of the GBMs. To fulfil this aim, a broad range of computational techniques, from semiempirical tight-binding and DFT to symmetry-adapted perturbation theory, was applied to investigate graphene and its many variants featuring functionalisation and (co-)doping, across a series of finite and periodic models.

1.4   Content of the thesis

This thesis is organised across the following chapters:

Chapter 2: Theory framework presents an overview on the theories upon which the methods used in this thesis are based.

Chapter 3: Carbon dioxide on graphene describes an extensive benchmarking study performed to simulate the adsorption of carbon dioxide on graphene nanoflakes of different shapes and sizes and on periodic graphene models. The Chapter also presents an extrapolation scheme for predicting adsorption energies at low cost but with high accuracy.

Chapter 4: Adsorption of nitroaromatic compounds on graphene-based materials provides insights into the adsorption of nitroaromatic contaminants on a diverse set of graphene-based materials in the context of their use in electrochemical sensors. The Chapter explores the effect of chemical functionalisation, model size, and theoretical methodology on the computed properties.

Chapter 5: Redox properties of graphene-based materials shows how electronic properties, such as IE, EA, and solvation energies depend on the model size and chemical composition of the material. The Chapter also explores how the quality of the electronic structure (*i.e.*, the extent of spin contamination) in conjunction with the chosen single-reference methodology affects computed properties.

Chapter 6: Conclusions summarises the findings of this thesis and outlines the future perspectives in this field of science.

While a general introduction into the topic of graphene-based materials and an overview of key modelling approaches are provided in the **Introduction** above and in **Chapter 2** below, **Chapters 3**, **4**, and **5** include dedicated introductory, prior art, and methodological sections that relate to their specific research areas.

Chapter 2

Theoretical framework

Modelling methods and their underlying theoretical frameworks, used in computational chemistry, must be appropriate, *i.e.*, afford balance between accuracy and cost, to the tackled scientific problems and investigated chemical systems. In this thesis, we aim to predict accurately and efficiently and to analyse in an insightful manner the adsorbent and electronic properties of graphene-based materials. The nature of the studied properties requires an explicit treatment of electrons, afforded by *ab initio* electronic structure theory methods (Section 2.1). Since investigated phenomena occur in the ground state, here we focus on the time-independent implementations of the Hartree-Fock (Section 2.1.2), post-Hartree-Fock (Section 2.1.3), and DFT (Section 2.1.3). The adsorption of small molecules on graphene or its derivatives entails non-covalent interactions, which need to be carefully evaluated and analysed (Section 2.3). The choice of the adsorption site is critical, necessitating detailed exploration of the potential energy surface (PES) of the system (Section 2.2). The inclusion of solvent effects, which are present in most real-world applications, is equally important (Section 2.4). In the case of GBMs, another challenge arises from the choice between the finite (molecular) and periodic (infinite) models. The latter represent extended materials more realistically, but pose significant computational challenges, *i.e.*, introduction of the periodic boundary conditions and limited selection of implementations (Section 2.1.5). In this Chapter, the key aspects of these theoretical frameworks and their implementations are concisely introduced and discussed in the context of GBMs modelling.

2.1   Electronic structure theory

2.1.1   Wavefunction theory

The probability of finding a particle in a given position in space, as well as information about the state of the particle, can be obtained from the time-dependent Schrödinger equation:

$$\hat{H}\Psi(t) = i\hbar\frac{d}{dt}\Psi(t), \tag{2.1}$$

where $\hat{H}$ is the Hamiltonian operator, Ψ the wavefunction, t time, and $\hbar$ the Plank constant.

  The Born postulate states that $|\Psi(x,t)|^2$ represents the probability that the particle is in the position defined by x at a time t. In practical chemical scenarios, to simplify the calculations, only the solutions of Eq.(2.1) that can be written as

$$\Psi(x,t) = f(t)\psi(x) \tag{2.2}$$

are considered. $f(t)$ is a function of time and $\psi(x)$ represents the spatial amplitude of the wavefunction.

  From Eq.(2.2), in a one-dimensional system, we obtain:

$$f(t) = e^{-\frac{2\pi i E t}{h}}, \tag{2.3}$$

and therefore the time-dependent wavefunction is

$$\Psi(x,t) = e^{-\frac{2\pi i E t}{h}}\psi(x), \tag{2.4}$$

where E represents the total energy. The states described by this equation are called stationary states, because the probability density does not depend on time:

$$|\Psi(x,t)|^2 = |\psi(x)|^2 . \tag{2.5}$$

We can rewrite the Schrödinger equation as

$$E\psi(x) = \left[-\frac{h^2}{8\pi^2 m}\frac{d^2}{dx^2} + V(x)\right]\psi(x) = \hat{H}\psi(x) \tag{2.6}$$

where $\hat{H}$ is the Hamiltonian operator, $V(x)$ the potential energy, and $\psi(x)$ is the wavefunction.

The eigenvalues of the Hamiltonian operator (see Eq.(2.6)) are the possible values of the system's energy, while the eigenfunctions represent the wavefunctions ψ. Considering the Born-Oppenheimer approximation, that allows decoupling electronic and nuclear motion, the electronic Hamiltonian is:

$$\hat{H}_{el} = \hat{T} + \hat{V}_{ne} + \hat{V}_{ee}, \tag{2.7}$$

where

$$\hat{T} = -\frac{h^2}{8\pi}\sum_{\alpha}\frac{1}{m_{\alpha}}\hat{\nabla}_{\alpha}^2, \tag{2.8}$$

$$\hat{V}_{ne} = \sum_{\alpha}\sum_{i}\frac{z_{\alpha}e'^2}{r_{i\alpha}}, \tag{2.9}$$

$$\hat{V}_{ee} = \sum_{j}\sum_{i>j}\frac{e'^2}{r_{ij}}. \tag{2.10}$$

Here, $\hat{\nabla}$ is the Laplacian operator, m_{α} the mass of the atom α, z_{α} the atomic number of the atom α, $r_{i\alpha}$ the distance between electron i and nucleus α, r_{ij} the distance between electron i and electron j, and e' the electron charge. The nuclear energy, constant for a fixed nuclear configuration, is added to the electronic energy to arrive at a purely electronic Schrödinger equation:

$$\hat{H}_{el}\psi_{el} = E_{el}\psi_{el}. \tag{2.11}$$

2.1.2   The Hartree-Fock method

The Hartree method is based on the assumption that the electronic wavefunction can be expressed as a product of one-electron molecular orbitals (MOs, ϕ), each dependent on the coordinates of a single electron (r_i):

$$\Psi(r_1, r_2, ..., r_n) = \prod_{i=1}^{n}\phi_i r_i. \tag{2.12}$$

However, this formalism violates the Pauli exclusion principle, which states that the many-electron wavefunction must be antisymmetrical with respect to the exchange of two particles. To resolve this problem, the Hartree-Fock (HF) method was developed. In it, the total wavefunction is approximated as a Slater determinant Φ:

$$\Phi = \Psi(r_1, r_2, ..., r_n) = \frac{1}{\sqrt{n!}}\begin{vmatrix} \phi_1(e_1) & \cdots & \phi_n(e_1) \\ \vdots & \ddots & \vdots \\ \phi_1(e_n) & \cdots & \phi_n(e_n) \end{vmatrix} = |\phi_1, \cdots, \phi_n|. \tag{2.13}$$

With this approach, the Hamiltonian operator can be separated into n one-electron operators, where n is the number of electrons in the system, as follows:

$$\hat{H}_{el} = \sum_{i=1}^{n}(-\frac{1}{2}\hat{\nabla}_i^2 - \sum_{A}^{nuclei}\frac{z_A}{r_{iA}}) + \sum_{i<j}\hat{V}_{i,j} + V_{nn} = \sum_{i}\hat{h}(i) + \sum_{i<j}\hat{V}_{i,j} + V_{nn}, \tag{2.14}$$

where $\hat{V}_{i,j}$ is the two-electron potential energy operator, $\hat{h}(i)$ is the one-electron Hamiltonian operator, and V_{nn} is the nuclear-repulsion potential, constant for a fixed set of nuclear coordinates.

The Hartree formalism of the one-electron Schrödinger equation (Eq.(2.15)) can be written as:

$$\hat{h}_i\phi_i = \epsilon_i\phi_i. \tag{2.15}$$

The corresponding molecular orbitals, denoted HF-MOs, are the eigenfunctions of the Fock operators ($\hat{f}_i$), which are one-electron operators similar to $\hat{h}_i$ in the Hartree formalism:

$$\hat{f}_i = -\frac{1}{2}\hat{\nabla}_i^2 - \sum_{nuclei}^{j} \frac{z_j}{r_{ij}} + \hat{V}_i^{\mathrm{HF}}. \tag{2.16}$$

Here, V_i^{HF} is the mean potential term including the electron exchange contribution. It includes the Coulomb operator $\hat{J}_i$, which describes the repulsion between two electrons in the orbital j, and the exchange operator $\hat{K}_i$ that describes the electron exchange contribution arising from the Pauli exclusion principle.

A set of eigenfunctions corresponding to the MOs is obtained through a self-consistent field (SCF) procedure:

  i. A set of guess MOs is used to obtain the corresponding set of Fock operators;

 ii. The obtained Fock operators are used to compute a new set of molecular orbitals;

iii. The procedure is reiterated until the calculated energy is converged, *i.e.*, does not change beyond a chosen threshold value (convergence criterion).

2.1.3 Post-Hartee-Fock methods

In the HF method the electron-electron repulsive potential is approximated by a mean potential, the Fock operators are one-electron operators, and the wavefunction is approximated as a Slater determinant. These approximations result in the lowest achievable Hartree-Fock energy of the system (the HF limit) still being higher than the true, or exact energy. The difference between these two values, *i.e.*, the error due to the approximations in the HF method, is called electron correlation:

$$E_{\mathrm{corr}} = E_{\mathrm{true}} - E_{\mathrm{HF}}. \tag{2.17}$$

The value of E

The electron wavefunction is not a physical observable; it is a function of both spatial and spin (angular momentum) coordinates:

$$\Psi(x,y,z,\sigma) = \psi(x,yz)\alpha(\sigma), \tag{2.18}$$

or

$$\Psi(x,y,z,\sigma) = \psi(x,y,z)\beta(\sigma), \tag{2.19}$$

where $\psi(x,y,z)$ is the spatial orbital, α and β are spin eigenfunctions, and σ is the spin variable.

In contrast, the electron density ($\rho(r)$) is a physical observable, defined as

$$\int \rho(\overrightarrow{r})d\overrightarrow{r} = n, \tag{2.20}$$

where n is the number of electrons in the system, and $\overrightarrow{r}$ are their positions. The relative simplicity and physical interpretability of the electron density prompted the development of DFT, which, is based upon the two Hohenberg-Kohn theorems:

HK 1 Proof of existence: The external potential, and therefore the total energy of the system, is a unique functional of the electron density. As a corollary, the ground state density determines the potential and thus all the properties of the system.

HK 2 Variational principle: This functional will yield the lowest bound for the ground-state energy of the system if and only if the input electron density is the true ground state density.

The first theorem can be expressed as follows:

$$E_0 = E_\nu\left[\rho_0\right] = T\left[\rho_0\right] + E_{ee}\left[\rho_0\right] + E_{\mathrm{ext}}\left[\rho_0\right], \tag{2.21}$$

where T is the kinetic energy, E_{ee} is the repulsion between the electrons, and, in the case of an isolated and field-free molecule, E_{ext} corresponds to the interaction between electrons and nuclei.

The last term is constant for a fixed nuclear configuration and can be evaluated exactly. The other two terms are independent of the system and are collected into the Hohenberg-Kohn (HK) functional:

$$E_{\text{HK}}[\rho_0] = T[\rho_0] + V_{\text{ee}}[\rho_0].$$

(2.22)

The explicit form of the functional for the kinetic energy is not known. The functional for the electron-electron interaction can be separated into two contributions:

$$V_{\text{ee}}[\rho] = J[\rho] + E_{\text{ncl}}[\rho],$$

(2.23)

where $J[\rho]$ is the classical and $E_{\text{ncl}}[\rho]$ the non-classical parts of the contribution.

The Kohn-Sham approach does not regard the treatment of wavefunctions or electronic orbitals, but the resolution method treats a fictitious system, composed by n non-interacting electrons. These electrons experience the same external potential $v(\overrightarrow{r})$, such that the fictitious electron density $\rho_s(\overrightarrow{r})$ equals the ground state density for the real system $\rho_0(\overrightarrow{r})$. With this approximation, the Hamiltonian can be expanded as the sum of one-electron Kohn-Sham operators $\hat{h}_i^{\text{KS}}$. The eigenfunctions of these operators (χ_i^{KS}) are the spatial parts of the Slater determinant of the Kohn-Sham spin-orbitals; the corresponding eigenvalues are the Kohn-Sham orbital energies ϵ_i^{KS}

$$\hat{h}_i^{\text{KS}}\chi_i^{\text{KS}} = \epsilon_i^{\text{KS}}\chi_i^{\text{KS}}.$$

(2.24)

The difference between the kinetic energy of the real system and the reference system (described exactly by the Kohn-Sham treatment) is given by $\Delta\bar{T}[\rho]$. The sum of $\Delta\bar{T}[\rho]$ and $E_{ncl}[\rho]$, which represent the non-classical part of the electron-electron interaction (see Eq.(2.25)), corresponds to the intrinsic error of the Kohn-Sham method and is called the exchange-correlation energy, E_{XC}:

$$E_{\text{XC}} = \Delta\bar{T}[\rho] + \Delta\bar{V}_{\text{ee}}[\rho].$$

(2.25)

Unfortunately, the form of the exact exchange-correlation functional remains elusive, resulting in a plethora of density functional approximations (DFAs). These methods are usually classified according to the Jacob's ladder [61], which ranks DFAs by how elaborately they represent the E_{XC} and how close the accuracy of the resulting energy is to the chemical accuracy (see Fig.2.1). Computational cost also increases from the bottom to the top of this ladder.
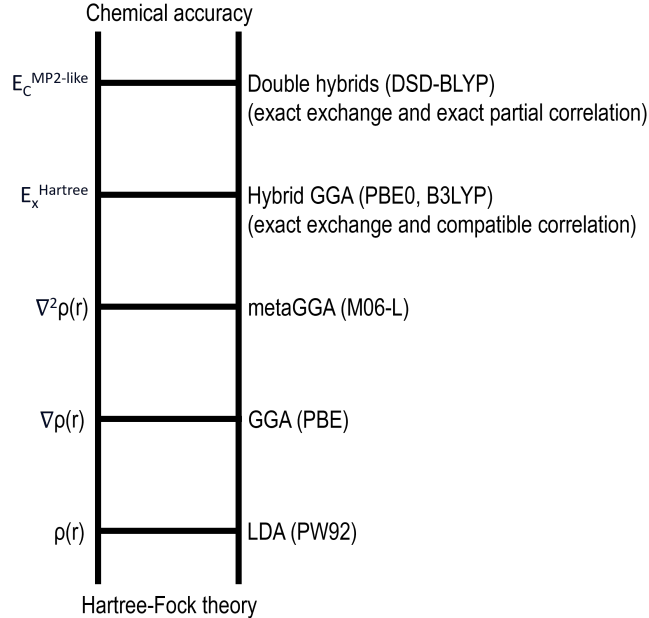
Figure 2.1: Jacob's ladder for the five rungs of DFAs [61]. Common DFT functionals for each level are shown on the right, additional information that is included to the functional increase its accuracy is shown on the left of the ladder.

The five rungs on the Jacob's ladder correspond to:

- local density approximation (LDA): the system is divided into infinitesimal volumes, inside of which the electron density is treated as constant. Only the electron density ($\rho(r)$) is included in the functional. Within this approach, the exchange term has an analytical expression and the correlation term is fitted to experimental data;

- generalised gradient approximation (GGA): to account for the rapid variation of the electron density, the gradient of ρ is introduced;

- meta-GGA: a second derivative of the electron density reflecting the dependence on the kinetic energy density (the Laplacian) is introduced;

- hybrid methods: a fixed fraction of the exact Hartree-Fock exchange is added to pure LDA, GGA, or meta-GGA functionals;

- double hybrid: on top of the exact Hartree-Fock exchange, a component of perturbation theory-like correlation is introduced. Range-separated functionals can be thought of as mixtures from higher rungs of the ladder. In them, the exchange functional is flexibly partitioned into DFT exchange at short-range and HF exchange at long-range with respect to the inter-electronic separation.

In this thesis, to assess the performance of various electronic structure theory methods for evaluating adsorbent and redox properties of GBMs, DFAs from various rungs were tested: GGA (PBE), hybrid-GGA (B3LYP, PBE0, TPSSh, M062-X), double hybrid (DSD-BLYP), and long-range-corrected (ωB97X-D). The choice of the functional was guided by the balance between accuracy and computational cost.

Dispersion constitutes a significant, at times even the dominant part, of the non-covalent interactions between neutral compounds [62]. However, it has been historically neglected in DFT, and a number of approaches has been developed in the past 20 years to account for dispersion directly in the functional (non-local DFAs), either during the parametrisation (Minnesota functionals) of the functional, or as *a posteriori* empirical correction to it. DFT-Dx corrections, developed by the Grimme group, are among the most famous such corrections. In DFT-D3 [63], dispersion energy is expressed as:

$$E_{\text{disp}} = -\frac{1}{2} \sum_{i=1}^{N_{\text{atoms}}} \sum_{j=1}^{N_{\text{atoms}}} \sideset{}{'}\sum_{\mathbf{L}} (f_{d,6}(r_{ij,L}) \frac{C_{6ij}}{r_{ij,L}^6} + f_{d,8}(r_{ij,L}) \frac{C_{8ij}}{r_{ij,L}^8}), \qquad (2.26)$$

where i and j are two atoms of the system, L is the reference cell, f a damping function, and C is a dispersion coefficient. The last two parameters are obtained empirically and optimised for different functionals.

While most DFAs come at a lower computational cost than the post-HF methods, they still scale up with the size of the system, becoming unaffordable in practical terms for systems containing hundreds of atoms. The so-called semiempirical methods address this limitation, albeit often sacrificing accuracy for efficiency. They are still based on the HF formalism, but involve further approximations and include parameters obtained by fitting to empirical data. A sub-class of semiempirical methods is represented by tight-binding methods, in which electrons are considered tightly bound to the atoms to which they formally belong. In the case of density functional tight-binding (DFTB), the total energy is expressed in terms of density fluctuations around superposition of the reference atomic densities. GFN2-xTB [64] is one such method, and is used extensively in this thesis. This method is parameterised to account for electrostatic, dispersion, and exchange-correlation contributions, and, in contrast to other tight-binding methods, does not rely on parameters obtained from classical mechanics. The GFN2-xTB energy is expressed as

$$E_{\text{GFN2-xTB}} = E_{\text{rep}} + E_{\text{disp}} + E_{\text{EHT}} + E_{\text{IES+IXC}} + E_{\text{AES}} + E_{\text{AXC}} + G_{\text{FERMI}}, \qquad (2.27)$$

where E_{rep} is the repulsiion energy, E_{disp} the dispersion energy (calculated using the DFT-D4 scheme), E_{EHT} the energy given by the extended Hückel theory, $E_{\text{IES+IXC}}$ the energy of the isotropic electrostatics and exchange-correlation, E_{AES} the anisotropic electrostatic component, E_{AXC} the anisotropic exchange-correlation, and G_{FERMI} the entropic contribution to the electronic free energy at finite electronic temperature due to Fermi smearing. A typical DFTB computation is orders of magnitude faster than DFT and is thought to yield results of comparable accuracy for geometries and some of the properties.

2.1.4   Basis sets

A molecular orbital (one-electron wavefunction) can be approximated within the basis set as a linear combination of functions, called *basis functions*:

$$|\phi_i\rangle \approx \sum_{\mu=1}^{k} c_{i\mu}\chi_\mu, \tag{2.28}$$

where ϕ_i is the orbital, χ_μ are the basis functions, and $c_{i\mu}$ their coefficients.
Common basis sets can be classified according to the nature of χ_μ as follows:

- a linear combination of atomic orbitals (LCAO) is the most common choice for quantum chemistry calculations on molecules.

- plane waves are typically used for treating periodic systems (see Section 2.1.5).

- a real space approach that allows efficiently parallelising the DFT computations.

In the LCAO approach, basis functions are typically constructed as linear combinations of either the Gaussian-type orbitals (GTOs), or, less commonly, the Slater-type orbitals (STOs). In a so-called minimal basis, a single basis function is used for each orbital. Such a minimal description naturally lacks accuracy, and therefore it is typically extended with more basis functions added per atom and furnished with various corrections. The latter include diffuse functions, which add flexibility to the electron density far from the nucleus (and are therefore crucial when describing non-covalent interactions and anionic species), and polarisation and high angular momentum functions to add flexibility in the proximity of the nuclei.

The basis sets employed in this thesis in conjunction with the DFT computations, namely def2-TZVP and def2-QZVPPD, belong to the Karlsruhe (or Ahlrichs) family [65]. These basis sets are built from contracted GTOs and belong to the so-called split-valence basis sets. In such basis sets, the inner electrons are modeled with effective core potentials, reducing the basis set size and accounting for scalar relativistic effects. Valence electrons occupy orbitals represented by one or more functions each. The number of these basis functions, Z (or ζ), can be single, double, triple, quadruple, etc.; e.g., def2-TZVP is a triple-zeta valence basis set. Here, P and D represent sets of polarisation and diffuse functions added, respectively. In general, these basis sets are characterised by rapid convergence of energy, applicable to the full periodic table, considered well balanced, and can also be coupled with the so-called auxiliary basis sets that further speed up computations.

A separate family of basis sets is conventionally used in conjunction with the symmetry-adapted perturbation theory computations. SAPT results are known to be highly sensitive to the basis set [66], and in this thesis the so-called "bronze" level of SAPT, *i.e.*, SAPT0/jun-cc-pVDZ, is used. The jun-cc-pVDZ belongs to the so-called "calendar" version of Dunning's correlation consistent basis sets [67], developed by Truhlar [68]. It is a double-zeta basis set, from which the redundant functions have been removed to increase efficiency, while diffuse and polarisation functions were adjusted. Specifically, H and He atoms have no diffuse functions, while the highest angular momentum diffuse functions are removed for all other elements.

Semiempirical methods, such as GFN2-xTB [64], also come with a dedicated basis set, which is a minimal valence basis set of atom-centered contracted Gaussian functions approximating Slater functions (STO-nG). Polarisation functions for most main group elements (typically, second row or higher) are added. In the case of a dimer, if the monomers do not have associated infinite basis sets, more basis functions are employed to describe the dimer than used for each of the monomers. Therefore, the basis set of the dimer is more flexible, causing artificial lowering of the energy.

2.1.5   Periodic computations

Periodic computations refer to a set-up describing ordered infinitely extended two- or three-dimensional systems, such as graphene. In this set-up, a primitive unit cell is repeated in space, creating the lattice (see Figure 1.3). All points in the lattice are identified by a lattice vector; a linear combination of primitive lattice vectors. The atoms in each cell are the basis of the lattice. A periodic boundary condition (PBC) is introduced to remove boundary effects between cells. We can define a reciprocal lattice, emerging from the Fourier transform of the real lattice in the physical space, in which the Fourier transform of a spatial function is represented in terms of

wavevectors of plane waves. In this lattice, the 1st Brillouin zone is defined as the most symmetric unit cell of the reciprocal lattice. Periodic systems are characterised by k-points, used to sample the Brillouin zone and, according to the Bloch theorem (see Equation (2.29)), at each k-point the electronic wavefunction can be expressed as a linear combination of plane waves:

$$\psi_{i\vec{k}}(\vec{r}) = e^{i\vec{k}\cdot\vec{r}} u_{i\vec{k}}(\vec{r}), \qquad (2.29)$$

where $\vec{r}$ is the position, u a periodic function with the same periodicity as the crystal that needs to be normilised within one unit cell, and $\vec{k}$ the crystal momentum vector.

The plane waves basis expansion includes infinite terms, but can be truncated according to a certain cutoff to include only the dominant plane waves, lower than a threshold kinetic energy. These plane waves constitute the basis set for periodic DFT. Pseudopotentials – substitutions of core electrons and strong Coulomb potentials by weaker pseudopotentials that act on a set of pseudo wavefunctions – are used to work with the lowest cutoff possible, since the full Coulomb potential of the electron-ion interaction decays too slowly to be accurately represented by a small number of components. In periodic DFT

$$\hat{H}_{\vec{k}} u_{i\vec{k}}(\vec{r}) = \epsilon_{i\vec{k}} u_{i\vec{k}}(\vec{r}), \qquad (2.30)$$

and the total DFT energy per unit cell is:

$$E_{\text{el}}[\rho] = \sum_i \int_{\text{BZ}} \frac{d\vec{k}}{\Omega_{\text{BZ}}} f_{i\vec{k}} \epsilon_{i\vec{k}} - \left[E_H + \int d\vec{r} V_{\text{xc}}(\vec{r})\rho(\vec{r}) - E_{\text{xc}} \right], \qquad (2.31)$$

where Ω_{BZ} is the volume of the Brillouin zone, and $f_{i\vec{k}}$ the occupation number of orbital i at k-point $\vec{k}$.

The $\epsilon_{i\vec{k}}$ eigenvalues are called bands. From the band structure – $\epsilon_{i\vec{k}}$ as a function of $\vec{k}$ – the allowed and forbidden levels for the electrons in the material can be identified. This information can be used to explain the physical and chemical behaviour in the solid state, such as electrical conductivity and optical absorption. Within the periodic lattice, points Γ, M, and K are the special highly symmetric points of the Brillouin zone. In this thesis, DFAs from the lower rungs of the Jacob's ladder, particularly PBE, were used for periodic computations, which tend to be considerably more demanding than modelling small finite small molecules.

2.2 Potential energy surface

Under the Born-Oppenheimer approximation, motions of nuclei and electrons can be treated separately. This enables constructing a surface where every point represents the energy at a given fixed nuclear arrangement (e.g., different conformers, reactants and products, etc.), called the potential energy surface (PES). In a non-linear molecule with N atoms, the potential energy is a function of 3N-6 internal coordinates: three for every atom minus three rotational and three translational coordinates. These 3N-6 coordinates are chosen to be linearly independent and correspond to angles, dihedrals, and bonds. PES is a hyper-surface with 3N-5 dimensions (3N-6 internal coordinates plus energy). To visualise the PES, 2- or 3-dimensional cross-sections are typically used (see Fig.2.2). In this case, the energy is expressed as a function of a single coordinate of interest, such as a dihedral angle in a conformer or a step in a reaction sequence.

Stable conformations of a molecule are critical points on the PES: at these points, first-order derivatives of potential energy are equal to zero

$$\frac{\partial E}{\partial x_i} = 0 \text{ for } i = 0, 1, .., 3N - 6, \qquad (2.32)$$

and second-order derivatives are positive for every internal coordinate x_i. The most stable conformation of a molecule is the absolute minimum on the hyper-surface. A transition state (TS) connecting the minima is a first-order saddle point: the first-order derivatives of the potential energy are still equal to zero but the second order derivatives are positive for every x_i except one, along which the TS is the maximum. The analytical expression of a PES for any meaningful chemical system is unobtainable, hence coordinates of the critical points are also not known *a priori*. To locate a critical point, its guess coordinates are changed iteratively until convergence in energy
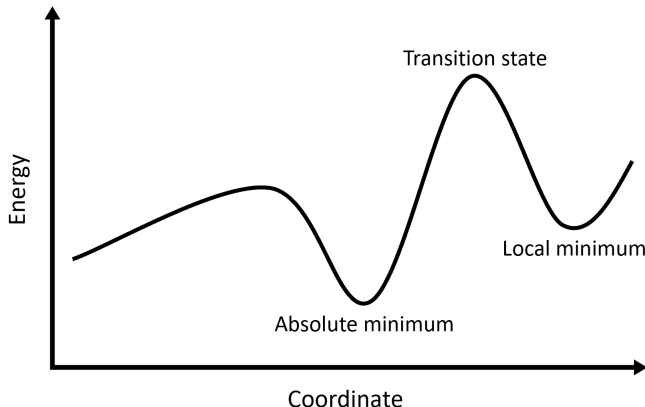
Figure 2.2: Schematic representation of a potential energy surface in two dimensions.

and derivatives is reached. For an N-atomic molecule, the procedure of geometry optimisation is difficult, because 3N-6 coordinates must be considered. Therefore, a matrix formalism is employed; the $(3N-6) \times (3N-6)$ second-order derivatives are arranged in a matrix called Hessian (H) that corresponds to the force constants matrix

$$H = \begin{pmatrix} \frac{\partial E^2}{(\partial x_1 x_1)_0} & \cdots & \frac{\partial E^2}{(\partial x_1 x_{(3N-6)})_0} \\ \vdots & \ddots & \vdots \\ \frac{\partial E^2}{(\partial x_{(3N-6)} x_1)_0} & \cdots & \frac{\partial E^2}{(\partial x_{(3N-6)} x_{(3N-6)})_0} \end{pmatrix} \qquad (2.33)$$

The nature of the stationary points found in optimisation can be verified by vibrational frequency calculations. For an N-atomic molecule, 3N-6 normal modes can be identified, each described by a vibrational frequency $\tilde{\nu}$:

$$\tilde{\nu}(cm^{-1}) = \frac{1}{2\pi c}\sqrt{\frac{k}{\mu}}. \qquad (2.34)$$

In Equation (2.34), c is the speed of light, k the force constant of the vibration, and μ the reduced mass. The 3N-6 values of k can be obtained *via* diagonalisation of the Hessian matrix. Common optimiser procedures include the steepest-descent, conjugate gradient, and Newton-Raphson methods. The most accurate algorithms perform the optimisation using both the gradient vector and the Hessian matrix, while simpler algorithms are based only on the gradient vector.

However, such optimisation procedures starting from a single guess structure explore only a fraction of the PES between the guess and the nearest (local) minima. A more thorough PES exploration, which is necessary for systems with multiple local minima that are close in energy (e.g., physisorption complexes on a GBM surface), entails sampling the PES along the coordinate of interest with a chosen step size. Each generated structure along this coordinate serves as a guess for subsequent geometry optimisation. Metadynamics (MTD) is an alternative technique for sampling the PES by adding a bias potential to the Hamiltonian of the system. This bias potential prevents the system from returning to the earlier state and allows overcoming energy barriers to reach other minima. In this thesis, metadynamics is used at the GFN2-xTB level of theory [69] and the bias potential is given by

$$E_{\text{bias}}^{\text{RMSD}} = \sum_{i=1}^{n} k_i \exp(-\alpha \Delta_i^2), \qquad (2.35)$$

where n is the number of reference structures associated with the pushing or pulling strength k, Δ the collective variable (set of variables describing the system), and the parameter α determines the width (in space and time) of the bias potential.

2.3 Non-covalent interactions

Non-covalent interactions are fundamental to many chemical phenomena, from conformational changes to catalysis and sensing. Given the comparative weakness of these interactions (usually less than 100 kJ mol^{-1} [70]), high accuracy is required in their computation and prediction. NCIs can occur both intra- and intermolecularly, and can be broadly classified depending on their physical nature: ionic, van der Waals, π-stacking, hydrophobic, *etc.* Intermolecular non-covalent interactions of various origins are central to this thesis.

The energy of the NCIs in a two-component complex AB is commonly defined as

$$\Delta E_{\text{int}} = E_{(A,B)} - (E_A + E_B), \tag{2.36}$$

where ΔE_{int} is the interaction energy, $E_{(A,B)}$ the energy of the complex AB, and E_A, E_B are the energies of A and B in isolation. This approach is an approximation, as it neglects the structural changes occurring in the fragments upon complex formation. The total interaction energy is not only insightful in its own right, but it can be further split into various components corresponding to diverse physical origins of the interaction. This can be achieved by means of various energy decomposition analysis (EDA) schemes, which can be quantitative and qualitative [41]. Quantitative EDAs can be:

- variational: associate a specific interaction with a lowering of the energy due to a specific aspect of the wavefunction relaxation. One of the most famous schemes of this type is the Kitaura-Morokuma method [71]. However, this scheme often overestimates the induction energy, because the underlying wavefunctions are not fully antisymmetric. To address this issue, exchange and electrostatic terms are not separate in other variational approaches, yet this results in a less detailed description of the interaction;

- perturbative: consider the Hamiltonian associated with the complex of interacting fragments as a perturbation to the sum of the unperturbed Hamiltonians of the fragments. SAPT is the most popular perturbative EDA, however, its limitations include high computational cost and applicability only to finite compounds (and not periodic materials).

Symmetry-adapted perturbation theory (see Section 2.1.3 for more details) [72] simultaneously offers the gold-standard quality of the NCI energy and its decomposition into physically meaningful components:

- E_{el}: electrostatic (Coulombic) interaction;

- E_{exch}: exchange-correlation (also called Pauli repulsion) contribution, which is always repulsive;

- E_{ind}: induction (polarisation), including change transfer;

- E_{el}: dispersion, which is always attractive.

In this thesis, the SAPT(DFT) version of SAPT is used, in which the Hamiltonian of the dimer is expressed as:

$$H = K_A + W_A + K_B + W_B + V, \tag{2.37}$$

where K_A and K_B are the Kohn-Sham operators for the fragments, W_A and W_B are the fluctuation potentials of the fragments, and V is the interaction potential. The SAPT(DFT) interaction energy is

$$E_{\text{SAPT(DFT)}} = E_{el}^{1,0} + E_{\text{exch}}^{1,0} + E_{\text{ind,resp}}^{2,0} + E_{\text{exch-ind,resp}}^{2,0} + E_{\text{disp,resp}}^{2,0} + E_{\text{exch-disp,resp}}^{2,0}(\text{est.}) + \delta_{\text{HF}}^{(2)} \tag{2.38}$$

where $E^{v,w}$ indicates the order in V and in $W_A + W_B$, the subscript "resp" indicates that the orbital relaxation effects are included, $\delta_{\text{HF}}^{(2)}$ takes into account higher-order induction effects, and "(est.)" means that the $E_{\text{exch-disp,resp}}^{2,0}$ term is estimated by scaling the uncoupled exchange-dispersion energy.

The Non-Covalent Interaction index (NCI index) is an example of qualitative EDA schemes [73]. The index, based on electron density and its derivatives, allows the visualisation of the position and intensity of the established non-covalent interactions. Bader's Quantum Theory of Atoms in Molecules (QTAIM) [74], another popular qualitative EDA, provides a mathematical description of

covalent and non-covalent bonds together with the visualization of the interactions. In the QTAIM framework, the molecular structure arises from the critical points in the electron density connected by the paths along the gradient of the electron density.

In this thesis, the Density Overlap Region Indicator (DORI) [75], based on the electron localisation function (ELF) and unique in its ability to describe covalent and non-covalent interactions simultaneously, is employed to analyse and visualise the NCIs. The DORI is defined as

$$\mathrm{DORI}(\mathbf{r}) = \frac{\theta(\mathbf{r})}{1 + \theta(\mathbf{r})}, \tag{2.39}$$

where

$$\theta(\mathbf{r}) = \frac{(\nabla(\frac{\nabla\rho(\mathbf{r})}{\rho(\mathbf{r})})^2)^2}{(\frac{\nabla\rho(\mathbf{r})}{\rho(\mathbf{r})})^6}. \tag{2.40}$$

DORI values can vary between 0 and 1, and can be plotted on a chosen isosurface to provide intuitive visualisation of the location and type of interaction (see Fig.2.3 for an example). Such visualisation requires four dimensions (scalar field in three-dimensional space), and therefore a specific function value has to be chosen for the isosurface. Individual closed isosurfaces are called DORI basins. Integrating electron density within a given basin provides a quantitative measure of the corresponding interaction.
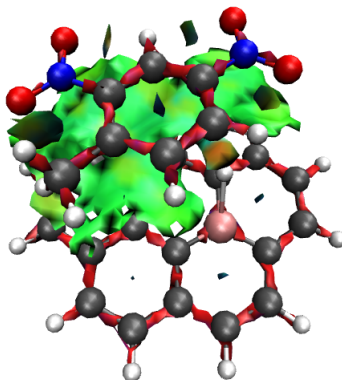
Figure 2.3: Example of a DORI = 0.98 isosurface for dinitrotoluene adsorbed on a B-doped graphene nanoflake, view from above the basal plane of the GBM model. Isosurfaces are colour-coded in the range from -0.01 au (red) to 0.01 au (blue).

2.4 Solvent effects

In a typical experimental setting of catalysis or sensing with a GBM, the latter is surrounded by a solvent. While *in vacuo* modelling is insightful (and often sufficient) when analysing the electronic structure features, inclusion of solvent effects is required for comparison with experimental observables, such as redox potentials. Models for simulating the solvent phase can be classified as:

- implicit (continuum) methods: the solvent molecules are replaced with a homogeneous polarisable medium with equivalent properties. Commonly used methods in this category are the polarisable continuum model (PCM)[76] and its variants [77], and the conductor-like screening model (COSMO) [78]. Continuum solvent models are a somewhat crude approximation to the real systems based on parametrisation, but they are the most affordable computationally. Such models are used when the solvent-solute interactions are relatively weak;

- explicit solvation: a certain number of solvent molecules is explicitly included in the system. In microsolvation, a small number of solvent molecules is placed around the solute; in macrosolvation, the full first (and sometimes even the second) solvation shell is included. These

models offer a much more realistic representation, but come at a significantly higher computational cost due to a large number of atoms treated quantum-mechanically. Consequently, *ab initio* methods become prohibitively expensive and the condensed phase is usually treated with semiempirical and/or classical mechanics approaches.

- hybrid solvation models: a combination of the previous two approaches, where a small number of solvent molecules are included explicitly and the rest of the condensed phase is represented by a polarisable continuum.

In this thesis, the SMD/IEF-PCM implicit solvent model is employed [79]. SMD (solvation model based on density) is a global method because it can be applied to any solvent provided its empirical parameters, necessary to solve the Poisson-Boltzmann equation describing the distribution of the electric potential in solution, are available. Additionally, SMD allows the decomposition of the total solvation energy into contributions from the solute-solvent dispersion, solute cavitation, and the solute-solvent repulsion. The total solvation energy from a continuum solvent model is given by

$$\Delta G_S^\circ = \Delta G_{\mathrm{ENP}} + G_{\mathrm{CDS}} + \Delta G_{\mathrm{conc}}^\circ, \tag{2.41}$$

where G_{ENP} represents the electronic, nuclear, and polarisation components of the free energy computed as the difference between the gas-phase total energies of the gas-phase and liquid-phase equilibrium structures, CDS represents the change in the free energy due to solvent cavitation, possible changes in local solvent structure and changes in dispersion energy, and $\Delta G_{\mathrm{conc}}^\circ$ is the concentration change between the gas and the liquid phase, *i.e.*, the phase change correction term.

Chapter 3

Carbon dioxide on graphene

3.1 Introduction

Carbon dioxide (CO_2) is one of the main culprits of the greenhouse effect. To remediate the associated negative environmental impacts, it is fundamental to detect, monitor, and remove CO_2 from the atmosphere. Two-dimensional materials are ideal candidates for these tasks [80, 81] because of their high surface-to-volume ratio and tunability of adsorbent and electrical/mechanical properties. GBMs in particular are well suited since their production is more sustainable compared to such alternatives as metal-organic frameworks [82], metal halide perovskite nanostructures, and quantum dots [83]. Therefore, graphene is extensively used to adsorb, detect, and transform CO_2 [84, 85, 86, 87, 88, 89, 90].

Development of efficient graphene-based adsorbents necessitates in-depth insights into the structure, strength, and nature of the associated non-covalent interactions [21]. While such insights are in principle obtainable from simulations, choosing an appropriate model of the adsorbate-GBM complex and *in silico* methodology, affording an efficient sampling of adsorption geometries, poses a major challenge. Periodic representations of the surface have the advantage of being free of defects and edge effects; yet, at the *ab initio* level it is usually feasible only at the local density or generalised gradient approximations of DFT, which cannot describe dispersion without empirical corrections or non-local functional extensions. Higher level density functionals, periodic second-order perturbation theory, random phase approximation (RPA), and the GW approach are available and able to address the previously described limitations of LDA and GGA DFT, yet they often come at a prohibitive computational cost [21]. These computations become particularly demanding when modeling adsorption in the low-coverage regime, where large surface slab models are needed, in addition to large vacuum gaps between surfaces. Finite nanoflake models, on the other hand, can be treated with a broad spectrum of wavefunction-based methods, as well as density functionals belonging to the higher rungs of the Jacob's ladder (Fig. 2.1) [61]. Unfortunately, finite models suffer from heavy size dependence of the resulting computed properties and artificial edge effects. Several studies compared finite and periodic models for studying adsorption on graphene. Specifically, Lazar *et al.* [48] computed adsorption enthalpies of small organic molecules on coronene and infinite graphene with methods ranging from empirical and density functional theory to wavefunction theory methods. For the coronene model, the best agreement with the reference CCSD(T) interaction energies was reached with a non-local optB88-vdW functional (mean error of 2.5 kJ mol^{-1}) and SCS(MI)-MP2 method (mean error of 1.7 kJ mol^{-1}). However, all tested methods were able to reproduce qualitatively the ordering of experimentally measured adsorption enthalpies. The latter were best reproduced with the *ab initio* molecular dynamics at the optB88-vdW level in conjunction with a periodic model. Haldar *et al.* [91] demonstrated the convergence of interaction energies for two organic electron acceptor molecules adsorbed on graphene with the size of coronene-based models, justifying the use of finite models. Considering the levels of theory, the SCS-MP2/CBS, BLYP-D3, and AMBER force field showed modest accuracy (within *ca.* 10 kJ mol^{-1}) compared to the reference MP2.5/CBS/6-31G*(0.25) values. Recently, Stachová *et al.* [92] compared the performance of several DFT methods for predicting adsorption energies of monolayers of noble gases (Ar, Kr, and Xe) and small molecules (N_2, O_2, CO, CH_4, C_2H_6, and C_3H_8) on both free-standing and Pt(111)-supported graphene. Both high-level RPA and fixed-node diffusion Monte Carlo computations, as well as previously published experimental results, were used for

method benchmarking. For unsupported graphene, the authors recommended optB86b for geometries and PBE-D3 for adsorption energies. In the case of graphene on Pt(111), the best approach was found to depend on the magnitude of the interactions: PBE-D3 for weakly interacting systems (<20 kJ mol^{-1}), and optB86b-vdW for stronger physisorptions (>20 kJ mol^{-1}).

To establish reliable approaches for simulating adsorbate-GBM complexes, we focus on the CO_2 adsorption on pristine graphene. This system provides a rare opportunity to benchmark the theoretical methodology for computing interaction energies, as it is the only system for which adsorption enthalpies have been measured experimentally. In a combined temperature programmed desorption and X-ray photoelectron spectroscopy study of CO_2 adsorbed on a monolayer graphene deposited on a SiC(0001) surface [93], the adsorption energy was estimated at 30.1 ± 1.5 kJ mol^{-1} at low coverage and at 25.4 ± 1.5 kJ mol^{-1} at high coverage. Using van der Waals density functional (vdW-DF) theory, parallel orientation of the carbon dioxide molecule on graphene surface was proposed. In another recent study [94], temperature programmed desorption and reflection absorption infrared spectroscopy were used to measure the adsorption enthalpy for CO_2 on a graphene-covered Pt(111) surface, resulting in an adsorption enthalpy of 26.1 ± 2 kJ mol^{-1} at low coverage. Moreover, analyses of the obtained reflection adsorption infrared spectra suggested tilted geometry for the adsorbate on the surface.

In this Chapter, we assessed for carbon dioxide adsorbed on graphene in a low-coverage regime how various simulation approaches for predicting adsorption energies and geometries fared, and compared our findings to reported experimentally measured results. The methodological approaches explored ranged from the smallest possible graphene model, benzene, treated at various levels of DFT and with highly accurate wavefunction theory-based methods, to a realistic periodic representation of an unsupported graphene monolayer.

3.2 Computational methods and models

3.2.1 Finite models

The structures for finite models of graphene investigated here were classified based on their shapes: circular (benzene, coronene, and circumcoronene), zigzag (rhomboid), and armchair (rectangular, see Fig.3.1a). For each shape, three nanoflake sizes were considered. For each model, three principal adsorption sites - top, hollow, and bridge (shown in Fig.3.1b) – were each considered in conjunction with the parallel or orthogonal orientations of the CO_2 molecule (shown in Fig.3.1c). In the larger systems, CO_2 was positioned either above the central C–C bond (for 2×2-zigzag, 4×4-zigzag, 3×2-armchair), or above the ring center. Constrained optimisations were performed to preserve the initial adsorption geometries, since they do not necessarily correspond to local minima on the potential energy surface. The resulting structures were then compared to the fully relaxed ones, obtained by unconstrained optimisations, and confirmed by normal mode analysis. Interaction energies were computed as the difference between the energies of the optimised complex and the CO_2 and GBM model separately and in their complex geometries. Computations for CO_2 and GBM models were performed in the basis set of their complex to correct for the basis set superposition error. We note that interaction energies evaluated in this manner neglect structural relaxation upon complex formation, although this is relatively small in non-covalently bound complexes of small and/or rigid molecules.

In the case of finite systems, the following DFT methods including appropriate dispersion corrections were used:

- GGA functional PBE-D3 [95, 96, 63];

- hybrid-GGA functional B3LYP-D3 [97, 98, 63];

- long-range separated functional ωB97X-D [99] and its non-local version ωB97X-V [100] for single-point energies;

- double-hybrid functional DSD-BLYP-D3 [101].

All DFT computations were performed with the Orca software, version 4.0 [102]. Convergence thresholds were set as very tight and the largest DFT grid was employed. Two basis sets belonging to the Karlsruhe family were used (see Section 2.2.1.4).
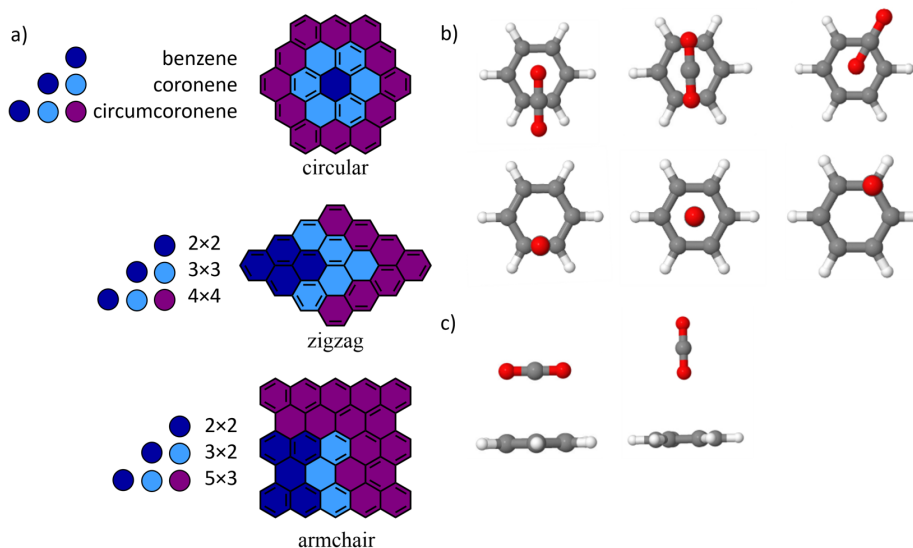
Figure 3.1: a) Models and notations of pristine graphene nanoflakes with various shapes and sizes. b) From left to right: bridge, hollow, and top adsorption sites, shown for parallel (top row) and orthogonal (bottom row) orientations. c) Lateral view of parallel (left) and orthogonal (right) orientation, shown for the hollow site.

For the smallest model system of a GBM – benzene – coupled-cluster with singles, doubles, and perturbative triples (CCSD(T)) computations were performed using the CFOUR software [103]. A variation of the coupled-cluster theory, the domain local-pair natural orbital coupled-cluster method (DLPNO-CCSD(T)) [104, 105], was also used as implemented in the Orca program. SAPT computations at SAPT0/jun-cc-pVDZ level (see Section 2.2.1.4) in conjunction with DFT (PBE-D3) geometries were performed with the resolution-of-the-identity (RI) approximation using the Psi4 program [106]. DLPNO-CCSD(T) results extrapolated to complete basis set (CBS) limit were taken as a reference.

3.2.2 Periodic models

To model a single layer of pristine graphene, a 7×7 supercell (see Fig.3.2) containing 98 carbon atoms was chosen. Periodic simulations were performed using Quantum Espresso [107] with PBE-
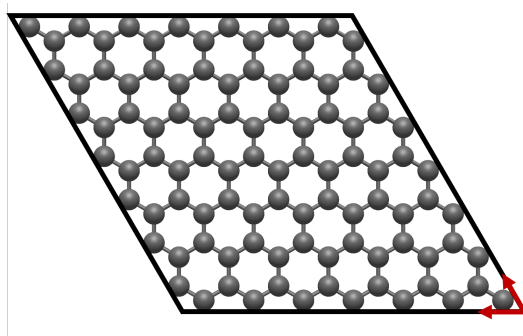
Figure 3.2: Top view of a 7×7 graphene periodic model.

derived pseudopotentials from the PSLibrary [108]. An energy cutoff of 90 Ry was selected after evaluating the dependence of the interaction energy on the cutoff. In all systems, a $3\times3\times1$ k-point grid was used. The adsorption geometry was preserved throughout optimisations and therefore no constraints was needed. Computations were performed with PBE-D3 [95, 96, 63] and B86BPBE-XDM [109] GGA functionals, vdW-DF1 [110], vdW-DF2 [111], optB88-vdW [112], and optB86b-vdW [113] functionals. Nudged elastic band (NEB) [114, 115] simulations were performed to find minimum energy paths between adsorption sites, as implemented in the Atomic Simulation

Environment (ASE) package [116].

3.3 Results and discussion

3.3.1 Method benchmark on CO_2-benzene

Initial assessment of electronic structure theory methods was performed for the smallest model, a CO_2-benzene complex, using the DLPNO-CCSD(T)(TightPNO)/CBS as a reference (Table 3.1). In DFT computations, the same level of theory was used for geometry optimisations and single-point energy computations; interaction energies with post-HF methods were obtained in conjunction with CCSD(T)/def2-TZVP geometries.

Table 3.1: Computed interaction energies (in kJ mol^{-1}) for CO_2 on benzene at various adsorption sites and orientations. The mean absolute deviation (MAD) is calculated with respect to the DLPNO-CCSD(T)(TightPNO)/CBS results and averaged across all orientations.

| Method | Global minima | Constrained optimization | | | | | | MAD |
| | | Parallel | | | Orthogonal | | | |
		Bridge	Top	Hollow	Bridge	Top	Hollow	
Method // CCSD(T)/def2-TZVP								
DLPNO-CCSD(T)(TightPNO)/CBS	-10.0	-9.7	-9.3	-9.1	-1.6	-1.7	-2.2	0.0
CCSD(T)/def2-TZVP	-7.6	-7.2	-6.9	-7.1	-0.4	-0.4	-0.5	1.9
SAPT0/jun-cc-pVDZ	-9.0	-8.4	-8.0	-8.2	0.1	0.0	0.2	1.5
Method/def2-TZVP // Method/def2-TZVP								
PBE-D3	-10.2	-9.9	-9.6	-9.5	-1.7	-1.7	-2.1	0.2
B3LYP-D3	-10.9	-10.5	-10.2	-10.0	-0.9	-0.9	-1.3	0.8
ωB97X-D	-11.3	-10.9	-10.5	-10.3	-1.0	-1.0	-1.5	1.0
ω B97X-V	-10.6	-10.2	-9.8	-9.8	-1.2	-1.2	-1.8	0.5
DSD-BLYP-D3	-9.2	-8.8	-8.4	-8.4	-0.8	-0.8	-1.1	0.9
Method/def2-QZVPPD // Method/def2-TZVP								
PBE-D3	-10.2	-9.9	-9.7	-9.4	-2.0	-2.0	-2.4	0.3
DSD-BLYP-D3	-10.1	-9.8	-9.5	-9.2	-1.4	-1.3	-1.9	0.2

Our results in Table 3.1 indicate the following:

- at all tested levels of theory, parallel orientations are significantly more stable than the orthogonal ones;

- computed interaction energies are notably higher (weaker) compared to experiments. This suggests, unsurprisingly, that benzene might not be a good model for extended graphene;

- very similar interaction energies correspond to different adsorption sites (top, bridge, hollow), especially in the orthogonal orientation;

- all DFT methods and SAPT0 predict the same relative order of interaction strengths across considered adsorption sites. CCSD(T) results for the parallel orientation slightly deviate from this trend;

- CCSD(T) predicts the weakest interaction, and SAPT0 the strongest. We attribute this to basis set effects in the coupled cluster computations, since SAPT0 results are in good agreement with the DLPNO-CCSD(T) results in complete basis set limit;

- trends in DFT results are in line with those obtained in a previously reported benchmarking [117], with better performance being achieved with double hybrid and non-local functionals. Interestingly, PBE-D3 - a GGA functional from the lower rungs of the Jacob's ladder – seems to outperform other, more sophisticated DFT methods in terms of matching reference results.

To further rationalise these results, we compared the geometries obtained with different methods (Table 3.2). In the structures obtained from unconstrained optimisations, *i.e.*, the global minima, we considered several geometrical parameters: (1) the distance between the benzene plane and either the carbon (for parallel orientations) or the closest oxygen atom (for orthogonal orientations) of the CO_2 molecule, (2) the tilt angle between the axis of CO_2 and the benzene plane, and (3) an angle between the carbon atom of CO_2 and its projection onto the benzene plane (see Fig.3.3). Since relative orientations were kept frozen in constrained optimisations, only the distance between carbon dioxide and benzene was considered here. CCSD(T) geometry was used as a reference. We found that all methods yield the same qualitative trends. However, PBE-D3 overestimates the adsorption distance, which can be explained by its neglect of HF-like exchange [118] or by many-body effects. The shortest distances were obtained with ωB97X-D for parallel orientations and with DSD-BLYP-D3 for orthogonal orientations. The latter method most closely reproduces the reference geometries.
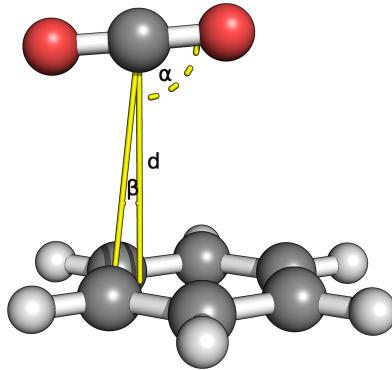
Figure 3.3: Geometrical parameters of the CO_2-benzene complex: tilt angle (α), distance between the benzene plane and the center of mass of carbon dioxide (d), and the angle between the adsorption site, center of mass of CO_2, and its projection onto benzene plane (β).

Table 3.2: Geometrical parameters (see Fig.3.3) for adsorption sites of CO_2 on benzene, computed with different methods.

| Method/def2-TZVP | Global minima | | | Constrained optimisation | | | | | |
| | | | | Parallel | | | Orthogonal | | |
	α^a	β^b	d [Å]^c	Bridge^d	Top^d	Hollow^d	Bridge^d	Top^d	Hollow^d
CCSD(T)	92.5	3.8	3.25	3.24	3.24	3.40	3.41	3.42	3.27
PBE-D3	93.8	1.6	3.30	3.30	3.29	3.47	3.46	3.46	3.36
B3LYP-D3	93.3	2.1	3.25	3.25	3.24	3.40	3.44	3.43	3.29
ωB97X-D	93.2	2.2	3.21	3.22	3.21	3.38	3.45	3.46	3.33
DSD-BLYP-D3	92.5	3.2	3.24	3.23	3.23	3.39	3.40	3.40	3.26

^{a} tilt angle α.
^{b} angle between the adsorption site, center of mass of CO_2, and its projection onto benzene plane β.
^{c} distance between the benzene plane and the center of mass of carbon dioxide of global minimum.
^{d} distance between the benzene plane and the center of mass of carbon dioxide d [Å] of constrained optimisations of each interaction type.

Considering the accuracy in both the interactions energies and adsorption geometries, the best performance amongst the DFT methods is achieved with the double-hybrid DSD-BLYP-D3, in agreement with previous benchmarks [117]. However, high computational cost precludes its application to more realistic (larger) models of pristine graphene. At the same time, the humble PBE-D3 method yields excellent results for energies and good quality of predictions for geometries.

3.3.2 Size dependence of the interaction energies

To probe the transferability of the CO_2-benzene results to larger models of graphene, we computed E_{int} for a range of model sizes and shapes (see Fig.3.1) up to periodic models using various DFAs

(see **Appendix** for details). For simplicity, only the PBE-D3/def2-TZVP results are discussed further (Table 3.3).

Table 3.3: Size dependency of the PBE-D3/def2-TZVP interaction energies (in kJ mol^{-1}) of CO_2 on various graphene nanoflakes models. Size is expressed as the number of carbon atoms in the model.

Model	Size	Global minima	Parallel			Orthogonal		
			Bridge	Top	Hollow	Bridge	Top	Hollow
Benzene	6	-10.2	-9.9	-9.6	-9.5	-1.7	-1.7	-2.1
Coronene	24	-13.9	-13.9	-13.2	-12.8	-6.0	-5.8	-6.9
Circumcoronene	54	-15.4	-15.4	-14.6	-14.0	-7.6	-7.5	-8.2
2×2-zigzag	16	-13.1	-13.1	-12.3	-11.4	-5.1	-4.9	-4.9
3×3-zigzag	30	-14.3	-14.2	-13.6	-13.1	-6.3	-6.4	/[a]
4×4-zigzag	48	-15.2	-15.2	-14.5	-13.8	-7.4	-7.4	-7.8
2×2-armchair	20	-13.3	-13.3	-13.0	-12.2	-5.2	-5.2	-6.2
3×2-armchair	28	-14.4	-14.4	-13.7	-12.8	-6.6	-6.4	-6.9
5x3-armchair	66	-15.5	-15.5	-14.8	-14.0	-7.7	-7.6	-8.3

[a] no minima

These results (Table 3.3) show that carbon dioxide is adsorbed more strongly on larger nanoflakes, for all orientations and adsorption sites. Furthermore, for all model sizes the interaction energies follow the same relative order of adsorption sites; the bridge parallel adsorption is always the most stable one.

With respect to the dependence of the geometry of the CO_2 adsorption on benzene on the model size (Table 3.4), we can infer that:

- the increase in the stability of CO_2-graphene complexes with the increase of the model size is accompanied by shorter interaction distances. Extent of this decrease in distance depends on the adsorption site. The decrease is relatively small for the bridge parallel adsorption (from 3.30 Å for benzene to 3.24 Å for the 5×3-armchair model), but larger for the hollow orthogonal (from 3.36 Å for benzene to 3.10 Å for the 5×3-armchair model);

- larger models (circumcoronene, 4×4 zigzag, and 5x3 armchair) converge to similar geometries;

- all global minima have similar geometry independent on the model, and this geometry is in turn very close to that of the bridge parallel adsorption site.

Furthermore, we find that that the interaction energy is approximately linearly dependent on the inverse of the size of the graphene nanoflake, expressed as the reciprocal of the number of carbon atoms in the model (see Fig.3.4). The linear fit intercepts the vertical axis for $x=0$, which corresponds to the infinite number of carbons in the model, $i.e.$, an infinite graphene sheet. Such extrapolation schemes have been reported in literature for several other adsorbates and GBMs [119, 120, 121, 122]. An extensive benchmark, including such high-level methods as coupled-cluster, diffusion Monte Carlo, and random phase approximation by Brandendurg et $al.$ [123] on the physisorption of water on graphene questioned the reliability of these schemes. However, a good agreement between highly accurate methods and extrapolated results has been achieved once the latter included long-range effects [124]. Crucially, the key advantage of these extrapolation schemes is that a given property, e.g., the interaction energy, can be predicted for an arbitrarily large (even infinite) graphene model from values obtained for much smaller systems. This allows accurately estimating E_{int} without the limitations of the computational cost given by the scaling of the method with the size. The extrapolated interaction energies obtained here with different methods are reported in Table 3.5.

Previously established trends in the relative stability of adsorption sites are retained in extrapolated E_{int}, with the bridge parallel being the most stable geometry, very close to the global minima. Among the DFT methods, PBE-D3 yields the highest (weakest) interaction energy and B3LYP-D3 – the lowest (strongest). Interaction energies obrained with SAPT0 are even lower and are relatively insensitive to the underlying geometries. We also assessed several DFT methods on

Table 3.4: Geometrical parameters (see Fig.3.3) for adsorption sites of CO_2 on benzene, computed for different sizes and shapes of models at the PBE-D3/def2-TZVP level of theory.

| Model | Global minima | | | | Constrained optimisation | | | | |
| | | | | | Parallel | | | Orthogonal | |
	α[a]	β[b]	d [A][c]	Bridge[d]	Top[d]	Hollow[d]	Bridge[d]	Top[d]	Hollow[d]
Benzene	93.8	1.6	3.30	3.30	3.29	3.47	3.46	3.46	3.36
Coronene	87.8	2.2	3.28	3.27	3.32	3.37	3.20	3.21	3.12
Circumcoronene	89.4	1.1	3.25	3.25	3.29	3.35	3.18	3.19	3.11
2×2-zigzag	90.0	0.1	3.29	3.29	3.34	3.39	3.21	3.23	3.19
3×3-zigzag	87.9	2.8	3.27	3.27	3.31	3.36	3.20	3.20	/[e]
4×4-zigzag	90.0	0.1	3.25	3.25	3.30	3.35	3.18	3.18	3.11
2×2-armchair	87.2	4.3	3.28	3.28	3.32	3.39	3.22	3.23	3.13
3×2-armchair	89.5	0.1	3.26	3.26	3.31	3.37	3.18	3.20	3.12
5×3-armchair	89.6	0.1	3.24	3.24	3.29	3.35	3.18	3.20	3.10

[a] tilt angle α.
[b] angle between the adsorption site, center of mass of CO_2, and its projection onto benzene plane β.
[c] distance between the benzene plane and the center of mass of carbon dioxide of global minimum.
[d] distance between the benzene plane and the center of mass of carbon dioxide d [Å] of constrained optimisations of each interaction type.
[e] no minima found for this model and constrained optimisation
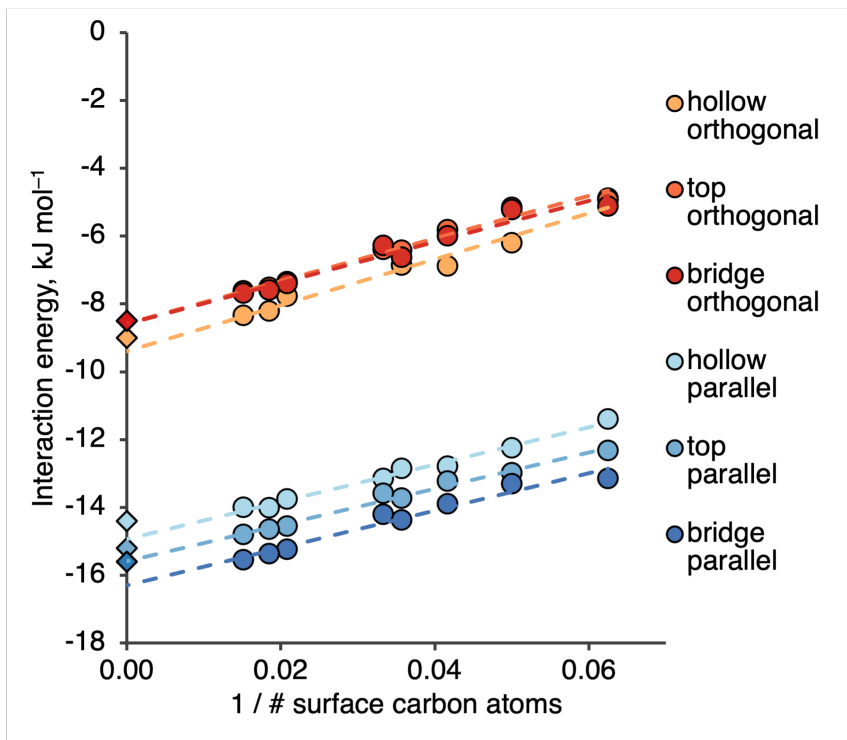
Figure 3.4: PBE-D3/def2-TZVP interaction energies of CO_2 as a function of the inverse of the number of carbon atoms in the finite surface model (circles), as well as linear regression fits of the finite model data points (dashed lines), and corresponding PBE-D3 E_{int} for the periodic model (diamonds).

the periodic model of pristine graphene (Table 3.6), establishing that dispersion-corrected GGA functionals, PBE-D3 and B86BPBE-XDM, predict E_{int} 4 to 9 kJ mol^{-1} weaker than the vdW functionals. At the PBE-D3 level, the periodic results are only 0.8 and 1.8 kJ mol^{-1} higher for parallel and orthogonal orientations, respectively, than the extrapolated values (Table 3.5), further validating the reliability of the extrapolation scheme. Considering experimentally measured adsorption enthalpies [93, 94], our predicted energies are still higher (weaker interactions), suggesting

Table 3.5: Extrapolated E_{int} (kJ mol^{-1}) of carbon dioxide adsorbed on an artificial infinite graphene model computed with different DFAs and SAPT0.

| Method | Global minima | Constrained optimisation | | | | | |
| | | Parallel | | | Orthogonal | | |
		Bridge	Top	Hollow	Bridge	Top	Hollow
Method/def2-TZVP // Method/def2-TZVP							
PBE-D3	−16.3	−16.3	−15.6	−14.9	−8.6	−8.6	−9.4
B3LYP-D3	−19.8	−19.8	−18.8	−18.0	−9.5	−9.5	−10.6
ωB97X-D	−17.9	−17.8	−16.6	−15.8	−8.4	−8.4	−9.5
ω B97X-V	−18.6	−18.6	−17.4	−16.7	−9.7	−9.7	−10.4
DSD-BLYP-D3	−18.9	−18.9	−18.0	−17.3	−10.3	−10.3	−11.6
SAPT0/jun-cc-pVDZ // Method/def2-TZVP							
PBE-D3	−20.7	−20.6	−19.3	−18.4	−12.7	−12.7	−14.0
B3LYP-D3	−20.9	−20.9	−19.5	−18.5	−12.9	−12.9	−14.4
ωB97X-D	−20.8	−20.7	−19.3	−18.5	−12.7	−12.7	−14.1
DSD-BLYP-D3	−21.4	−21.2	−20.0	−18.9	−13.2	−13.2	−14.9

that vibrational effects and support materials might be providing additional stabilisation.

Table 3.6: Interaction energies (in kJ mol^{-1}) of CO_2 adsorbed on periodic graphene.

| Method | Constrained optimisation | | | | | |
| | Parallel | | | Orthogonal | | |
	Bridge	Top	Hollow	Bridge	Top	Hollow
PBE-D3	−15.2	−13.8	−13.2	−7.8	−7.8	−8.3
B86BPBE-XDM	−13.0	−12.3	−11.1	−6.0	−6.0	−6.6
vdW-DF-1	−21.0	−20.6	−20.0	−12.9	−12.9	−13.4
vdW-DF-2	−17.7	−17.2	−16.3	−10.1	−10.0	−10.5
optB88-vdW	−21.5	−20.9	−19.4	−12.5	−12.4	−13.2
optB86b-vdW	−22.5	−21.7	−20.4	−12.7	−12.6	−13.3

3.3.3   Orientation of CO_2 and nature of the interactions

Parallel or tilted?

The orientation of the carbon dioxide molecule, different between the two supports, is another important experimental observation. All of our results suggest that bridge parallel orientation is always preferred over tilted geometries. To further explore the two orientations, we performed a potential energy scan from the parallel orientation to orthogonal using the nudged elastic band approach, with three intermediate adsorption geometries. SAPT energy decomposition analysis (see Fig.3.5a) of interaction energies along this path shows that all four energy contributions – dispersion, electrostatics, exchange, and induction – undergo significant changes along this transition. More precisely, all energy contributions become smaller in absolute terms. The most drastic reductions are found for the attractive contributions, leading to a weaker interaction for the orthogonally oriented CO_2. All three adsorption sites – bridge, hollow and top – show the same trend when transitioning from parallel to orthogonal orientation (see Fig.3.5b), although the intermediate geometries are less stable (and even repulsive) than in the other two sites.

That none of the models and methods employed here reproduce the tilted CO_2 geometry, experimentally observed for graphene deposited on a Pt(111) support, is open to interpretation. Support material likely modulates the electronic structure of graphene and can potentially prompt a reorientation of the CO_2 molecule. Inclusion of structural defects, dynamic, concentration, and pressure effects in the simulations can further change the trends in computed energetics. On the other hand, experimental data for this system is limited to only two studies, and would benefit from careful reexamination.
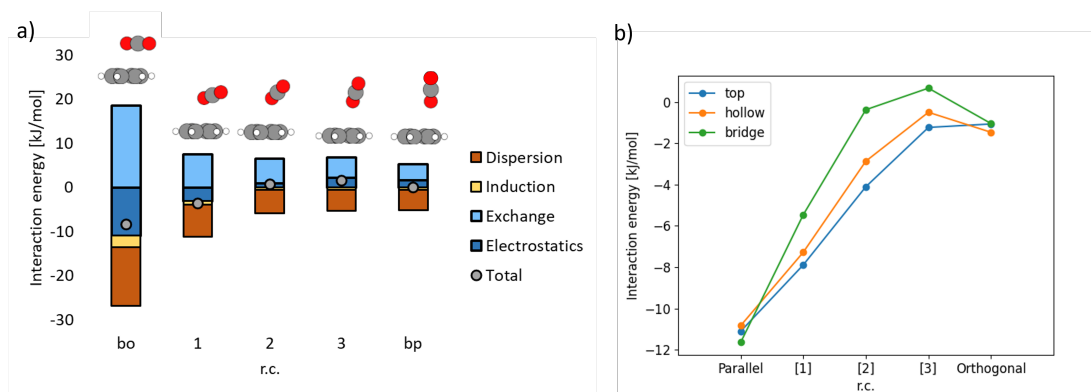
Figure 3.5: SAPT0/jun-cc-pVDZ results for the minimum energy path between parallel and orthogonal orientation. a) Energy decomposition analysis along the rotation coordinate for the bridge adsorption site; b) Total interaction energy along the rotation coordinate for all adsorption sites.

Nature of the interactions

Symmetry adapted perturbation theory was employed to elucidate the driving physical forces behind CO_2 adsorption on graphene. We decomposed SAPT0 interaction energies at the most stable adsorption geometry (Fig.3.6a) for all investigated graphene nanoflakes, establishing that, with the exception of benzene, the induction and electrostatic components are practically constant and independent on the system size and shape. Benzene shows a different behaviour because of the hydrogen bond, with a strong electrostatic component, established between carbon dioxide and the edge hydrogens (see Fig.3.6b).
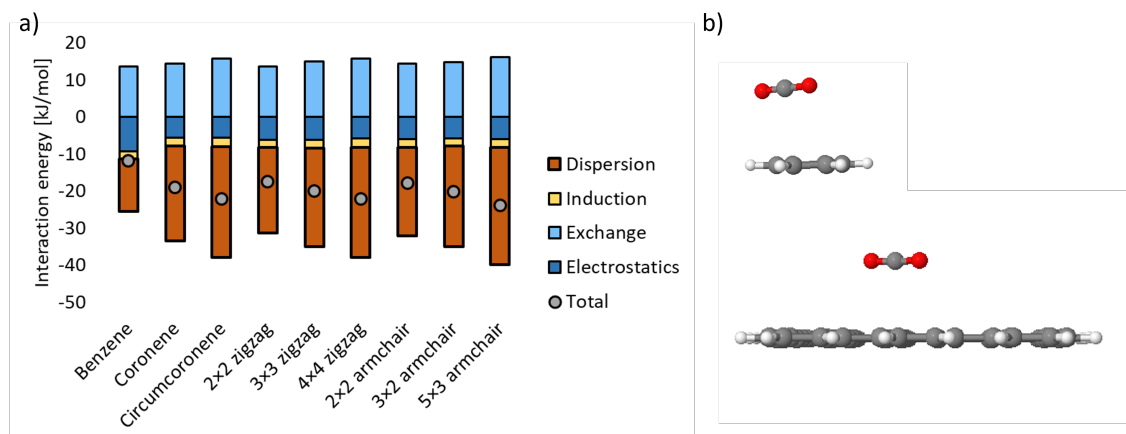
Figure 3.6: a) SAPT0/jun-cc-pVDZ interaction energy decomposition for CO_2 adsorption on graphene nanoflakes at the global minimum adsorption geometry. b) Side view of the PBE-D3/def2-TZVP global minima adsorption geometry for CO_2 on benzene (top) and on a 5×3 model (bottom).

On the other hand, exchange and dispersion interactions show significant size dependence, both becoming more important in larger nanoflakes. Between these two components of the total interaction energy, the effect of the nanoflake size on dispersion is stronger and is thus the main reason behind the increasing stability of larger systems.

3.4 Conclusions

We have modelled the adsorption of carbon dioxide on graphene, aiming to assess the impact the chemical model and the level of theory have on the computed interaction energies, and to establish a simulation approach most accurately reproducing the experimental adsorption energies in the low-coverage regime. For benzene, the smallest molecular approximation to pristine

graphene considered, comparison with the gold standard of quantum chemistry, CCSD(T), identified double-hybrid DSD-BLYP-D3 as the best performing density functional, in accordance with previous benchmarking studies. However, all computed interaction energies for CO_2 on benzene were notably higher (weaker) compared to experiment, indicating the need for larger, more realistic models. We also found that the relative order of different adsorption sites is generally independent on the method and model size. However, good agreement with experimental adsorption energies could not be achieved even with large models, suggesting that other factors (support material, vibrational effects, etc.) play additional stabilising roles. Considering adsorption geometries, the longest intermolecular distances were predicted by PBE-D3, followed by B3LYP-D3 and ωB97X-D3. The double hybrid DSD-BLYP-D3 predicted the shortest interaction distances, and, combined with SAPT0, lead to the most stable clusters. For a series of increasingly larger graphene models, a linear fit extrapolating computed interaction energies of CO_2 from nanoflakes to infinity accurately reproduced the results of periodic computations. This scheme represents a simple yet powerful tool for predicting high-quality interaction energies of periodic materials from computations on several finite models, which can be performed with more sophisticated electronic structure theory methods and analysed using diverse energy and density decomposition analyses. Overall, qualitatively reliable adsorption energies can be obtained with medium-sized graphene models using the computationally inexpensive PBE-D3 method. For accurate absolute energetics, geometries should be obtained with higher-level functionals, such as DSD-BLYP-D3, and SAPT0 energies should be extrapolated to the infinite size limit. Furthermore, we found that all parallel adsorption geometries were more stable than the orthogonal ones, in contrast to the experimental observations for CO_2 on a platinum-supported graphene. Energy decomposition analysis revealed dispersion to be the driving force behind the increasing stabilisation in larger systems. Dispersion is also the reason for the destabilisation of the orthogonal adsorption compared to parallel orientation. In periodic computations, vdW functionals predicted interaction energies *ca.* 10 kJ mol^{-1} lower than dispersion-corrected GGA functionals.

In this Chapter, we have demonstrated that even for simple systems, such as carbon dioxide adsorbed on graphene, computed interaction energies significantly depend on the chosen level of theory and computational model of graphene. While highly accurate methods can be used as benchmarks for small, molecular systems, choosing reliable approaches for periodic systems ultimately calls for more experimental data.

The results reported herein were obtained in collaboration with Dr. Christopher Ehlert, who further expanded the project by testing additional post-HF methods and including the effects of temperature and supports. Nonetheless, inclusion of these factors was found to introduce only small changes to the computed interaction energies, in the order of a few kJ mol^{-1}. Even in the presence of the Pt(111) support, parallel orientation of carbon dioxide remained energetically preferred at all tested levels of theory and graphene models, thus we were still unable to reproduce *in silico* the experimentally detected tilted geometry. The results of this work were published as Ref. [125].

Chapter 4

Adsorption of nitroaromatic compounds on graphene-based materials

4.1 Introduction

Nitroaromatic compounds (NACs) (Fig.4.1) are common contaminants found in soil and water because of their large-scale use as explosives in mining and military applications, and as building blocks in industrial production of many systems, from dyes to polymers. NACs are extremely hazardous since they persist in the environment for decades, are not biodegradable [126], and pose serious risk to human health due to their facile absorption through skin and high bioaccumulation rates [127]. In this thesis, we focus on 2,4-dinitrotoluene (DNT) and 2,4,6-trinitrotoluene (TNT) (Fig.4.1), which are among the most commonly used and extensively studied representatives of the NAC family.
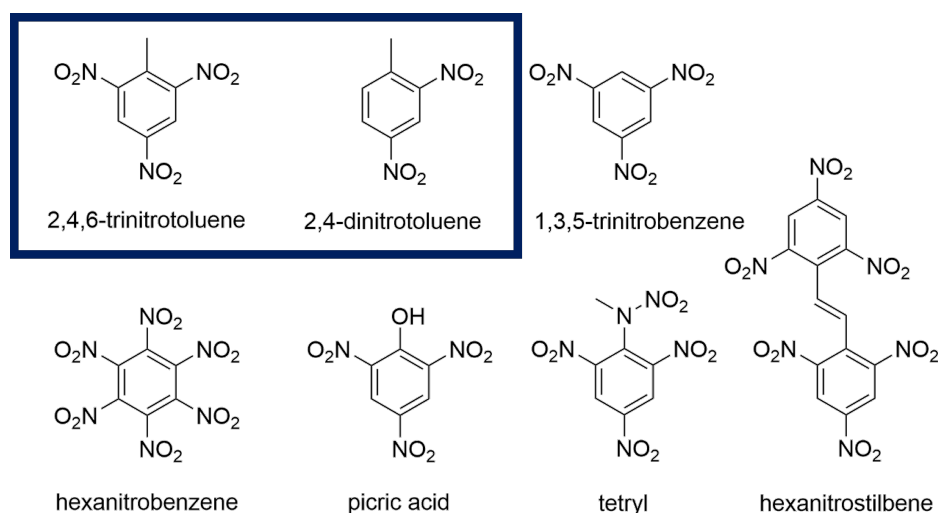
Figure 4.1: Structures of common NACs.

Detecting minute amounts of NACs in soil and water is of great importance to public health and safety, forensics, and anti-terrorism operations [128]. Common detection methods include surface-enhanced Ramanspectroscopy [129], high-performance liquid chromatography (HPLC) [130], and numerous others [131, 132]. Among them, electrochemical detection based on the reduction of nitro-groups to amino-groups [133] enables real-time on-site analysis [134] with low limits of detection (LOD) and large linear range, using a relatively low cost and compact sensor [135].[1] For

---

[1] The (LOD) of a sensor is the minimal concentration of the analyte that generates a signal significantly different from the blank [40].

these reasons, electrochemical sensors are among the state-of-the-art methods for detecting NACs. GBMs in particular, given their excellent mechanical [136] and electrochemical properties [137], high surface-to-volume ratio, and biocompatibility, are attractive candidates for these efficient and sustainable sensors.

In 2014, the first GBM-based sensor for NACs, in which graphene was decorated with palladium nanoparticles and 1,3,6,8-pyrenetetrasulfonic acid sodium salt, was developed [138]. However, the reliance on the precious metal hinders economically viable large-scale production. Subsequently, cheaper and more sustainable graphene-based alternatives were developed since to detect nitroaromatics, including electrochemically exfoliated graphene [134], hydrogenated graphene [139], reduced graphene oxide [140], N,S-codoped graphene nanoribbons [141], N-doped graphene[142], and others [143, 144, 145]. We have assembled an extensive overview of the published experimental literature (Table 4.1) to analyse potential structure-sensitivity relationships, pertinent to GBM-based electrochemical sensors. The information collected refers not only to the limits of detection of DNT and TNT in various saline aqueous environments, but also, where available, to the analytical characterisation of the GBM structure and composition, used in this work to construct the model systems. Analysis of this literature data suggests the following:

- Graphene obtained by electrochemical exfoliation [134]:the limit of detection is generally lower for the GBMs obtained with the lithium perchlorate compared to sodium sulphate. This trend is attributed to the higher content of oxygen-containing functional groups in GO-LiClO$_4$ (C/O ratio = 4) than in GO-Na$_2$SO$_4$ (C/O ratio = 8.8), which gives rise to stronger interactions between the sensor and the NAC and, ultimately, a lower LOD;

- Graphene nanosheets and nanoribbons [139]: detectors utilising nanoribbons, rich in sp^2-hybridised carbon, are more sensitive than those based on nanosheets;

- Reduced graphene oxide (rGO) and hydrogenated rGO [139]: sensors employing non-hydrogenated rGO enable improved detection relative to their hydrogenated analogues, highlighting the importance of sensor's planarity and π-conjugation, leading to stronger π-π stacking with the nitroaromatic analytes;

- rGO obtained through different experimental procedures [140]: the sensitivity of the sensor appears to depend on the oxygen content in the GBM. Specifically, for rGO-HO, rGO-HU, and rGO-ST (where HO, HU, and ST stand, respectively, for Hofmann, Hummers, and Staudenmaier synthetic procedures, see **Chapter 1**), the sensitivity of the detector is higher in less oxygenated GBMs;

- Single-, few-, and multi-layered nanoribbons and graphite nanoparticles [144]: the sensitivity of these materials weakly depends on the number of graphene layers, and the linear range of response is larger for graphite nanoparticles;

- N-doped graphene [142]: these sensors show low limits of detection, possibly due to additional non-covalent interactions between the electrophilic nitroaromatic analyte and the electron-rich GBM containing pyridinic nitrogen atoms;

- N,S-codoped-nanoribbons [141]: demonstrate the best performance, potentially due to such additional interactions as hydrogen bonding between sensor and analyte. However, synthesis of these materials can be challenging and not sustainable on a large scale.

Table 4.1: Reported performance and experimental conditions for GBMs-based sensors for DNT and TNT.

Ref.	NAC	Electrode [a]	Experimental conditions [b]	LOD (ppm)	Features
[134]	DNT	GC	BBS	11.26	/
[134]	DNT	GC	9:1 sea water and BBS	3.17	/
[139]	DNT	rGO	9:1 sea water and BBS	/	/

... CONTINUED

Ref.	NAC	Electrode [a]	Experimental conditions [b]	LOD (ppm)	Features
[139]	DNT	rGO-Hydr.	9:1 sea water and BBS	/	Loss of aromaticity
[140, 145]	DNT	rGO-ST	BBS	/	C/O =24.1
[140, 145]	DNT	rGO-HU	BBS	/	C/O =19.27
[140, 145]	DNT	rGO-HO	BBS	/	C/O =18.22
[134]	DNT	GO-LiClO$_4$	9:1 sea water and BBS	4.35	high in hydroxyls and carbonyls
[134]	DNT	GO-LiClO$_4$	BBS	2.73	high in hydroxyls and carbonyls
[134]	DNT	GO-Na$_2$SO$_4$	9:1 sea water and BBS	5.97	epoxies, hydroxyls, carboxyls and carbonyls
[134]	DNT	GO-Na$_2$SO$_4$	BBS	5.43	epoxies, hydroxyls, carboxyls and carbonyls
[143]	TNT	G-sheet	9:1 sea water and BBS	0.52	50×50 nm
[143]	TNT	G-sheet	BBS	/	50×50 nm
[143]	TNT	G-ribbon	9:1 sea water and BBS	0.14	5000×300nm
[143]	TNT	G-ribbon	BBS	/	5000×300nm
[144]	TNT	G-SL	Artificial sea water	∼1	100×100nm
[144]	TNT	G-FL	Artificial sea water	∼1	100×100nm
[144]	TNT	G-ML	Artificial sea water	∼1	100×100nm
[144]	TNT	Graphite	Artificial sea water	∼1	Diameter= ∼10–20μm
[139]	TNT	rGO	9:1 sea water and BBS	0.40	
[139]	TNT	rGO-Hydr.	9:1 sea water and BBS	0.50	Loss of aromaticity
[140, 145]	TNT	rGO-ST	BBS	/	C/O =24.1
[140, 145]	TNT	rGO-HO	9:1 sea water and BBS	/	C/O =18.22
[140, 145]	TNT	rGO-HO	BBS	/	C/O =18.22
[140, 145]	TNT	rGO-HU	BBS	/	C/O =19.27
[134]	TNT	GO-LiClO$_4$	9:1 sea water and BBS	2.03	high in hydroxyls and carbonyls
[134]	TNT	GO-LiClO$_4$	BBS	6.74	high in hydroxyls and carbonyls
[134]	TNT	GO-Na$_2$SO$_4$	9:1 sea water and BBS	3.85	epoxies, hydroxyls, carboxyls and carbonyls
[134]	TNT	GO-Na$_2$SO$_4$	BBS	6.54	epoxies, hydroxyls, carboxyls and carbonyls
[142]	TNT	N-doped graphene	Artificial sea water	0.03	rich in pyridine-like N
[141]	TNT	N,S-codoped rGO nano-ribbon	0.1M PBS with 0.4M KCl	0.0001	Oxygen-containing groups, pyridinic and pyrrolic N, thiophene and oxidised thiophene

[a] Electrode notations: GC – glassy carbon electrode; GO-LiClO$_4$ – graphene obtained by electrochemical exfoliation with lithium perchlorate; GO-Na$_2$SO$_4$ – graphene obtained by electrochemical exfoliation with sodium sulphate; rGO – obtained by thermal reduction of graphite oxide in an argon atmosphere; rGO-Hydr. – obtained by thermal reduction of graphite oxide in a saturated H$_2$ atmosphere; rGO-

ST – thermally reduced graphene oxide obtained with Staudenmaier procedure; rGO-HO – thermally reduced graphene oxide obtained with the Hofmann procedure;rGO-HU – thermally reduced graphene oxide obtained with Hummers procedure; G-SL – single-layered graphene nanoribbons; G-FL – few-layered graphene nanoribbons; G-ML – multi-layered graphene nanoribbons.
[b] Experimental conditions notations: BBS – borate-buffered saline; artificial sea water – 0.5 M NaCl solution; PBS – phosphate-buffered saline.

A direct comparison between the sensing performance measures of different materials is complicated by the lack of standard testing conditions (see Table 4.1), hindering efficient development of improved sensors. Therefore, clear design guidelines based on a systematic understanding of the GBMs chemistry involved in sensing are needed. In the case of NO_2 detection, a sensor's LOD was shown to be quantitatively correlated with the computed adsorption energies and band gap of graphene oxide [146]. Non-covalent interactions are thought to be crucial in sensing organic molecules with GBMs, influencing the transport properties of a sensor [147, 148], determining sensitivity and selectivity of the analysis [80], and defining the design principles for high-performance carbon-based sensors [80, 134]. As already discussed above, the nature of the NCIs is defined by the structures and compositions of the sensor material and the contaminant being detected [80]: pristine graphene and derivatives with a high degree of aromaticity interact with nitroaromatic analytes primarily through $\pi - \pi$ stacking, while less or non-aromatic variously functionalised graphene derivatives (e.g., reduced graphene oxide and heteroatom-doped graphene) can form additional hydrogen bonds and other electrostatic interactions [149]. According to a Fourier transform infrared spectroscopy study, the adsorption of nitroaromatic compounds is weaker on graphene oxide (given its hydrophilicity and reduced aromaticity) and stronger on reduced graphene oxide (due to the combination of π-stacking and electrostatic interactions with its numerous oxygenated functional groups) [149]. Computational studies of the interactions between organic molecules and graphene derivatives (see Table 4.2 for an overview) lead to similar observations and showcase the variety of computational methods used to simulate these systems.

Table 4.2: Prior computational studies on the adsorption of aromatic substrates on GBMs.

Ref	System	Model	Level of theory
[150]	Benzene/toluene on single- and multi-layered defective graphene	Periodic	vdW-corrected DFT
[151]	Methylbenzenes on graphene	Periodic	vdW-corrected DFT
[148]	Aminoacids on graphene	Periodic	DFT-D3
[152]	Aminoacids on graphene	Nanoflake	M06-2X
[153]	Organic dyes on graphene oxide	Periodic	(GGA)AIMD + DFT-D3
[154]	Aromatic organic molecules	Periodic	Dispersion-corrected DFT
[155]	Biomolecules on graphene	Nanoflake, periodic	M06-2X, Dispersion-corrected DFT
[48]	Small organic molecules on graphene	Nanoflake, periodic	Empirical, DFT, and WFT
[56]	Aromatic organic molecules on graphene	Nanoflake	B3LYP

Once a nitroaromatic compound is adsorbed on a sensor's surface, its electrochemical detection proceeds *via* a stepwise four-electron reduction of NO_2 groups to amines [134]. The electrochemical signal is therefore largely determined by the redox characteristics and conductivity of the sensor material. Overall, both the initial adsorption (this Chapter) and the subsequent reduction (**Chapter 5**) of a NAC on the GBM define the sensor's performance. However, the specific weight that each of these steps plays in the sensing efficiency is yet to be clarified. In this Chapter, we test computational protocols for quantifying and analysing NCIs between NACs and GBMs in the context of electrochemical sensing. We also probe the ability of the extrapolation scheme, developed in **Chapter 3**, to predict the strength of the adsorption for an arbitrarily large surface model. Finally, we aim to determine how functionalisation of the GBM impacts its adsorbent properties with respect to NACs.

4.2 Computational methods and models

4.2.1 GBM models

Interaction energies between nitroaromatic compounds DNT and TNT and model graphene-based materials were computed for circular-shaped nanoflakes across a range of sizes: from the smallest, coronene, to the largest, $C_{384}H_{48}$ (see Fig.4.2a). In addition to pristine graphene, G, we investigated two variants of reduced graphene oxide, rGO-ST and rGO-HU-HO, several combinations of boron and nitrogen (co-)doping, and hexagonal boron nitride (hBN) (see Fig.4.2b). hBN is another important two-dimensional material; it has similar properties and the same structure as pristine graphene, but its lattice is composed of alternating boron and nitrogen atoms [156, 157]. In this work, it was selected as an "fully codoped" graphene in order to explore the effect of increasing the number of dopant atoms. The amount of functional groups or dopant atoms per model is the same independent of the model size. The size of the models was increased by adding sp²-hybridised carbon atoms around the smaller models, maintaining the circular shape and keeping the functionalised area in the center of the nanoflake. This was done to study the size-dependency for a fixed number of dopant atoms and functional groups, and to minimise the edge effects. For periodic models, a pristine graphene supercell containing 98 carbon atoms was chosen. Functional groups and doping atoms were then introduced to produce models for all other investigated materials, and the functionalised/doped are was again positioned at the center of the model (see Fig.4.2c).
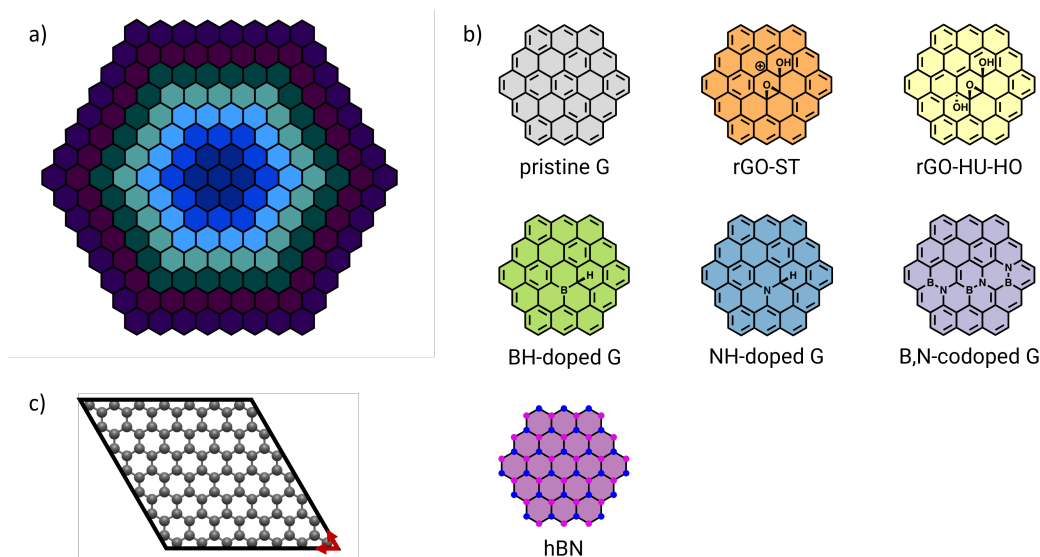
Figure 4.2: a) Investigated model sizes: size 0 – dark blue, size 1 - dark blue plus lighter blue, and so on up to size 6. b) Models of investigated GBMs, shown for size 1 and colour-coded according to their chemical nature. This colour code is used for all the plots in this Chapter. c) Supercell of pristine graphene, used to model periodic GBMs.

4.2.2 Theoretical procedures

For the model size 1 (circumcoronene) of each GBM, GFN2-xTB was used in the framework of metadynamics [69] with the root mean square deviation (RMSD) as a metric for collective variables to find stable analyte-sensor complexes and compute their relative energies. Simulations were performed at 298 K for 20 picoseconds with a 1 femtosecond step using the xtb software.[69] 400 frames were obtained for each complex. Nanoflake models were constrained with a force constant of 10 Hartree; spherical *logfermi* potential was applied to avoid the dissociation of the non-covalently bound complexes. RMSDs were evaluated for 20 structures with a scaling factor of 0.02. These parameters were chosen as a good compromise between an extensive sampling of the potential energy surface and a reasonable computational time [69]. For each complex, structures within 20 kJ mol⁻¹ of the lowest energy conformation at the MTD(RMSD)/GFN2-xTB level were chosen for a subsequent energy refinement at a PBE0-D3 /def2-TZVP level of theory with the resolution of identity approximation (RIJCOSX) approximation in ORCA [102]. For each GBM with model

size 1, structure with the lowest PBE0-D3-RIJCOSX//GFN2-xTB energy was assumed to be the lowest-energy adsorption complex and used for subsequent investigation.

For each GBM, other model sizes were constructed from the obtained lowest-energy adsorption complexes of size 1 by removing (size 0) or consecutively adding (sizes 2-6) outer benzene rings and relaxing these structures at the GFN2-xTB level of theory. For all model sizes using relaxed GFN2-xTB geometries, interaction energies were then computed at the GFN2-xTB level of theory [64] as implemented in DFTB+ [158]. For model sizes 0-3, interaction energies were also computed at the PBE-D3-RIJCOSX/def2-TZVP level using ORCA; these single-point PBE computations for larger models were prohibitively computationally expensive, particularly in terms of required random access memory. In all cases, interaction energy was computed as the difference between the energy of the complex and the energies of its isolated components.

For the model size 1, we also performed full geometry relaxation at the PBE0-D3-RIJCOSX level of theory to assess the quality of semiempirical geometries. Correspondingly, for both the GFN2-xTB and PBE0-D3 geometries of this model size, we computed the interaction energies at several levels of theory, namely

- GFN2-xTB geometry: GFN2-xTB [64] as implemented in DFTB+ [158], PBE-D3-RIJCOSX/def2-TZVP and B3LYP-D3-RIJCOSX/def2-TZVP using ORCA [102], and SAPT0/jun-cc-pVDZ with the density fitting approximation [159] as implemented in the Psi4 package [106];

- PBE0-D3-RIJCOSX/def2-TZVP geometry: PBE-D3-RIJCOSX/def2-TZVP and PBE0-D3-RIJCOSX/def2-TZVP using ORCA, and SAPT0/jun-cc-pVDZ in Psi4.

Periodic models of GBMs were constructed using a 7×7 supercell approach. Computations were performed at the PBE-D3 level of theory with pseudopotentials from the PSLibrary [108] using Quantum Espresso [107]. An energy cutoff of 90 Ry for the plane wave expansion of the wavefunction was selected together with a 3 ×3×1 *k*-point grid.

For model size 1, the non-covalent interactions were additionally studied with a density-dependent scalar field, *i.e.*, the density-overlap regions indicator, which allows simultaneous characterisation and quantification of both covalent and non-covalent interactions [75]. DORI was computed at the PBE0-D3/DZP level of theory in conjunction with the PBE0-D3-RIJCOSX/def2-TZVP geometries using ADF [160].

Finally, solvent effects in water were evaluated for model size 1 using a continuum solvent model at the PCM-UAKS/PBE0/6-31G(d) level of theory in conjunction with the PBE0-D3-RIJCOSX/def2-TZVP geometries using Gaussian 16 [161]. Solvent correction to the interaction energy for a given system was computed as the difference between the solvation energy of the complex and solvation energies of its isolated components, and corrected for the phase change.

4.3   Results and discussion

4.3.1   Adsorption geometry

To assess the impact the chosen level of theory has on the adsorption geometry, we compared the shortest distances between the C-atom of the NAC phenyl ring and the closest non-hydrogen atom of the GBM in the optimised GFN2-xTB and PBE0-D3 geometries in model size 1 and in the PBE-D3 geometries on the periodic model (Table 4.3). We note that the results from PBE0-D3 on model size 1 and PBE-D3 on periodic model are in good quantitative agreement with each other. However, semiempirical geometries across all studied GBMs feature significantly smaller intermolecular separations, *i.e.*, 0.4-1.0Å shorter than the corresponding PBE0-D3 values. This is somewhat surprising considering that GFN2-xTB was developed to, among other reasons, fix the tendency to overbind non-covalent interactions in GFN1-xTB [64]. Yet, similar overbinding by GFN2-xTB compared to pure DFT was recently reported for the corannulene-fullerene system [162].

4.3.2   Interaction energies: method assessment

The relationship between a bond's length and its strength is the subject of a long-standing debate in chemistry, relevant also to the non-covalent interactions. Considering the overbinding of the

Table 4.3: Intermolecular distances in the obtained geometries of NAC-GBM complexes.

System	Periodic (PBE-D3)		size 1 (PBE0-D3/def2-TZVP)		size 1 (GFN2-xTB)	
	DNT	TNT	DNT	TNT	DNT	TNT
pristine graphene	3.48	3.52	3.43	3.41	3.00	2.91
rGO-ST	3.47	3.43	3.62	3.37	2.89	2.81
rGO-HU-HO	3.43	3.47	3.37	3.24	2.63	2.54
BH-doped	3.54	3.58	3.55	3.49	2.82	2.80
NH-doped	3.55	3.45	3.42	3.54	3.02	2.98
B,N-codoped	3.46	3.48	3.37	3.35	2.88	2.77
hBN	3.52	3.66	3.41	3.48	2.92	2.87

investigated complexes at the GFN2-xTB level compared to DFT, we next examined whether this translates to the interaction energies (Figure 4.3). Obtained results lead to the following observations:

- somewhat counter-intuitively, when the same level of theory, e.g., PBE-D3, is applied to GFN2-xTB and PBE0-D3 geometries, the former, despite featuring significantly shorter intermolecular interactions, results in notably weaker (by as much as 80 kJ mol^{-1}) interaction energies;

- when the same method is used for both the energy and geometry, *i.e.*, PBE0-D3-RIJCOSX/def2-TZVP//PBE0-D3-RIJCOSX/def2-TZVP or GFN2-xTB//GFN2-xTB, the interaction energies from the two methods are much closer to each other for most systems, although deviations as high as 37 kJ mol^{-1} do occur in several cases;

- interestingly, SAPT0 interaction energies appear to be relatively insensitive to the underlying geometries, with the exception of the rGO-ST system.

	Method 1	Method 2	Mean AD	Max AD
🔵	PBE0-D3	GFN2-xTB	14.7	37.2
🔴	PBE-D3	PBE-D3	53.3	82.2
🟠	SAPT0	SAPT0	9.9	38.6
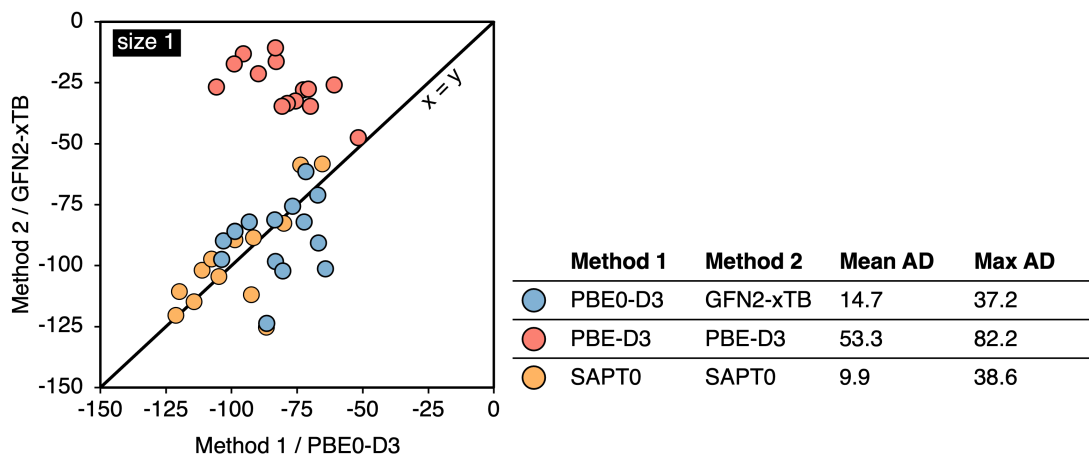
Figure 4.3: Interaction energies for model size 1 of the investigated GBMs, computed using several combinations of the levels of theory and GFN2-xTB and DFT geometries. The Table contains the legend and the mean and maximum absolute deviations in interaction energies between the two methods (kJ mol^{-1}).

While PBE0-D3 geometries should, in principle, be more reliable than the GFN2-xTB ones, they also come at steeper computational cost. At least three model sizes are required to probe the extrapolation scheme. Model size 0 (coronene) is subject to strong edge effects, therefore sizes 1-3 would satisfy this minimal requirement. Yet, PBE0-D3 geometry optimisations become prohibitively expensive and essentially impossible above model size 2. In other words, we can only explore the size dependency of the non-covalent interaction energies in the NAC-GBM systems if we resort to GFN2-xTB geometries. Results in Figure 4.3 indicate that SAPT0 energies for

the GFN2-xTB geometries provide reasonable accuracy, followed by GFN2-xTB. However, the same bottleneck of insurmountable computational cost applies to performing SAPT0 on larger model sizes. As is further shown in Figure 4.4, DFT energies, computed with GFN2-xTB, are in complete disarray with respect to SAPT0/jun-cc-pVDZ//GFN2-xTB data. Consequently, GFN2-xTB//GFN2-xTB approach appears to be the only affordable and to some extent reliable method to explore the size dependency of the interaction energy *via* the extrapolation scheme.

Method	Mean AD	Max AD
B3LYP-D3	54.5	83.8
PBE-D3	70.1	103.1
GFN2-xTB	25.9	65.0
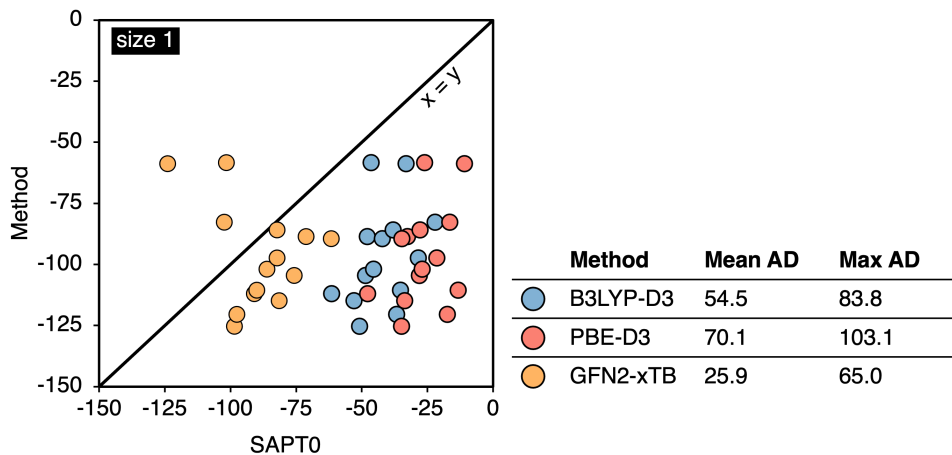
Figure 4.4: Interaction energies for model size 1 of the investigated GBMs, computed in conjunction with the GFN2-xTB using various methods. The Table contains the legend and the mean and maximum absolute deviations in interaction energies between the two methods (kJ mol^{-1}).

4.3.3　Adsorption on periodic GBMs

Using the extrapolation scheme, established in **Chapter 3**, we have estimated interaction energies of DNT and TNT with the infinitely large GBMs at the GFN2-xTB level (Fig.4.5, top panel). We note that all linear regressions have high coefficients of determination (R^2 >0.75), with the exception of DNT on rGO-ST (R^2 = 0.34). As could be expected, for all investigated graphene-based materials, the interaction energy decreases, *i.e.*, the NCIs strengthen with the increasing size of the nanoflake. However, the rate of this change varies with the chemical nature of the material. In B- and N-containing systems specifically, stabilisation grows much faster with size (*i.e.*, larger slope of the linear regression fit) than in pristine and oxidised graphenes. If these results are to be trusted, they would imply that competitive (selective) adsoption can be modulated through the nanoflake size.

However, GFN2-xTB extrapolated interaction energies do not follow the same trend as those obtained from the periodic PBE-D3 computations (Fig.4.5, bottom panel). Estimates from extrapolation reveal a steady, and, arguably, chemically intuitive increase in stabilisation with the increasing extent of B,N-doping, *i.e.*, pristine G < BH-doped G < NH-doped G < B,N-codoped G < hBN. Periodic simulations also predict the strongest interactions with the hBN, followed, however, by rGO-ST, with the rest of the materials affording adsorptions of similar strengths.

4.3.4　Solvent effect

In real-life practical applications, *i.e.*, electrochemical detection of nitroaromatic pollutants in waste or ground water, the sensor is submerged in water. Thus, the analyte-sensor interactions are subject to solvent effects. To gain the first insight into the magnitude and direction of these effects, we have estimated them for model size 1 using the continuum solvent model (Fig. 4.6). We find that for all GBMs, the solvent destabilises their complexes with NACs by *ca.* 20-80 kJ mol^{-1}. This destabilisation is greater in pristine and B-doped graphene than in O- and N-containing derivatives.

4.3.5　Physical origins of the physisorption

To further explore the physical nature of the non-covalent interactions between investigated GBMs and nitroaromatic compounds, we performed the energy decomposition analysis of the total inter-
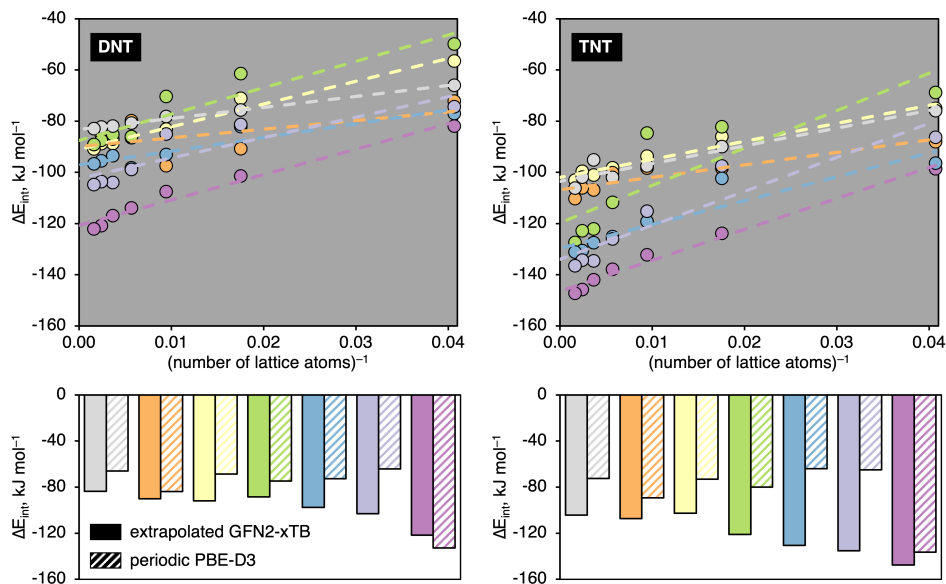
Figure 4.5: Top panel: GFN2-xTB interaction energy as a function of the model size (circles), as well as linear extrapolations ($y = m \times x + b$, dashed lines) to an infinite material for adsorption of DNT (left) and TNT (right). Bottom panel: Interaction energies of DNT (left) and TNT (right) with infinitely large GBMs, as predicted from extrapolated GFN2-xTB results (solid) and from periodic PBE-D3 computations (striped).
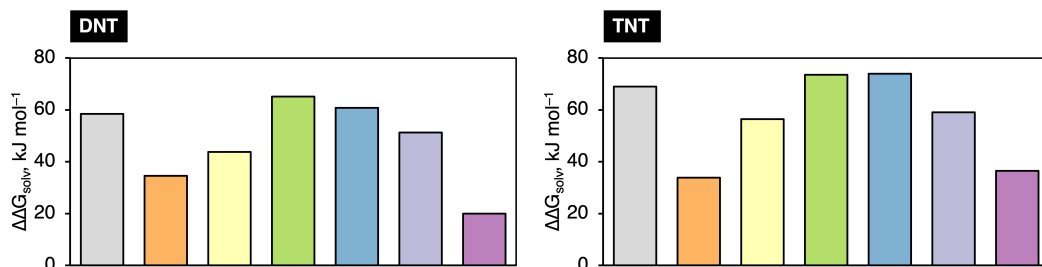
Figure 4.6: Solvent effects on interaction energies (kJ mol^{-1}), computed from PCM-UAKS/PBE0/6-31G(d)//PBE0-D3-RIJCOSX/def2-TZVP free energies of solvation in water at 25°C for DNT (left) and TNT (right).

action energies in the model size 1 complexes using symmetry-adapted perturbation theory (Fig. 4.7). We find for all systems that exchange is the only repulsive component to the interaction energy. Electrostatic effects can be largely attributed to the interactions of the polar NO$_2$ groups of DNT and TNT with the GBMs; yet, the largest stabilisation arises from dispersion. Comparing investigated graphene derivatives, all contributions to the interaction energy are amplified in rGO-ST compared to rGO-HU-HO, and are diminished in hexagonal boron nitride compared to pristine and B-,N-doped graphene.

The density overlap region indicator (DORI) was employed to gain further insights into the investigated interactions (Fig. 4.8). With DORI, the intermolecular interactions can be (1) visualised as DORI domains, (2) analysed by colouring the corresponding isosurfaces with sgn(λ2)ρ(r) to distinguish between attractive and repulsive forces, and (3) indirectly quantified by integrating the electron density within a given DORI domain. In all studies systems, a single large DORI domain between the NAC and the basal plane of the material fully captures the intermolecular interaction. The most pronounced feature of the B,N-codoped complexes is the electron density overlap between the methyl group of the NAC and the GBM surface, greater compared to that in pristine graphene and hBN complexes. This suggests that the propensity to establish dispersion-driven CH–π interactions is enhanced in systems involving particular B–N–C patterns.
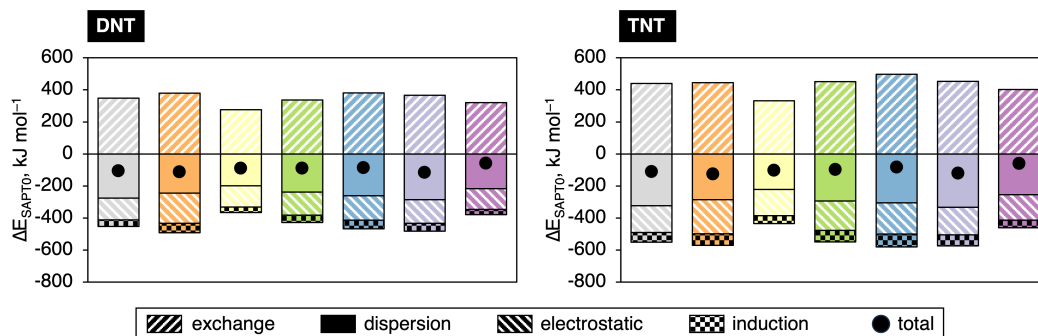
Figure 4.7: Total interaction energies and their components in model size 1 for DNT (left) and TNT (right), computed at the SAPT0/jun-cc-pVDZ//GFN2-xTB level of theory.
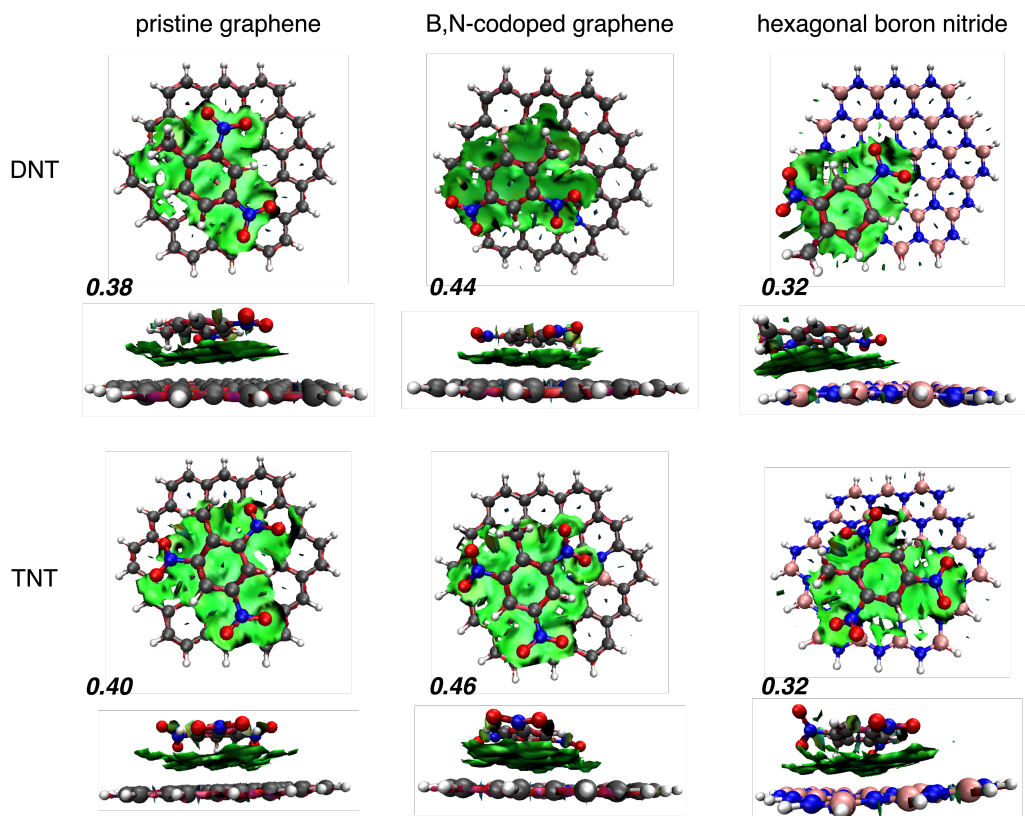
Figure 4.8: DORI = 0.98 isosurfaces for selected NAC-GBM complexes with model size 1, views from above and along the basal plane of the GBM model. Isosurfaces are colour-coded with $sgn(\lambda^2)\rho(r)$ in the range from -0.01 au (red) to 0.01 au (blue). Bold italic numbers are electron density integrals over $V^{DORI=0.98}$ intermolecular interaction domains.

4.4   Conclusions

The non-covalent interactions responsible for the physisorption of nitroaromatic pollutants on the surface of graphene-based electrochemical sensors are crucial to detector performance. Employing a combination of semiempirical density functional tight-binding in the framework of metadynamics to explore the structural space of physisorption with DFT, and symmetry-adapted perturbation theory to assess its energetics, we have analysed these interactions for a series of finite and periodic models of various graphene-based materials with two prototypical nitroaromatic contaminants, dinitro- and trinitrotoluene. This study heads toward a deeper understanding of the chemistry and physics underlying electrochemical sensing with GBMs, with the ultimate aim to deduce the guidelines for the design of better sensors applicable to a wider scope of analytes. As a first step on this path, we tested a range of theoretical approaches, from semiempirical tight-binding and "pure"

DFT to symmetry-adapted perturbation theory in finite and periodic settings. Our results revealed concerning disagreements between these various methods, in particular, large deviations in DFT interaction energies depending on the underlying geometry, *i.e.*, DFT *versus* DFTB. We note that the latter yielded noticeably overbound complexes, as quantified by the intermolecular distances. On the other hand, SAPT results were found to be largely independent on the geometries - an observation that, to the best of our knowledge, has not been addressed in the published literature so far. Overall, the issue of how to simulate the adsorbent properties of graphene-based materials both accurately (at least on a qualitative level) and efficiently (given that SAPT and hybrid-GGA DFT are only applicable to small nanoflake models) warrants continued investigation.

Using the best affordable methodologies, we next tested the extrapolation scheme for predicting adsorption energetics on infinitely large graphene derivatives. Obtained results are in agreement with those from the periodic DFT in terms of the weakest and strongest binding. Surprisingly, the size dependency of the interaction energy was found to be dependent on the chemical nature of the substrate. Specifically, stabilisation grows "faster" with increasing graphene nanoflake size in B- and N-doped materials, and slower in oxidised graphene. We stress that nanoflakes of various sizes used in this work differ only by the amount of outer benzene rings around a single chemical functionality within a flake. In other words, only the edge effects and the extent of electron delocalisation vary across model sizes. This peculiar phenomenon, which can potentially be utilised in size-selective nanographene-based sensors and catalysts, has not been reported yet.

Finally, among several graphene-based materials explored, the strongest interactions are consistently predicted for B,N-codoped graphene and hexagonal boron nitride. These materials have not been tested in electrochemical sensing and transformation of nitroaromatics pollutants yet. Provided these systems can efficiently reduce NACs (we investigate these properties in **Chapter 5**), our findings suggest they can be promising new materials for nitroaromatics detection.

Overall, this study demonstrated concerning discrepancies in the performance of computational methods, revealed unexpected trends in the size dependence of the interaction energies, and shed light on the role and the nature of non-covalent interactions in the sensing process. However, our conclusions are subject to several limitations. On the one hand, more homogeneous experimental data is necessary to benchmark computational methods. On the other, further theoretical assessments are needed to simulate materials with a realistic content of functional groups and dopant atoms in the graphene lattice, evaluate the contribution of environmental effects (e.g., solvation beyond continuum solvent models, loadings of analyte, etc.) and elucidate the importance of the subsequent steps in electrochemical sensing.

A manuscript reporting the findings of this Chapter is currently in preparation. A preprint version is available at https://doi.org/10.26434/chemrxiv.14364800.v2.

Chapter 5

Redox properties of graphene-based materials

5.1   Introduction

Recent developments in materials engineering enable accurate synthesis of systems with desired size, functionalisation, and defects [163, 164, 165]. The only practically viable way to explore this vast chemical space is through computation [166]. Electronic structure theory [167], multiscale modelling [168], machine learning [169], and several other approaches are used to understand and predict properties of materials. The obtained information is then employed to design *in silico* new materials or to screen large databases to select good candidates for a certain application [166, 50], reducing the amount of lengthy and expensive experimental testings. Carbon-based materials, including nanotubes, fullerenes, and graphene, are promising and sustainable candidates to substitute transition metals and other inorganic counterparts not only as sensors, but also as catalysts [170] and electronic components [171]. Graphene nanoflakes, defined as nanoparticles of less than 100 nm in diameter comprising a single or few layer graphene, were discovered shortly after graphene itself, in 2008 [172]. Graphene nanoflakes already play an important role in the carbon-based materials family. They are characterised by non-zero band gaps and good dispersability, and their properties are easily tunable *via* functionalisation. In graphene nanoflakes, quantum confinement and edge effects [173] arise because of their nanometer dimensions. The unique features of graphene nanoflakes are responsible for their various applications in solar cells, batteries, catalysis, imaging, and sensing [9].

Electronic structure of materials and molecules is crucial in the development of more efficient and sustainable batteries [174, 175] and catalysts [176, 177]. For example, the detection of nitroaromatics by GBM-based sensors (**Chapter 4**) involves a sequence of electrochemical transformations. These processes are also relevant to GBM-based electrocatalytic systems, in which the NO_2 groups are converted to NH_2 groups by a reducing agent. The GBM is assumed to facilitate the catalysis by adsorbing the NAC molecule and shuttling the electrons throughout the system (Fig.5.1) [178, 179]. In both electrochemical sensing and catalysis, the first electron transfer is considered to be the rate-determining step [180]. Therefore, understanding how electronic (*i.e.*, ionisation energy and electron affinity) and redox (e.g., reduction potential) properties of graphene nanoflakes depend on their size, functionalisation, and doping is crucial for enhancing their performance in electrochemical applications.

Electronic properties of graphene nanoflakes and similar nanoparticles have been explored *in silico*, with the focus on how these properties vary with the size of the system [52, 53, 54, 55] or with the functionalisation [181]. For coronene, an EA of 0.47±0.09 eV was measured *via* photoelectron spectroscopy [55]. An overview of computed and experimental values reported in the literature for grpahene nanoflakes is presented in Table 5.1.

In extended conjugated polycyclic molecules, presence of numerous degenerate or near-degenerate states can lead to strong static electronic correlation [184, 185], posing considerable challenge for modeling electronic properties of graphene nanoflakes. While the wavefunction theory based-methods such as configuration interaction [186], many-body perturbation theory [187], multiconfiguration self-consistent field [188], quasidegenerate perturbation theory [189], and multireference configuration interaction [188] or coupled cluster [190] methods have been developed
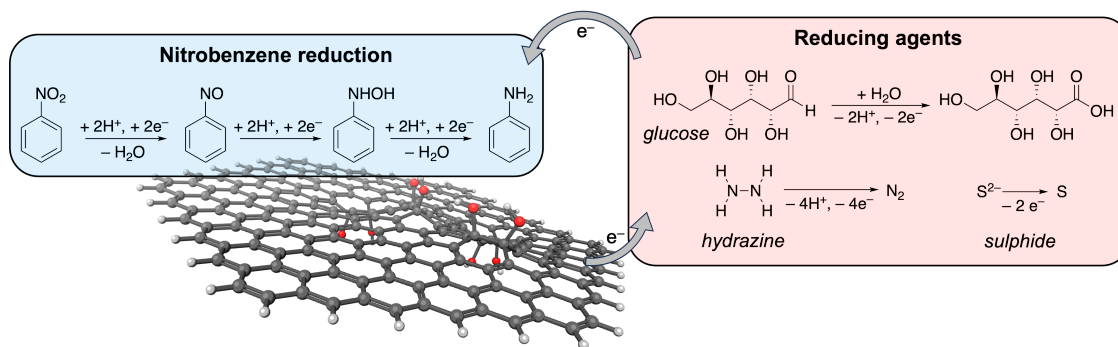
Figure 5.1: General scheme of the reduction of NACs by GBMs.

Table 5.1: Summary of computed electronic properties of graphene nanoflakes, reported in the literature.

Ref.	GBM	Method	Properties
[52]	Pristine graphene size 0	TAO-LDA/6-31G	Vertical IP=6.72 eV Vertical EA=0.58 eV
[52]	Pristine graphene size 1	TAO-LDA/6-31G	Vertical IP=5.81 eV Vertical EA=1.70 eV
[52]	Pristine graphene size 2	TAO-LDA/6-31G	Vertical IP=5.30 eV Vertical EA=2.35 eV
[52]	Pristine graphene size 3	TAO-LDA/6-31G	Vertical IP=4.99 eV Vertical EA=2.77 eV
[51]	Pristine graphene size 0	B3LYP/6-31+G	Vertical IE=7.08 eV
[51]	Pristine graphene size 1	B3LYP/6-31+G	Vertical IE=6.35 eV
[182]	Boron-nitrogen codoped coronene[a]	B3LYP/6-31+G	Vertical EA (circle)=0.75 eV Vertical EA (stripe)=1.52 eV Vertical IE (circle)=6.67 eV Vertical IE (stripe)=5.57 eV
[183]	Single graphitic nitrogen coronene	B3LYP/DND	Fundamental gap= 4.20 eV

[a] the heteroatoms substitute the central benzene ring (circle) or 3 adjacent rings (stripe)

to treat strongly correlated systems, their high computational costs makes them applicable to only relatively small compounds [191]. Instead, thermally-assisted-occupation DFT [192] provides a more reliable description of complex electronic structure at a computational cost similar to that of DFT. In classical DFT, the error due to static correlation was found to either be independent of the functional [193], or to display an "erratic behaviour" [194]. When simulating graphene nanoflakes it is therefore necessary to find a good balance between an acceptable computational cost, given the large size of the molecules, and an accurate description of the electronic behaviour to avoid large errors.

Many metrics have been developed to analyse and quantify electron correlation and to evaluate the quality of the wavefunction [195]. The eigenvalues of the spin operator $\hat{S}^2$ are habitually used to assess the extent of spin contamination present in the system [196]. Grimme *et al.* [197] developed a tool based on fractional occupation number weighted density (FOD) and finite-temperature DFT calculations with pre-defined electronic temperature that allows both the quantification and visualization of static electron correlation effects. An electron correlation diagnostic for single-reference coupled-cluster methods is the T_1 value [198], which corresponds to the Frobenius norm of the single substitution amplitudes t_1 vector of the closed-shell CCSD wavefunction, normalised by the number of correlated electrons.

In **Chapter 4**, we have explored the adsorbent properties of GBMs in the context of their applications in electrochemical sensing. Completing this picture, in this Chapter we investigate the other part of the sensing process, *i.e.*, the capability of the sensor material to shuffle electrons. Specifically, we examine how ionisation energies, electronic affinities, and solvation energies (which convert EAs and IEs into redox potentials) vary with the size and chemical composition of graphene-

based nanoflakes using range-separated DFT and the SMD continuum solvent model. As before, we aim to identify reliable modelling protocols and arrive at structure-property relationships, which can guide subsequent design and experimental testing of new and improved graphene-based materials for electrochemical applications.

5.2 Computational methods and models

IEs, EAs, and solvation energies were computed for six graphene-based materials, namely:

- Pristine graphene;

- Epoxide-functionalised graphene (epoxide rGO);

- Boron-doped graphene (BH-doped G);

- Graphene codoped with boron and nitrogen (1,1-B,N-codoped G);

- Nitrogen-doped graphene (NH-doped G);

- Phosphorus-doped graphene (PH-doped G).

These systems were modelled as circular nanoflakes of four sizes, coronene being the smallest (Fig.5.2). In the case of doped and functionalised graphene nanoflakes, the number of functionalities was increased with the size of the system so as to maintain experimentally observed elemental composition.
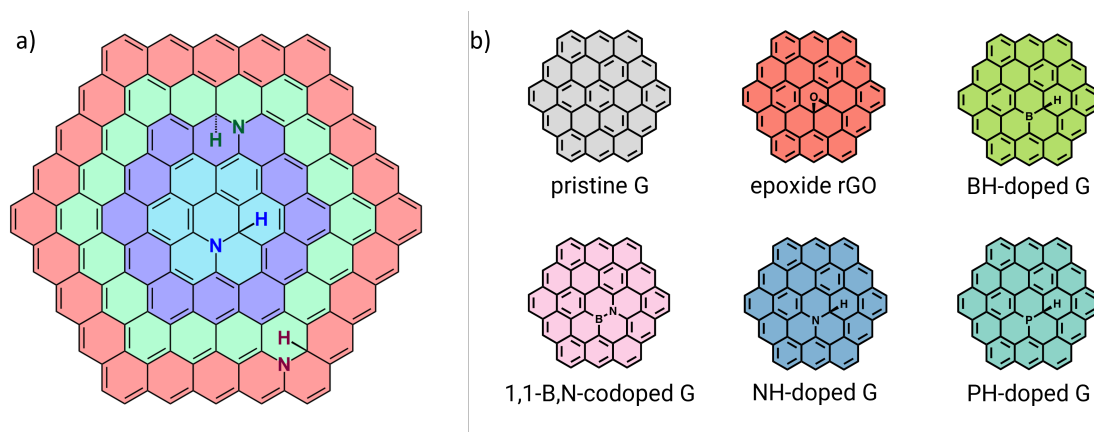
Figure 5.2: a) Investigated model sizes illustrated for NH-doped graphene: size 0 – light blue, size 1 - size 0 plus light blue, size 2 - size 1 plus light green, size 3 - size 2 plus red. b) Models of investigated GBMs, shown for size 1 and colour-coded according to their chemical nature. This colour code is used for all the plots in this Chapter.

All computations were performed with the Gaussian 16 software [161] using the range-separated ωB97X-D functional with the def2-TZVP basis set. This DFT method includes 22% Hartree-Fock exchange at short range and 100% Hartree-Fock at long range [199, 200]. To examine the role of exact exchange within the functional formulation, EAs and IEs were also computed at the PBE-D3BJ (0% of HF exchange) [95, 96, 201], TPSSh-D3BJ (10% HF exchange) [202], B3LYP-D3BJ (20% of HF exchange)[97], and M06-2X (54% of HF exchange) [203] levels of theory, all with the def2-TZVP basis set. All computations on open-shell species were performed within an unrestricted formalism. We chose the SMD/IEF-PCM implicit model for solvation in water [79] with an electrostatic scaling factor of 1.2; this method additionally allows decomposing solvation energy into solute-solvent dispersion interaction, solute cavitation, and solute-solvent repulsion. For all computations, a tight self-consistent field optimisation and a fine integration grid were employed, except for M06-2X which requires an ultra-fine grid setting [204]. Wavefunction stability analysis was also performed for all systems.

We computed both the vertical (the energy of the radical ion is computed in the geometry of the neutral state) and the adiabatic (the geometry of the radical ion is fully relaxed) IE and EA values, defined according to the following one-electron reactions:

$$\text{GBM} \rightarrow \text{GBM}^{+\cdot} + e^- \tag{5.1}$$

$$\text{GBM} + e^- \rightarrow \text{GBM}^{-\cdot} \tag{5.2}$$
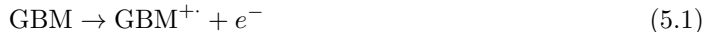
Correspondingly,

$$\text{IE} = E_{\text{cation}} - E_{\text{neutral}} \tag{5.3}$$

$$\text{EA} = E_{\text{neutral}} - E_{\text{anion}} \tag{5.4}$$

The quality of the wavefunction for all systems was monitored through the expectation value of the $\hat{S}^2$ operator in conjunction with the geometry of the parent neutral closed-shell state. The extent of static electron correlation was quantified and visualised with the fractional occupation density number (N_{FOD}) [197] at the TPSS/def2-TZVP level of theory with a smearing temperature of 5000K, as implemented in ORCA 5.0.3 [102].

5.3 Results and discussion

5.3.1 Ground-state electronic structure of nanographenes

In polycyclic conjugated molecules, such as linear acenes, the ground-state multiplicity tends to switch from closed-shell to open-shell diradical with an increasing number of rings [205]. Since the same can take place in nanographenes, we first focused on exploring their ground-state electronic structure. We used the fractional occupation density number (N_{FOD}) to quantify the extent of static correlation, symptomatic of the multireference character of the parent nanographenes (neutral and closed-shell). While there is no fixed threshold for N_{FOD}, values below *ca.* 1.0 signify that a single determinant is reasonably reliable. Our results, reported in Table 5.2, show that static electronic correlation rises with the increasing model size, suggesting increasing diradical character in model sizes 2 and 3 [206].

Visualisation of the FOD results for pristine graphene models (Fig. 5.3) confirms the increase in electron correlation with the nanoflake size. For model sizes 0 and 1, there is no visible FOD and, therefore, the electronic structure can be well-represented by single-reference methods. Instead, small FOD lobes can be seen in model sizes 2 and 3, and their location suggest that static correlation occurs primarily at the edges of the large nanoflakes.
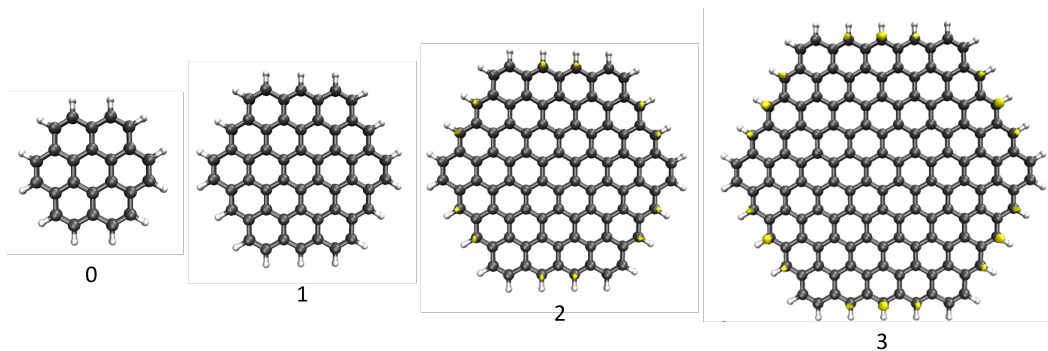
Figure 5.3: FOD plots (in yellow) with an isovalue of 0.005 e/Bohr^3 across model sizes of pristine graphene.

DFT partially captures the electron correlation *via* its exchange term. To demonstrate this, we have compared results obtained with ωB97X-D, which is a range-separated DFT including 22% of Hartree-Fock exchange at short distance and 100% at long distance, with PBE (0% exact exchange), TPSSh (10% exact exchange), B3LYP (20% exact exchange), and M06-2X (54% exact exchange), in conjunction with the def2-TZVP basis set. The effect that a growing amount of HF exchange plays in capturing correlation can be traced in the eigenvalues of the $\hat{S}^2$ operator (see

Table 5.2: Fractional occupation density number (N_{FOD}), computed at the TPSS/def2-TZVP level of theory with 5000K smearing temperature.

Material	Size	N_{FOD}
pristine graphene	0	0.3
	1	0.9
	2	2.0
	3	3.5
epoxide rGO	0	0.4
	1	1.0
	2	2.4
	3	3.7
BH-doped graphene	0	0.4
	1	1.1
	2	2.4
	3	4.1
1,1-B,N-codoped graphene	0	0.4
	1	1.0
	2	2.2
	3	3.6
NH-doped graphene	0	0.6
	1	1.2
	2	2.7
	3	4.6
PH-doped graphene	0	0.6
	1	1.2
	2	2.7
	3	4.7

Table 5.3). For doublet radicals, the expectation value of this operator should be exactly equal to 0.75 if the system is strictly single-reference. Our results illustrate that the more exact exchange is included in the functional, the more the expectation value of the $\hat{S}^2$ operator deviates from 0.75 (Fig. 5.4). In several cases, complete lack of HF exchange in PBE even resulted in unconverged computations. In line with the FOD diagnostic, model sizes 0 and 1 feature insignificant spin contamination, yet $\langle \hat{S}^2 \rangle$ eigenvalues consistently exceed 10% deviation from 0.75 in radical ions of model sizes 2 and 3.
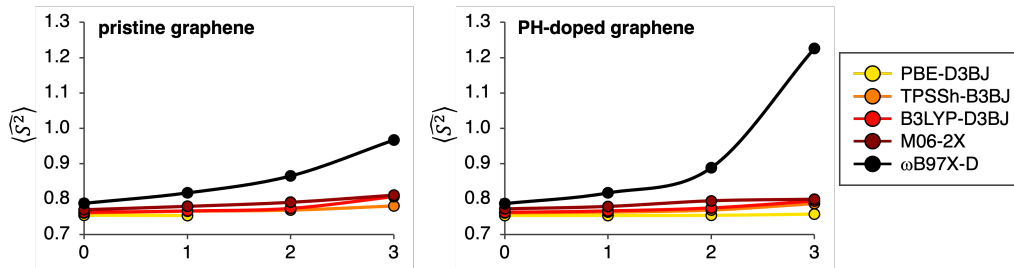
Figure 5.4: Eigenvalue of the $\hat{S}^2$ operator as a function of the model size obtained with different functionals and def2-TZVP basis set for the radical anions of pristine (left) and PH-doped (right) graphene, in the vertical process.

Table 5.3: Comparison of $\langle \hat{S}^2 \rangle$ eigenvalues, computed using various DFT functionals with the def2-TZVP basis set in the vertical scheme for radical ions across sizes and functionalisations of graphene models.

GBM	Species	Functional	Size 0	Size 1	Size 2	Size 3
pristine graphene	Cation	PBE-D3BJ	0.75	0.76	\\[a]	\\[a]
		TPSSh-D3BJ	0.76	0.77	0.77	0.79
		B3LYP-D3BJ	0.77	0.77	0.78	0.82
		M06-2X	0.78	0.78	0.80	0.84
		ωB97X-D	0.80	0.84	0.88	0.99
	Anion	PBE-D3BJ	0.75	0.75	\\[a]	\\[a]
		TPSSh-D3BJ	0.76	0.77	0.77	0.78
		B3LYP-D3BJ	0.76	0.77	0.77	0.81
		M06-2X	0.77	0.78	0.79	0.81
		ωB97X-D	0.79	0.82	0.87	0.97
epoxide rGO	Cation	PBE-D3BJ	0.76	0.75	0.76	0.76
		TPSSh-D3BJ	0.77	0.77	0.78	0.78
		B3LYP-D3BJ	0.77	0.77	0.79	0.79
		M06-2X	0.78	0.79	0.81	0.80
		ωB97X-D	0.80	0.84	0.94	0.94
	Anion	PBE-D3BJ	0.75	0.75	0.76	0.76
		TPSSh-D3BJ	0.76	0.76	0.78	0.78
		B3LYP-D3BJ	0.76	0.77	0.78	0.78
		M06-2X	0.77	0.78	0.80	0.80
		ωB97X-D	0.79	0.82	0.90	0.91
BH-doped graphene	Cation	PBE-D3BJ	0.76	0.76	0.76	0.76
		TPSSh-D3BJ	0.77	0.77	0.77	0.81
		B3LYP-D3BJ	0.77	0.77	0.78	0.82
		M06-2X	0.79	0.79	0.80	0.85
		ωB97X-D	0.81	0.85	0.88	1.22
	Anion	PBE-D3BJ	0.75	0.75	0.75	0.76
		TPSSh-D3BJ	0.76	0.77	0.77	0.80
		B3LYP-D3BJ	0.77	0.77	0.78	0.82
		M06-2X	0.77	0.78	0.79	0.84
		ωB97X-D	0.79	0.84	0.91	0.95
1,1-B,N-codoped graphene	Cation	PBE-D3BJ	0.76	0.76	0.76	0.76
		TPSSh-D3BJ	0.77	0.77	0.78	0.79
		B3LYP-D3BJ	0.77	0.77	0.79	0.80
		M06-2X	0.78	0.79	0.81	0.81
		ωB97X-D	0.80	0.84	0.95	0.99
	Anion	PBE-D3BJ	0.75	0.75	0.76	0.76
		TPSSh-D3BJ	0.76	0.77	0.77	0.79
		B3LYP-D3BJ	0.77	0.77	0.78	0.80
		M06-2X	0.77	0.78	0.80	0.82
		ωB97X-D	0.80	0.83	0.94	1.05
NH-doped graphene	Cation	PBE-D3BJ	0.76	0.76	0.76	0.76
		TPSSh-D3BJ	0.78	0.77	0.78	0.79
		B3LYP-D3BJ	0.78	0.78	0.79	0.79
		M06-2X	0.78	0.79	0.81	0.82
		ωB97X-D	0.81	0.86	0.99	1.11
	Anion	PBE-D3BJ	0.75	0.75	0.76	0.76
		TPSSh-D3BJ	0.77	0.77	0.78	0.79
		B3LYP-D3BJ	0.77	0.77	0.79	0.81

... Continued

GBM	Species	Functional	Size 0	Size 1	Size 2	Size 3
		M06-2X	0.79	0.79	0.82	0.85
		ωB97X-D	0.82	0.84	0.97	1.18
PH-doped graphene	Cation	PBE-D3BJ	0.75	0.75	0.75	0.76
		TPSSh-D3BJ	0.76	0.77	0.77	0.80
		B3LYP-D3BJ	0.76	0.77	0.78	0.80
		M06-2X	0.78	0.78	0.80	0.80
		ωB97X-D	0.79	0.83	0.92	0.90
	Anion	PBE-D3BJ	0.75	0.75	0.75	0.76
		TPSSh-D3BJ	0.76	0.76	0.77	0.79
		B3LYP-D3BJ	0.76	0.77	0.77	0.79
		M06-2X	0.77	0.78	0.80	0.80
		ωB97X-D	0.79	0.82	0.89	1.23

[a] unconverged computation

The presence of strong static electron correlation in larger nanoflakes is confirmed by visualising both the fractional occupation number weighted density and spin density, as shows in Figure 5.5 for size 2 of PH-doped graphene. Small localised FOD domains reside on the edge carbon atoms and close to the dopant atoms, while the spin densities are localised only on the latter sites. We can also clearly see how DFT functionals treat static correlation differently based on the amount of exact exchange (Table 5.3) by comparing the spin density plots at the PBE-D3BJ and ωB97X-D levels of theory (Figure 5.5b-c).
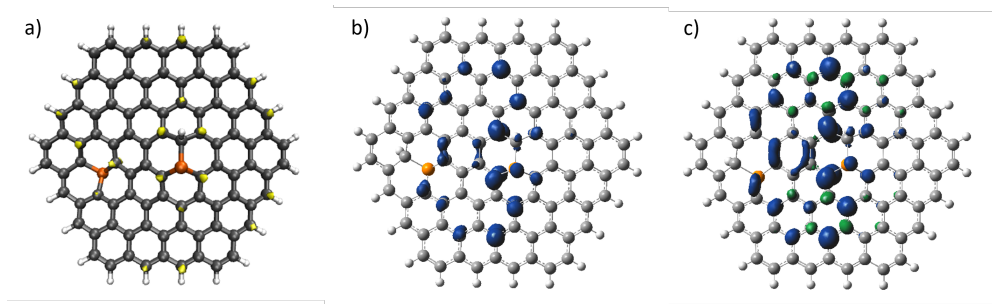
Figure 5.5: Static correlation in PH-doped graphene, model size 2: a) FOD plot with isovalue of +0.005 e/Bohr^3, b) spin density plots ($\pm$0.002 isovalue) computed at the PBE-D3/def2-TZVP and c) wB97x-D/def2-TZVP levels of theory, all in the vertical process.

Surprisingly, despite the varying extent of exact exchange and thus the static correlation, computed EAs and IEs are in an excellent qualitative agreement between all tested methods across model sizes (Fig.5.6). Functionals with less or no exact exchange tend to overestimate the EAs and underestimate the IEs, although these errors appear to be systematic. This suggests that the infamous error cancellation, to which the success of DFT is often attributed, is at play when computing the reaction energies of one-electron addition or removal, even in the case of complex electronic structures plagued by significant multi-reference character.

5.3.2 Structure-property relationships

Computing EAs and IEs from the vertical process alone saves computational time compared to the full adiabatic process, since no geometry relaxations are necessary for the product radical ions. This is an approximation neglecting the structure relaxation effects. To confirm the validity of this approximation, a comparison between results obtained in the vertical and in the adiabatic schemes was performed (see Fig.5.7). These results show that in the case of one-electron addition to or removal from the investigated graphene-based nanoflakes, structural variation in the product radical ions is minimal. This is not surprisingly considering the rigid structures of these species comprised of condensed conjugated rings. Therefore, for simplicity we discuss the vertical values below, but the same conclusions can be drawn based on the adiabatic computations.
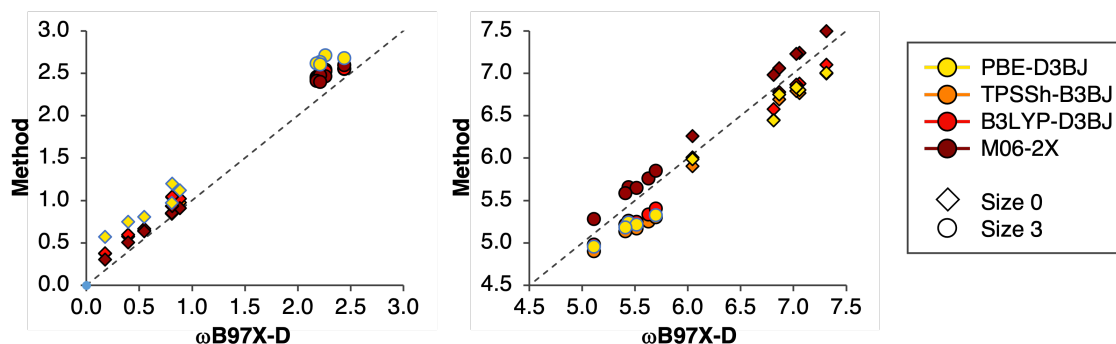
Figure 5.6: Vertical electronic affinities (left) and ionisation energies (right) for GBM model sizes 0 and 3, computed using various DFT functionals and plotted *versus* the ωB97X-D/def2-TZVP results. Dashed line represents the $x=y$ function.
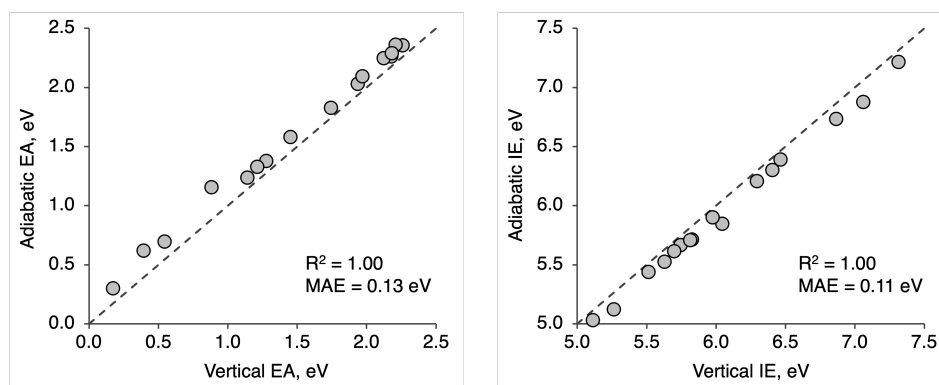
Figure 5.7: Comparison between vertical and adiabatic electron affinities (left) and ionisation energies (right), computed at the ωB97X-D/def2-TZVP level of theory across all model sizes. Dashed line represents the $x=y$ function.

The EA of a molecule is defined as the amount of energy released when an electron is added to it (see Equation (5.4)); high EA indicates that the molecule accepts an electron easily. Computed vertical EAs for investigated graphene nanoflakes (Fig. 5.8) show that increasing the size of the nanoflake leads to an increase in the EA. Better electron-accepting behaviour of larger systems arises from the greater delocalisation and thus stabilisation of the negative charge and unpaired spin.

Ionisation energy (also called ionisation potential, IP, in the past) is the energy required to remove an electron from a molecule (see Equation (5.3)), and lower IE values correspond to a stronger electron acceptor character. Our results for the graphene nanoflakes (Fig. 5.8) indicate that bigger molecules have smaller IEs. Similar to the EA values, the bigger the system, the easier it is to remove a single electron from it, since the resulting radical cation is more efficiently stabilised by electron delocalisation.

According to Koopmans theorem in the closed-shell Hartree–Fock formalism, the first IE of a molecule is exactly equal to the negative of the orbital energy of its highest occupied molecular orbital (HOMO) [207]. A parallel is often made to connect the first electron affinity to the energy of the lowest unoccupied molecular orbital (LUMO). Its analogue in DFT, Janak's theorem [208], states that similar relationships exist, although in practice large errors can often be observed depending on the functional used [209]. To probe these relationships, we compared vertical EA and IE values to the LUMO and HOMO energies, respectively (Fig. 5.9). For small model sizes, there is a clear linear relationship between EA or IE and the respective orbital energies. However, large static electron correlation in large model sizes is also reflected in poor (if any) correlations.

Comparing electronic properties of the studied GBMs, we note that doping and functionalisation generally improve both the electron-accepting (higher EAs) and electron-donating (lower IEs) ability compared to pristine graphene. However, considering the size dependence of these properties, we note that the chemical composition of the GBM does not have a strong effect on these
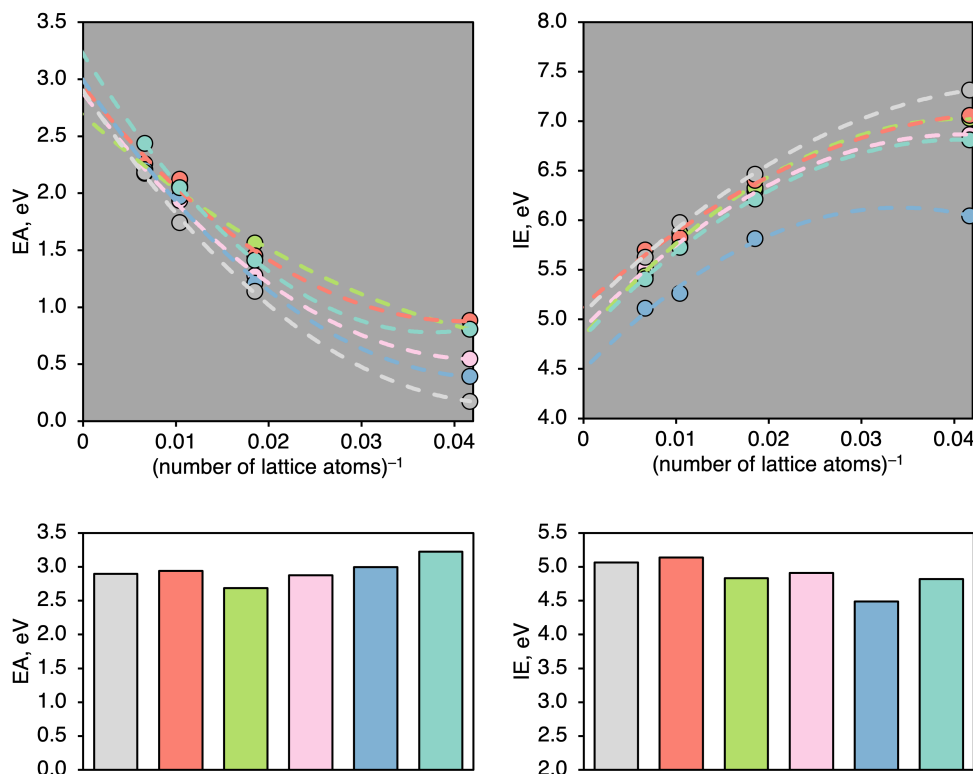
Figure 5.8: Top: Vertical electron affinities (left) and ionisation energies (right), computed at ωB97X-D/def2-TZVP level of theory for various GBMs as a function of the size of the nanoflake, expressed as the reciprocal to the number of non-hydrogen atoms contained in it. Dashed lines are 2nd order polynomial fits. Bottom: EA and IE values, extrapolated to the infinitely large material from the ωB97X-D/def2-TZVP computations on finite nanoflakes.

values, especially at larger model sizes (Fig. 5.8). Moreover, this dependence appears to be polynomial rather than linear with respect to the model size. This is particularly interesting considering that adsorption energies (see **Chapter 4**) instead follow a linear relationship with the model size and, most importantly, show a much greater variation depending on the chemistry of the material. These findings suggest that to boost the efficiency of graphene-based materials for sensing applications, a greater weight should be placed on the adsorbent properties, while reasonable electron shuffling can be expected with almost any doped graphene. This is reminiscent of the findings of the study by Pumera *et al.* fittingly titled "Will Any Crap We Put into Graphene Increase Its Electrocatalytic Effect?", in which doped GBM electrocatalysts performed much better than the pristine counterpart in the oxygen reduction and hydrogen evolution reactions independent on the dopant's chemical nature [16].

5.3.3 Solvent effects

Accurate redox potentials of molecules can be obtained *in silico via* thermodynamic cycles (Fig.5.10) [210]. Apart from accurate thermodynamic values for protons, electrons, and reference electrode, which can be found in the literature, the only other quantities required to evaluate the redox potentials are the EA (for reduction) or IE (for oxidation) and the corresponding solvent effects on these reaction energies. To estimate these solvent effects in water, we computed Gibbs free energies of solvation of the parent nanoflakes and their radical anions and cations, respectively, using the SMD solvent model at the ωB97X-D/def2-TZVP level of theory (see Table 5.4). We note that while most parent nanoflakes are either insoluble in water or their solvation is very slightly exergonic, products of their one-electron reduction or oxidation are charged, and are therefore associated with large negative free energies of solvation in a polar solvent (water). As a result, solvation in water further amplifies both the electron-donating and electron-withdrawing tendencies of the graphene nanoflakes. Comparing results for model sizes 0 and 1, we note that
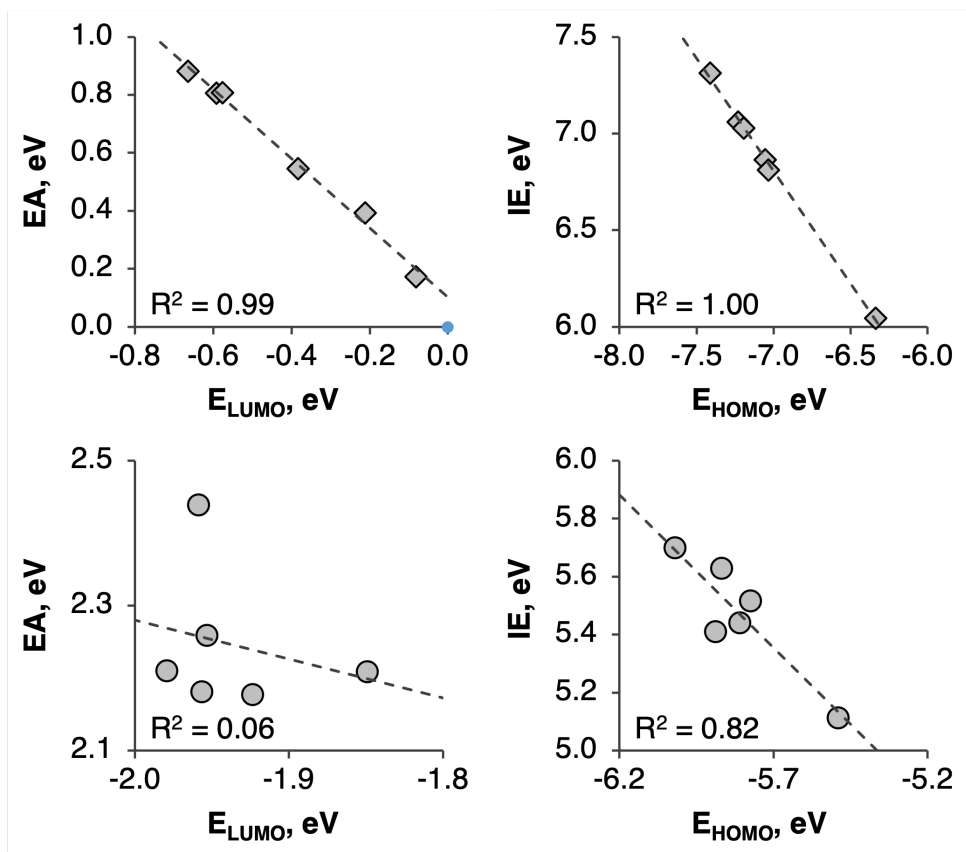
Figure 5.9: Left: vertical electron affinities plotted *versus* LUMO energies for model size 0 (diamonds) and 3 (circles). Right: vertical ionisation energies plotted *versus* HOMO energies for model size 0 (diamonds) and 3 (circles). Dashed lines are linear regression fits. All values were computed at the ωB97X-D/def2-TZVP level of theory.

the magnitude of these solvent effects decreases, which is consistent with the fact that larger polycyclic hydrocarbons are more hydrophobic.
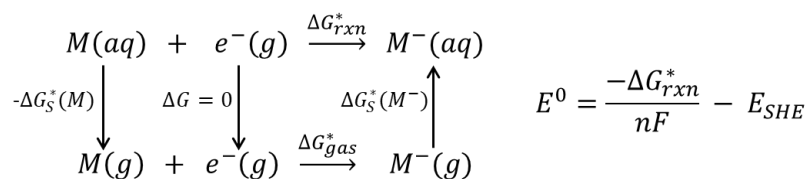
Figure 5.10: Thermodynamic cycle for computing the redox potential according to Ref.[210].

Finally, solvent effects on the oxidation and reduction are relatively similar for all studied GBMs (Fig. 5.11). Together with very similar gas-phase EA and IP values (Fig. 5.8), this suggests that doping and functionalisation do not result in significant variation of the redox properties of GBMs in water. This observation again contrasts with our results for interaction energies in **Chapter 4**, solvent effects on which were found to vary across a broader range depending on the chemical nature of the materials (Fig. 4.6).

Table 5.4: Free energies of solvation for neutral and reduced/oxidised GBMs, as well as the corresponding solvent corrections to EA and IE. All computations were performed in water at 298K at the SMD/ωB97x-D/def2-TZVP level of theory.

GBM	Size	$\Delta G_{solv, parent}$ [eV]	$\Delta G_{solv, anion}$ [eV][a]	$\Delta G_{solv, cation}$ [eV][a]	$\Delta\Delta G_{Red}$ [eV][b]	$\Delta\Delta G_{Ox}$ [eV][c]
pristine graphene	0	0.11	-1.36	-1.20	1.47	-1.30
	1	0.18	-0.99	-0.79	1.17	-0.97
epoxide rGO	0	0.06	-1.48	-1.26	1.55	-1.33
	1	0.13	-1.13	-0.85	1.26	-0.98
BH-doped graphene	0	0.11	-1.33	-1.25	1.44	-1.37
	1	0.10	-1.09	-0.91	1.18	-1.01
1,1-B,N-codoped graphene	0	0.12	-1.35	-1.20	1.47	-1.32
	1	0.20	-0.99	-0.78	1.20	-0.98
NH-doped graphene	0	0.00	-1.45	-1.49	1.45	-1.49
	1	0.04	-1.13	-1.07	1.17	-1.11
PH-doped graphene	0	-0.02	-1.47	-1.44	1.45	-1.42
	1	0.03	-1.16	-0.99	1.19	-1.02

[a] Referring to the radical anionic and cationic species.
[b] The reduction $\Delta\Delta G_{Red}$ corresponds to the solvent effect on the EA, as defined in Equation (5.4).
[c] The oxidation $\Delta\Delta G_{Ox}$ corresponds to the solvent effect on the IE, as defined in Equation (5.3).
All ΔG values were corrected for the phase change.
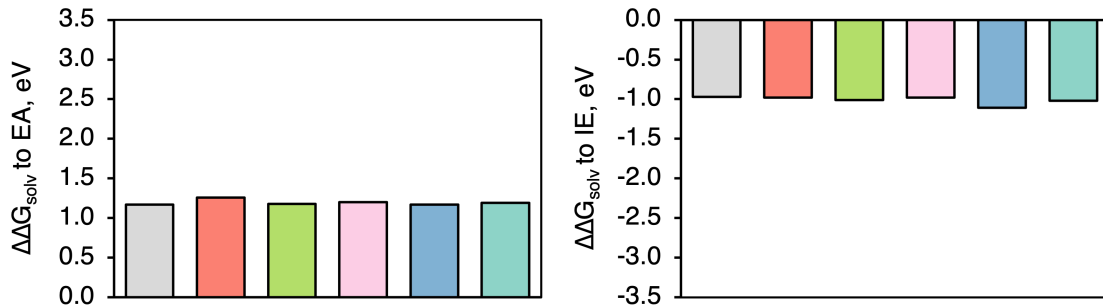
Figure 5.11: Solvent corrections to EA (left) and IE (right) for model size 1. All computations were performed in water at 298K at the SMD/ωB97X-D/def2-TZVP level of theory. The y-axis scale is set to the same range as that for computed EAs and IEs in Fig. 5.8, bottom panel.

5.4 Conclusions

In this Chapter, we explored how IE, EA, and solvation effects on the corresponding redox properties depend on the size and chemical composition of nanographenes. Large acenes and other extended polyaromatic hydrocarbons feature small singlet-triplets gaps and often have diradical ground states. To characterise the static electron correlation (spin contamination) associated with the multi-reference character of these systems, we employed the fractional occupation number weighted density and explored how the amount of Hartree-Fock exchange included in the chosen DFT functional influences resulting electronic properties. We found that despite the strong multi-reference character of the larger nanoflakes (model sizes 2 and 3), computed properties are hardly affected by the choice of the DFT functional, and even inexpensive PBE-D3BJ (lacking any exact exchange) produces EA and IE values in close qualitative agreement with the range-separated ωB97X-D. For pristine graphene, computed values are also in line with those reported in prior computational studies (Table 5.1). However, a definitive ruling on the quality of these predictions is impossible without either more experimental data or computations with multi-reference methods,

which, at present, are prohibitively expensive for larger nanoflakes.

In **Chapter 4**, we discovered the strong dependence of the interaction energies between GBMs and nitroaromatic molecules on the chemical nature of the material and the size of the nanoflake model. In contrast, computed electronic properties appear to be less dependent on the doping and functionalisation of graphene, and their variation with size is essentially constant across all studied chemistries. Increasing the size of the graphene nanoflakes makes the one-electron addition and removal easier, as the resulting radical anion or cation is increasingly more stabilised in larger conjugated systems. Furthermore, computed Gibbs free energies of solvation reveal that increasing the size of the graphene derivative increases its hydrophobic character, even for radical ions. Therefore, while solvation in water further facilitates the redox transformations, this effect decreases for larger nanoflakes.

Overall, in this Chapter we established that, unlike the adsorbent energetics, electronic (redox) properties of graphene-based materials show only little variation with the computational methodology, the size of the model, and the chemical composition of the material. On the one hand, these findings simplify the development of alternative electrochemical sensors and catalysts, since a material can be tailored toward other relevant properties without sacrificing its redox performance. On the other hand, there is seemingly little "wiggle room" for modulating the redox properties of graphene-based materials *via* chemical modification alone. This limitation presents an enticing challenge for future materials design.

Conclusions

Graphene-based materials are attracting growing attention as sustainable and efficient alternatives to inorganic systems in sensing, catalysis, among many other practical applications. The vast chemical space of graphene derivatives, stemming from endless functionalisation, doping, and defect engineering possibilities, together with the sizes - ranging from small nanoflakes to extended periodic sheets - cannot be mapped efficiently in an experimental setting. Exploring this space and selecting the best candidate materials for specific applications calls for structure-property-performance relationships to be established and applied in rational design. In this thesis, we set out to elucidate such relationships, focusing on the applications of GBMs in capture and transformation of environmental pollutants. We explored how their adsorbent properties, quantified *via* the energetics of the non-covalent interactions, and their ability to shuttle electrons in an electrochemical settings, reflected by the EAs and IEs, vary depending on the chemical composition and size of the material, as well as how these properties relate to the observed performance in practical uses. Crucially, our findings are relevant to applications far outside this particular scope, and can be applied to any scenario involving physisorption and reduction/oxidation of GBMs.

The unique chemical nature of graphene and its derivatives brings about an array of methodological challenges in simulating their properties. While computational chemistry and physics offer many sophisticated and insightful modelling tools and techniques, the gap between the accuracy of predictions and realism in representing investigated systems and processes remains unbridged even today. Specifically, highly accurate electronic structure theory approaches, such as multi-reference post-Hartree-Fock theory or DFT functionals from the upper rungs of the Jacob's ladder, are largely impractical for molecules containing more than several dozen atoms and are completely unavailable for extended materials. These large systems can instead be treated with classical or semiemppirical approaches and LDA and GGA DFT, although these lack precision in describing the electronic structure. This is particularly pressing in the case of extended polycyclic conjugated molecules and materials burdened with potentially strong static electron correlation. Therefore, a substantial part of this thesis was dedicated to benchmarking a broad spectrum of *in silico* approaches in an effort to identify reliable and affordable modelling protocols.

This task has proven to be non-trivial. We discovered that even for very simple systems, such as CO_2 interacting with benzene, computed interaction energies already deviate between the levels of theory. As we moved to large models of pristine graphene, the spread in the computed energetics broadened while the range of available methods shrank. We also observed unsettling discrepancies in the performance of computational methods when modelling interactions between GBMs and nitroaromatic compounds: semiempirical density functional tight-binding greatly overbinds these complexes but predicts interaction energies qualitatively similar to those obtained with SAPT, while the results of pure DFT are in disarray. On the other hand, the electronic (redox) properties of graphene-based nanoflakes showed little variation with the computational methodology, notwithstanding the complicated and potentially multi-reference electronic structure of these species. Despite these challenges, we were able to deduce methodological approaches to the adsorbent and redox properties that provided qualitative insights into how these properties depend on the material's structures.

We have discovered that properties of extended materials can be approximated *via* an extrapolation scheme, which relies on computations on finite, moderately-sized systems. These computations can in turn be performed with more accurate methods, and the obtained results can be rationalised by means of insightful energy and density decomposition analyses, largely unavailable for periodic computations. We found that while the adsorbent properties of the studied GBMs, both in the gas phase and in water, vary greatly depending on their doping, chemical functionalisation, and model size, their redox features remain essentially uniform across the explored structural and composi-

tional ranges. These findings not only pave the way toward rational application-guided materials design, but also pose several tantalising research questions:

- Can the discovered size-dependence of the adsorbent properties of GBMs on their chemistry be incorporated into size-selective practical applications, such as sorting of the quantum dots by sorbents?

- Why are the redox properties of the GBMs so insensitive to their composition? Could these properties be pushed outside the narrow range, observed in this thesis, by greater dopant loadings or more exotic functionalisations?

These questions undoubtedly warrant addressing in follow-up studies. Another target for future research is the expansion of the *in silico* models employed in this thesis toward realistic systems under real-life conditions. This entails incorporating structural defects, altering analyte loadings, applying external potentials, introducing support materials, including thermal corrections, and so on. In large part, methodological foundation for these investigations has already been established in this thesis. This foundation can equally be utilised in setting-up high-throughput screenings of many more GBMs and analytes. However, true validation of such computational studies can only come from experiment. Our research has clearly demonstrated that, at present, there is not enough consistent and homogeneous experimental data to conduct reliable and extensive methods benchmarks. Until this data is available, methodological protocols and structure-property relationships, established herein, serve to qualitatively guide the chemical design and exploratory testing of new graphene-based materials for catalysis and sensing.

List of Publications

Publications in the scope of this thesis:

- **CO$_2$ on Graphene: Benchmarking Computational Approaches to Noncovalent Interactions**
  Christopher Ehlert, Anna Piras, and Ganna Gryn'ova
  ACS Omega **2023**, *8*, 35768–35778.
  https://doi.org/10.1021/acsomega.3c03251

- **Sensing and Sensitivity: Computational Chemistry of Graphene-Based Sensors**
  Anna Piras, Christopher Ehlert, and Ganna Gryn'ova
  WIREs Computat. Mol. Sci., **2021**, *11*, e1526.
  https://doi.org/10.1002/wcms.1526

Other publications:

- **Metal-Free Molecular Catalysts for the Oxygen Reduction Reaction: Electron Affinity as an Activity Descriptor**
  Christopher Ehlert, Anna Piras, Juliette Schleicher, and Ganna Gryn'ova
  J. Phys. Chem. Lett. **2023**, *14*, 476–480.
  https://doi.org/10.1021/acs.jpclett.2c03481

Publications in preparation:

- **Adsorption of Nitroaromatic Contaminants on Graphene-Based Sensors: A Computational Study**
  Anna Piras and Ganna Gryn'ova

- **A Density Functional Theory Study on the Electronic Properties of Circular Graphene Quantum Dots**
  Anna Piras and Ganna Gryn'ova

Bibliography

[1] UN General Assembly. *Transforming our world : the 2030 Agenda for Sustainable Development,* tech. rep. A/RES/70/1. Oct. 2015. URL: https://sdgs.un.org/2030agenda.

[2] Greg Hughes and Jared C. Lewis. "Introduction: Biocatalysis in Industry". en. In: *Chemical Reviews* 118.1 (Jan. 2018), pp. 1–3. ISSN: 0009-2665, 1520-6890. DOI: 10.1021/acs.chemrev.7b00741. URL: https://pubs.acs.org/doi/10.1021/acs.chemrev.7b00741.

[3] Miles H. Aukland and Benjamin List. "Organocatalysis emerging as a technology". en. In: *Pure and Applied Chemistry* 93.12 (Dec. 2021), pp. 1371–1381. ISSN: 0033-4545, 1365-3075. DOI: 10.1515/pac-2021-0501. URL: https://www.degruyter.com/document/doi/10.1515/pac-2021-0501/html.

[4] Eric Keightley Rideal and Winifred Mary Wright. "CCXL.—Low temperature oxidation at charcoal surfaces. Part II. The behaviour of charcoal in the presence of promoters". en. In: *J. Chem. Soc.* 129.0 (1926), pp. 1813–1821. ISSN: 0368-1769. DOI: 10.1039/JR9262901813. URL: http://xlink.rsc.org/?DOI=JR9262901813.

[5] Sumio Iijima. "Helical microtubules of graphitic carbon". en. In: *Nature* 354.6348 (Nov. 1991), pp. 56–58. ISSN: 0028-0836, 1476-4687. DOI: 10.1038/354056a0. URL: https://www.nature.com/articles/354056a0 (visited on 12/12/2023).

[6] K. S. Novoselov et al. "Electric Field Effect in Atomically Thin Carbon Films". en. In: *Science* 306.5696 (Oct. 2004), pp. 666–669. ISSN: 0036-8075, 1095-9203. DOI: 10.1126/science.1102896. URL: https://www.science.org/doi/10.1126/science.1102896.

[7] Vasilios Georgakilas et al. "Functionalization of Graphene: Covalent and Non-Covalent Approaches, Derivatives and Applications". en. In: *Chemical Reviews* 112.11 (Nov. 2012), pp. 6156–6214. ISSN: 0009-2665, 1520-6890. DOI: 10.1021/cr3000412. URL: https://pubs.acs.org/doi/10.1021/cr3000412.

[8] Sami Ullah et al. "Advances and Trends in Chemically Doped Graphene". en. In: *Advanced Materials Interfaces* 7.24 (Dec. 2020), p. 2000999. ISSN: 2196-7350, 2196-7350. DOI: 10.1002/admi.202000999. URL: https://onlinelibrary.wiley.com/doi/10.1002/admi.202000999.

[9] Amelie Ferrand, Mohamed Siaj, and Jerome P. Claverie. "Graphene, the Swiss Army Knife of Nanomaterials Science". en. In: *ACS Applied Nano Materials* 3.8 (Aug. 2020), pp. 7305–7313. ISSN: 2574-0970, 2574-0970. DOI: 10.1021/acsanm.0c02055. URL: https://pubs.acs.org/doi/10.1021/acsanm.0c02055.

[10] Chengzhou Zhu et al. "Reducing Sugar: New Functional Molecules for the Green Synthesis of Graphene Nanosheets". en. In: *ACS Nano* 4.4 (Apr. 2010), pp. 2429–2437. ISSN: 1936-0851, 1936-086X. DOI: 10.1021/nn1002387. URL: https://pubs.acs.org/doi/10.1021/nn1002387.

[11] William S. Hummers and Richard E. Offeman. "Preparation of Graphitic Oxide". en. In: *Journal of the American Chemical Society* 80.6 (Mar. 1958), pp. 1339–1339. ISSN: 0002-7863, 1520-5126. DOI: 10.1021/ja01539a017. URL: https://pubs.acs.org/doi/abs/10.1021/ja01539a017.

[12] L. Staudenmaier. "Verfahren zur Darstellung der Graphitsäure". en. In: *Berichte der deutschen chemischen Gesellschaft* 31.2 (May 1898), pp. 1481–1487. ISSN: 0365-9496. DOI: 10.1002/cber.18980310237. URL: https://chemistry-europe.onlinelibrary.wiley.com/doi/10.1002/cber.18980310237.

[13] Benjamin C. Brodie. "XIII. On the atomic weight of graphite". en. In: *Philosophical Trans-actions of the Royal Society of London* 149 (Dec. 1859), pp. 249–259. ISSN: 0261-0523, 2053-9223. DOI: `10.1098/rstl.1859.0013`. URL: `https://royalsocietypublishing.org/doi/10.1098/rstl.1859.0013`.

[14] Anton Lerf et al. "Structure of Graphite Oxide Revisited". en. In: *The Journal of Physical Chemistry B* 102.23 (June 1998), pp. 4477–4482. ISSN: 1520-6106, 1520-5207. DOI: `10.1021/jp9731821`. URL: `https://pubs.acs.org/doi/10.1021/jp9731821`.

[15] Hoik Lee, Keewook Paeng, and Ick Soo Kim. "A review of doping modulation in graphene". en. In: *Synthetic Metals* 244 (Oct. 2018), pp. 36–47. ISSN: 03796779. DOI: `10.1016/j.synthmet.2018.07.001`. URL: `https://linkinghub.elsevier.com/retrieve/pii/S0379677918301668` (visited on 12/12/2023).

[16] Lu Wang, Zdenek Sofer, and Martin Pumera. "Will Any Crap We Put into Graphene Increase Its Electrocatalytic Effect?" en. In: *ACS Nano* 14.1 (Jan. 2020), pp. 21–25. ISSN: 1936-0851, 1936-086X. DOI: `10.1021/acsnano.9b00184`. URL: `https://pubs.acs.org/doi/10.1021/acsnano.9b00184`.

[17] Jacqueline Allan et al. "Regulatory landscape of nanotechnology and nanoplastics from a global perspective". en. In: *Regulatory Toxicology and Pharmacology* 122 (June 2021), p. 104885. ISSN: 02732300. DOI: `10.1016/j.yrtph.2021.104885`. URL: `https://linkinghub.elsevier.com/retrieve/pii/S0273230021000258`.

[18] Charles A. Clifford et al. "The importance of international standards for the graphene community". en. In: *Nature Reviews Physics* 3.4 (Mar. 2021), pp. 233–235. ISSN: 2522-5820. DOI: `10.1038/s42254-021-00278-6`. URL: `https://www.nature.com/articles/s42254-021-00278-6`.

[19] Martin Pykal et al. "Modelling of graphene functionalization". en. In: *Physical Chemistry Chemical Physics* 18.9 (2016), pp. 6351–6372. ISSN: 1463-9076, 1463-9084. DOI: `10.1039/C5CP03599F`. URL: `http://xlink.rsc.org/?DOI=C5CP03599F`.

[20] Kasra Momeni et al. "Multiscale computational understanding and growth of 2D materials: a review". en. In: *npj Computational Materials* 6.1 (Mar. 2020), p. 22. ISSN: 2057-3960. DOI: `10.1038/s41524-020-0280-2`. URL: `https://www.nature.com/articles/s41524-020-0280-2`.

[21] Anna Piras, Christopher Ehlert, and Ganna Gryn'ova. "Sensing and sensitivity: Computational chemistry of ¡span style="font-variant:small-caps;"¿graphene-based¡/span¿ sensors". en. In: *WIREs Computational Molecular Science* 11.5 (Sept. 2021), e1526. ISSN: 1759-0876, 1759-0884. DOI: `10.1002/wcms.1526`. URL: `https://wires.onlinelibrary.wiley.com/doi/10.1002/wcms.1526`.

[22] Lan Zhang et al. "A molecular dynamics simulation of the graphene growth on Cu(1 1 1) sur-face". en. In: *Computational Materials Science* 130 (Apr. 2017), pp. 10–15. ISSN: 09270256. DOI: `10.1016/j.commatsci.2016.12.043`. URL: `https://linkinghub.elsevier.com/retrieve/pii/S0927025617300058`.

[23] Ziwei Xu et al. "Molecular dynamics simulation of graphene sinking during chemical vapor deposition growth on semi-molten Cu substrate". en. In: *npj Computational Materials* 6.1 (Mar. 2020), p. 14. ISSN: 2057-3960. DOI: `10.1038/s41524-020-0281-1`. URL: `https://www.nature.com/articles/s41524-020-0281-1`.

[24] Satoru Kaneko et al. "Carbon clusters on substrate surface for graphene growth- theoretical and experimental approach". en. In: *Scientific Reports* 12.1 (Sept. 2022), p. 15809. ISSN: 2045-2322. DOI: `10.1038/s41598-022-20078-x`. URL: `https://www.nature.com/articles/s41598-022-20078-x`.

[25] Zongyang Qiu et al. "Atomistic Simulations of Graphene Growth: From Kinetics to Mech-anism". en. In: *Accounts of Chemical Research* 51.3 (Mar. 2018), pp. 728–735. ISSN: 0001-4842, 1520-4898. DOI: `10.1021/acs.accounts.7b00592`. URL: `https://pubs.acs.org/doi/10.1021/acs.accounts.7b00592`.

[26] Zhi Yang et al. "Pyrolysis mechanisms of graphene oxide revealed by ReaxFF molecular dynamics simulation". en. In: *Applied Surface Science* 509 (Apr. 2020), p. 145247. ISSN: 01694332. DOI: `10.1016/j.apsusc.2020.145247`. URL: `https://linkinghub.elsevier.com/retrieve/pii/S0169433220300039`.

[27] Chu Chen et al. "Theoretical simulation of reduction mechanism of graphene oxide in sodium hydroxide solution". en. In: *Physical Chemistry Chemical Physics* 16.25 (2014), p. 12858. ISSN: 1463-9076, 1463-9084. DOI: `10.1039/c4cp01031k`. URL: `http://xlink.rsc.org/?DOI=c4cp01031k`.

[28] Robert C. Sinclair and Peter V. Coveney. "Modeling Nanostructure in Graphene Oxide: Inhomogeneity and the Percolation Threshold". en. In: *Journal of Chemical Information and Modeling* 59.6 (June 2019), pp. 2741–2745. ISSN: 1549-9596, 1549-960X. DOI: `10.1021/acs.jcim.9b00114`. URL: `https://pubs.acs.org/doi/10.1021/acs.jcim.9b00114`.

[29] Benyamin Motevalli et al. "The representative structure of graphene oxide nanoflakes from machine learning". In: *Nano Futures* 3.4 (Dec. 2019), p. 045001. ISSN: 2399-1984. DOI: `10.1088/2399-1984/ab58ac`. URL: `https://iopscience.iop.org/article/10.1088/2399-1984/ab58ac` (visited on 12/15/2023).

[30] Natalya A Garcia et al. "Simulation-ready graphene oxide structures with hierarchical complexity: a modular tiling strategy". In: *2D Materials* 10.2 (Apr. 2023), p. 025007. ISSN: 2053-1583. DOI: `10.1088/2053-1583/acb0e1`. URL: `https://iopscience.iop.org/article/10.1088/2053-1583/acb0e1`.

[31] Sebastian Muraru, Jorge S. Burns, and Mariana Ionita. "GOPY: A tool for building 2D graphene-based computational models". en. In: *SoftwareX* 12 (July 2020), p. 100586. ISSN: 23527110. DOI: `10.1016/j.softx.2020.100586`. URL: `https://linkinghub.elsevier.com/retrieve/pii/S2352711020302995`.

[32] Zak E. Hughes and Tiffany R. Walsh. "Computational chemistry for graphene-based energy applications: progress and challenges". en. In: *Nanoscale* 7.16 (2015), pp. 6883–6908. ISSN: 2040-3364, 2040-3372. DOI: `10.1039/C5NR00690B`. URL: `http://xlink.rsc.org/?DOI=C5NR00690B`.

[33] Aijun Du. "*In silico* engineering of graphene-based van der Waals heterostructured nanohybrids for electronics and energy applications". en. In: *WIREs Computational Molecular Science* 6.5 (Sept. 2016), pp. 551–570. ISSN: 1759-0876, 1759-0884. DOI: `10.1002/wcms.1266`. URL: `https://wires.onlinelibrary.wiley.com/doi/10.1002/wcms.1266` (visited on 12/15/2023).

[34] Christopher D. Williams, Paola Carbone, and Flor R. Siperstein. "*In Silico* Design and Characterization of Graphene Oxide Membranes with Variable Water Content and Flake Oxygen Content". en. In: *ACS Nano* 13.3 (Mar. 2019), pp. 2995–3004. ISSN: 1936-0851, 1936-086X. DOI: `10.1021/acsnano.8b07573`. URL: `https://pubs.acs.org/doi/10.1021/acsnano.8b07573`.

[35] Honglei Wang et al. "*In silico* design of dual-doped nitrogenated graphene (C_2N) employed in electrocatalytic reduction of carbon monoxide to ethylene". en. In: *Journal of Materials Chemistry A* 10.9 (2022), pp. 4703–4710. ISSN: 2050-7488, 2050-7496. DOI: `10.1039/D1TA09847K`. URL: `http://xlink.rsc.org/?DOI=D1TA09847K`.

[36] Na Guo, Kah Meng Yam, and Chun Zhang. "Substrate engineering of graphene reactivity: towards high-performance graphene-based catalysts". en. In: *npj 2D Materials and Applications* 2.1 (Jan. 2018), p. 1. ISSN: 2397-7132. DOI: `10.1038/s41699-017-0046-y`. URL: `https://www.nature.com/articles/s41699-017-0046-y`.

[37] Luca Bonatti et al. "*In silico* design of graphene plasmonic hot-spots". en. In: *Nanoscale Advances* 4.10 (2022), pp. 2294–2302. ISSN: 2516-0230. DOI: `10.1039/D2NA00088A`. URL: `http://xlink.rsc.org/?DOI=D2NA00088A`.

[38] Steven E. Wheeler et al. "Noncovalent Interactions in Organocatalysis and the Prospect of Computational Catalyst Design". en. In: *Accounts of Chemical Research* 49.5 (May 2016), pp. 1061–1069. ISSN: 0001-4842, 1520-4898. DOI: `10.1021/acs.accounts.6b00096`. URL: `https://pubs.acs.org/doi/10.1021/acs.accounts.6b00096`.

[39] Kamran T. Mahmudov and Armando J. L. Pombeiro. "Control of Selectivity in Homogeneous Catalysis through Noncovalent Interactions". en. In: *Chemistry – A European Journal* 29.26 (May 2023), e202203861. ISSN: 0947-6539, 1521-3765. DOI: `10.1002/chem.202203861`. URL: `https://chemistry-europe.onlinelibrary.wiley.com/doi/10.1002/chem.202203861`.

[40] Victor Gold, ed. *The IUPAC Compendium of Chemical Terminology: The Gold Book*. en. 4th ed. Research Triangle Park, NC: International Union of Pure and Applied Chemistry (IUPAC), 2019. DOI: 10.1351/goldbook. URL: https://goldbook.iupac.org/ (visited on 01/24/2024).

[41] Ewa Pastorczak and Clémence Corminboeuf. "Perspective: Found in translation: Quantum chemical tools for grasping non-covalent interactions". en. In: *The Journal of Chemical Physics* 146.12 (Mar. 2017), p. 120901. ISSN: 0021-9606, 1089-7690. DOI: 10.1063/1.4978951. URL: https://pubs.aip.org/jcp/article/146/12/120901/636348/Perspective-Found-in-translation-Quantum-chemical.

[42] Laith A. Algharagholy et al. "Discriminating sensing of explosive molecules using graphene–boron nitride–graphene heteronanosheets". en. In: *RSC Advances* 12.54 (2022), pp. 35151–35157. ISSN: 2046-2069. DOI: 10.1039/D2RA06125B. URL: http://xlink.rsc.org/?DOI=D2RA06125B (visited on 12/01/2023).

[43] Mandeep, Lekha Sharma, and Rita Kakkar. "DFT study on the adsorption of p-nitrophenol over vacancy and Pt-doped graphene sheets". en. In: *Computational and Theoretical Chemistry* 1142 (Oct. 2018), pp. 88–96. ISSN: 2210271X. DOI: 10.1016/j.comptc.2018.08.020. URL: https://linkinghub.elsevier.com/retrieve/pii/S2210271X18304936 (visited on 12/01/2023).

[44] Xin-Ran Zhang, Jian-Gang Guo, and Li-Jun Zhou. "Experimental and theoretical investigation on the adsorption properties of benzene on graphene surface: Influence of pH and edge effects". en. In: *Chemical Engineering Journal* 440 (July 2022), p. 135794. ISSN: 13858947. DOI: 10.1016/j.cej.2022.135794. URL: https://linkinghub.elsevier.com/retrieve/pii/S1385894722012943 (visited on 12/01/2023).

[45] Zakir Ullah et al. "Adsorption of Pyrimidin-2-amine (PA) on Graphene Quantum Dots (GQDs): Non-covalent Interaction Study". en. In: *Journal of Molecular Liquids* 368 (Dec. 2022), p. 120654. ISSN: 01677322. DOI: 10.1016/j.molliq.2022.120654. URL: https://linkinghub.elsevier.com/retrieve/pii/S0167732222021936 (visited on 12/01/2023).

[46] V.S. Anithaa et al. "Adsorption of volatile organic compounds on pristine and defected nanographene". en. In: *Computational and Theoretical Chemistry* 1211 (May 2022), p. 113664. ISSN: 2210271X. DOI: 10.1016/j.comptc.2022.113664. URL: https://linkinghub.elsevier.com/retrieve/pii/S2210271X22000779 (visited on 12/01/2023).

[47] Amir Karton. "π–π interactions between benzene and graphene by means of large-scale DFT-D4 calculations". en. In: *Chemical Physics* 561 (Sept. 2022), p. 111606. ISSN: 03010104. DOI: 10.1016/j.chemphys.2022.111606. URL: https://linkinghub.elsevier.com/retrieve/pii/S0301010422001616.

[48] Petr Lazar et al. "Adsorption of Small Organic Molecules on Graphene". en. In: *Journal of the American Chemical Society* 135.16 (Apr. 2013), pp. 6372–6377. ISSN: 0002-7863, 1520-5126. DOI: 10.1021/ja403162r. URL: https://pubs.acs.org/doi/10.1021/ja403162r.

[49] Dan Wang et al. "Computational prediction for oxidation and reduction potentials of organic molecules used in organic light-emitting diodes". en. In: *Organic Electronics* 64 (Jan. 2019), pp. 216–222. ISSN: 15661199. DOI: 10.1016/j.orgel.2018.10.038. URL: https://linkinghub.elsevier.com/retrieve/pii/S1566119918305536.

[50] Rocco Peter Fornari and Piotr De Silva. "Molecular modeling of organic redox-active battery materials". en. In: *WIREs Computational Molecular Science* 11.2 (Mar. 2021), e1495. ISSN: 1759-0876, 1759-0884. DOI: 10.1002/wcms.1495. URL: https://wires.onlinelibrary.wiley.com/doi/10.1002/wcms.1495.

[51] G. Malloci, C. Joblin, and G. Mulas. "Theoretical evaluation of PAH dication properties". In: *Astronomy & Astrophysics* 462.2 (Feb. 2007), pp. 627–635. ISSN: 0004-6361, 1432-0746. DOI: 10.1051/0004-6361:20066053. URL: http://www.aanda.org/10.1051/0004-6361:20066053.

[52] Chia-Nan Yeh et al. "Electronic properties of the coronene series from thermally-assisted-occupation density functional theory". en. In: *RSC Advances* 8.60 (2018), pp. 34350–34358. ISSN: 2046-2069. DOI: 10.1039/C8RA01336E. URL: http://xlink.rsc.org/?DOI=C8RA01336E.

[53] Qing Deng and Jeng-Da Chai. "Electronic Properties of Triangle-Shaped Graphene Nanoflakes from TAO-DFT". en. In: *ACS Omega* 4.10 (Sept. 2019), pp. 14202–14210. ISSN: 2470-1343, 2470-1343. DOI: 10.1021/acsomega.9b01259. URL: https://pubs.acs.org/doi/10.1021/acsomega.9b01259.

[54] Cesar Gabriel Vera de la Garza et al. "Electronic structure of isomeric graphene nanoflakes". en. In: *Computational and Theoretical Chemistry* 1140 (Sept. 2018), pp. 125–133. ISSN: 2210271X. DOI: 10.1016/j.comptc.2018.08.007. URL: https://linkinghub.elsevier.com/retrieve/pii/S2210271X1830416X.

[55] Anthony P. Davis and Albert J. Fry. "Experimental and Computed Absolute Redox Potentials of Polycyclic Aromatic Hydrocarbons are Highly Linearly Correlated Over a Wide Range of Structures and Potentials". en. In: *The Journal of Physical Chemistry A* 114.46 (Nov. 2010), pp. 12299–12304. ISSN: 1089-5639, 1520-5215. DOI: 10.1021/jp106088n. URL: https://pubs.acs.org/doi/10.1021/jp106088n.

[56] Jiawen Zhang et al. "Unraveling the molecular interaction mechanism between graphene oxide and aromatic organic compounds with implications on wastewater treatment". en. In: *Chemical Engineering Journal* 358 (Feb. 2019), pp. 842–849. ISSN: 13858947. DOI: 10.1016/j.cej.2018.10.064. URL: https://linkinghub.elsevier.com/retrieve/pii/S1385894718320047.

[57] Jin Zhang et al. "Comparison of Implicit and Explicit Solvent Models for the Calculation of Solvation Free Energy in Organic Solvents". en. In: *Journal of Chemical Theory and Computation* 13.3 (Mar. 2017), pp. 1034–1043. ISSN: 1549-9618, 1549-9626. DOI: 10.1021/acs.jctc.7b00169. URL: https://pubs.acs.org/doi/10.1021/acs.jctc.7b00169.

[58] Trygve Helgaker, Poul Jørgensen, and Jeppe Olsen. *Molecular electronic-structure theory*. Chichester ; New York: Wiley, 2000. ISBN: 9780471967552 9781118531471.

[59] Dimitrios G. Liakos, Yang Guo, and Frank Neese. "Comprehensive Benchmark Results for the Domain Based Local Pair Natural Orbital Coupled Cluster Method (DLPNO-CCSD(T)) for Closed- and Open-Shell Systems". en. In: *The Journal of Physical Chemistry A* 124.1 (Jan. 2020), pp. 90–100. ISSN: 1089-5639, 1520-5215. DOI: 10.1021/acs.jpca.9b05734. URL: https://pubs.acs.org/doi/10.1021/acs.jpca.9b05734.

[60] Krzysztof Szalewicz. "Symmetry-adapted perturbation theory of intermolecular forces". en. In: *WIREs Computational Molecular Science* 2.2 (Mar. 2012), pp. 254–272. ISSN: 1759-0876, 1759-0884. DOI: 10.1002/wcms.86. URL: https://wires.onlinelibrary.wiley.com/doi/10.1002/wcms.86 (visited on 12/06/2023).

[61] John P. Perdew. "Jacob's ladder of density functional approximations for the exchange-correlation energy". en. In: *AIP Conference Proceedings*. Vol. 577. Antwerp (Belgium): AIP, 2001, pp. 1–20. DOI: 10.1063/1.1390175. URL: https://pubs.aip.org/aip/acp/article/577/1/1-20/573973.

[62] Yasmine S. Al-Hamdani and Alexandre Tkatchenko. "Understanding non-covalent interactions in larger molecular complexes from first principles". en. In: *The Journal of Chemical Physics* 150.1 (Jan. 2019), p. 010901. ISSN: 0021-9606, 1089-7690. DOI: 10.1063/1.5075487. URL: https://pubs.aip.org/jcp/article/150/1/010901/152312/Understanding-non-covalent-interactions-in-larger.

[63] Stefan Grimme et al. "A consistent and accurate *ab initio* parametrization of density functional dispersion correction (DFT-D) for the 94 elements H-Pu". en. In: *The Journal of Chemical Physics* 132.15 (Apr. 2010), p. 154104. ISSN: 0021-9606, 1089-7690. DOI: 10.1063/1.3382344. URL: https://pubs.aip.org/jcp/article/132/15/154104/926936/A-consistent-and-accurate-ab-initio.

[64] Christoph Bannwarth, Sebastian Ehlert, and Stefan Grimme. "GFN2-xTB—An Accurate and Broadly Parametrized Self-Consistent Tight-Binding Quantum Chemical Method with Multipole Electrostatics and Density-Dependent Dispersion Contributions". en. In: *Journal of Chemical Theory and Computation* 15.3 (Mar. 2019), pp. 1652–1671. ISSN: 1549-9618, 1549-9626. DOI: 10.1021/acs.jctc.8b01176. URL: https://pubs.acs.org/doi/10.1021/acs.jctc.8b01176.

[65]   Florian Weigend and Reinhart Ahlrichs. "Balanced basis sets of split valence, triple zeta valence and quadruple zeta valence quality for H to Rn: Design and assessment of accuracy". en. In: *Physical Chemistry Chemical Physics* 7.18 (2005), p. 3297. ISSN: 1463-9076, 1463-9084. DOI: 10.1039/b508541a. URL: http://xlink.rsc.org/?DOI=b508541a (visited on 12/07/2023).

[66]   Trent M. Parker et al. "Levels of symmetry adapted perturbation theory (SAPT). I. Efficiency and performance for interaction energies". en. In: *The Journal of Chemical Physics* 140.9 (Mar. 2014), p. 094106. ISSN: 0021-9606, 1089-7690. DOI: 10.1063/1.4867135. URL: https://pubs.aip.org/jcp/article/140/9/094106/193599/Levels-of-symmetry-adapted-perturbation-theory (visited on 12/08/2023).

[67]   Thom H. Dunning. "Gaussian basis sets for use in correlated molecular calculations. I. The atoms boron through neon and hydrogen". en. In: *The Journal of Chemical Physics* 90.2 (Jan. 1989), pp. 1007–1023. ISSN: 0021-9606, 1089-7690. DOI: 10.1063/1.456153. URL: https://pubs.aip.org/jcp/article/90/2/1007/91329/Gaussian-basis-sets-for-use-in-correlated.

[68]   Ewa Papajak et al. "Perspectives on Basis Sets Beautiful: Seasonal Plantings of Diffuse Basis Functions". en. In: *Journal of Chemical Theory and Computation* 7.10 (Oct. 2011), pp. 3027–3034. ISSN: 1549-9618, 1549-9626. DOI: 10.1021/ct200106a. URL: https://pubs.acs.org/doi/10.1021/ct200106a.

[69]   Stefan Grimme. "Exploration of Chemical Compound, Conformer, and Reaction Space with Meta-Dynamics Simulations Based on Tight-Binding Quantum Chemical Calculations". en. In: *Journal of Chemical Theory and Computation* 15.5 (May 2019), pp. 2847–2862. ISSN: 1549-9618, 1549-9626. DOI: 10.1021/acs.jctc.9b00143. URL: https://pubs.acs.org/doi/10.1021/acs.jctc.9b00143 (visited on 12/08/2023).

[70]   Steve Scheiner. "Understanding noncovalent bonds and their controlling forces". en. In: *The Journal of Chemical Physics* 153.14 (Oct. 2020), p. 140901. ISSN: 0021-9606, 1089-7690. DOI: 10.1063/5.0026168. URL: https://pubs.aip.org/jcp/article/153/14/140901/316619/Understanding-noncovalent-bonds-and-their.

[71]   Kazuo Kitaura and Keiji Morokuma. "A new energy decomposition scheme for molecular interactions within the Hartree-Fock approximation". en. In: *International Journal of Quantum Chemistry* 10.2 (Mar. 1976), pp. 325–340. ISSN: 0020-7608, 1097-461X. DOI: 10.1002/qua.560100211. URL: https://onlinelibrary.wiley.com/doi/10.1002/qua.560100211.

[72]   Bogumil Jeziorski, Robert Moszynski, and Krzysztof Szalewicz. "Perturbation Theory Approach to Intermolecular Potential Energy Surfaces of van der Waals Complexes". en. In: *Chemical Reviews* 94.7 (Nov. 1994), pp. 1887–1930. ISSN: 0009-2665, 1520-6890. DOI: 10.1021/cr00031a008. URL: https://pubs.acs.org/doi/abs/10.1021/cr00031a008.

[73]   Erin R. Johnson et al. "Revealing Noncovalent Interactions". en. In: *Journal of the American Chemical Society* 132.18 (May 2010), pp. 6498–6506. ISSN: 0002-7863, 1520-5126. DOI: 10.1021/ja100936w. URL: https://pubs.acs.org/doi/10.1021/ja100936w.

[74]   Richard F. W. Bader. "A quantum theory of molecular structure and its applications". en. In: *Chemical Reviews* 91.5 (July 1991), pp. 893–928. ISSN: 0009-2665, 1520-6890. DOI: 10.1021/cr00005a013. URL: https://pubs.acs.org/doi/abs/10.1021/cr00005a013.

[75]   Piotr De Silva and Clémence Corminboeuf. "Simultaneous Visualization of Covalent and Noncovalent Interactions Using Regions of Density Overlap". en. In: *Journal of Chemical Theory and Computation* 10.9 (Sept. 2014), pp. 3745–3756. ISSN: 1549-9618, 1549-9626. DOI: 10.1021/ct500490b. URL: https://pubs.acs.org/doi/10.1021/ct500490b.

[76]   S. Miertuš, E. Scrocco, and J. Tomasi. "Electrostatic interaction of a solute with a continuum. A direct utilizaion of AB initio molecular potentials for the prevision of solvent effects". en. In: *Chemical Physics* 55.1 (Feb. 1981), pp. 117–129. ISSN: 03010104. DOI: 10.1016/0301-0104(81)85090-2. URL: https://linkinghub.elsevier.com/retrieve/pii/0301010481850902.

[77] Benedetta Mennucci and Roberto Cammi, eds. *Continuum Solvation Models in Chemical Physics: From Theory to Applications*. en. 1st ed. Wiley, Nov. 2007. ISBN: 9780470029381 9780470515235. DOI: 10.1002/9780470515235. URL: https://onlinelibrary.wiley.com/doi/book/10.1002/9780470515235.

[78] A. Klamt and G. Schüürmann. "COSMO: a new approach to dielectric screening in solvents with explicit expressions for the screening energy and its gradient". en. In: *J. Chem. Soc., Perkin Trans. 2* 5 (1993), pp. 799–805. ISSN: 0300-9580, 1364-5471. DOI: 10.1039/P29930000799. URL: http://xlink.rsc.org/?DOI=P29930000799.

[79] Aleksandr V. Marenich, Christopher J. Cramer, and Donald G. Truhlar. "Universal Solvation Model Based on Solute Electron Density and on a Continuum Model of the Solvent Defined by the Bulk Dielectric Constant and Atomic Surface Tensions". en. In: *The Journal of Physical Chemistry B* 113.18 (May 2009), pp. 6378–6396. ISSN: 1520-6106, 1520-5207. DOI: 10.1021/jp810292n. URL: https://pubs.acs.org/doi/10.1021/jp810292n.

[80] Cosimo Anichini et al. "Chemical sensing with 2D materials". en. In: *Chemical Society Reviews* 47.13 (2018), pp. 4860–4908. ISSN: 0306-0012, 1460-4744. DOI: 10.1039/C8CS00417J. URL: http://xlink.rsc.org/?DOI=C8CS00417J.

[81] E. J. Jelmy et al. "Impact of structure, doping and defect-engineering in 2D materials on CO_2 capture and conversion". en. In: *Reaction Chemistry & Engineering* 6.10 (2021), pp. 1701–1738. ISSN: 2058-9883. DOI: 10.1039/D1RE00214G. URL: http://xlink.rsc.org/?DOI=D1RE00214G.

[82] Rajesh Das, Vaibhav Parihar, and C. M. Nagaraja. "Strategic design of a bifunctional Ag(¡span style="font-variant:small-caps;"¿i¡/span¿)-grafted NHC-MOF for efficient chemical fixation of CO_2 from a dilute gas under ambient conditions". en. In: *Inorganic Chemistry Frontiers* 9.11 (2022), pp. 2583–2593. ISSN: 2052-1553. DOI: 10.1039/D2QI00479H. URL: http://xlink.rsc.org/?DOI=D2QI00479H.

[83] Huilong Liu and Shubhra Bansal. "Metal halide perovskite nanostructures and quantum dots for photocatalytic CO2 reduction: prospects and challenges". en. In: *Materials Today Energy* 32 (Mar. 2023), p. 101230. ISSN: 24686069. DOI: 10.1016/j.mtener.2022.101230. URL: https://linkinghub.elsevier.com/retrieve/pii/S246860692200288X.

[84] Anderson D. Smith et al. "Graphene-based CO_2 sensing and its cross-sensitivity with humidity". en. In: *RSC Advances* 7.36 (2017), pp. 22329–22339. ISSN: 2046-2069. DOI: 10.1039/C7RA02821K. URL: http://xlink.rsc.org/?DOI=C7RA02821K.

[85] Yotsarayuth Seekaew and Chatchawal Wongchoosuk. "A novel graphene-based electroluminescent gas sensor for carbon dioxide detection". en. In: *Applied Surface Science* 479 (June 2019), pp. 525–531. ISSN: 01694332. DOI: 10.1016/j.apsusc.2019.02.100. URL: https://linkinghub.elsevier.com/retrieve/pii/S0169433219304441.

[86] Ganhua Lu, Leonidas E Ocola, and Junhong Chen. "Reduced graphene oxide for room-temperature gas sensors". In: *Nanotechnology* 20.44 (Nov. 2009), p. 445502. ISSN: 0957-4484, 1361-6528. DOI: 10.1088/0957-4484/20/44/445502. URL: https://iopscience.iop.org/article/10.1088/0957-4484/20/44/445502.

[87] K. R. Nemade and S. A. Waghuley. "Chemiresistive Gas Sensing by Few-Layered Graphene". en. In: *Journal of Electronic Materials* 42.10 (Oct. 2013), pp. 2857–2866. ISSN: 0361-5235, 1543-186X. DOI: 10.1007/s11664-013-2699-4. URL: http://link.springer.com/10.1007/s11664-013-2699-4 (visited on 12/19/2023).

[88] Hyeun Joong Yoon et al. "Carbon dioxide gas sensor using a graphene sheet". en. In: *Sensors and Actuators B: Chemical* 157.1 (Sept. 2011), pp. 310–313. ISSN: 09254005. DOI: 10.1016/j.snb.2011.03.035. URL: https://linkinghub.elsevier.com/retrieve/pii/S0925400511002310 (visited on 12/19/2023).

[89] Ashish Kumar Mishra and Sundara Ramaprabhu. "Carbon dioxide adsorption in graphene sheets". en. In: *AIP Advances* 1.3 (Sept. 2011), p. 032152. ISSN: 2158-3226. DOI: 10.1063/1.3638178. URL: https://pubs.aip.org/adv/article/1/3/032152/19886/Carbon-dioxide-adsorption-in-graphene-sheets.

[90] Rajasekhar Balasubramanian and Shamik Chowdhury. "Recent advances and progress in the development of graphene-based adsorbents for CO_2 capture". en. In: *Journal of Materials Chemistry A* 3.44 (2015), pp. 21968–21989. ISSN: 2050-7488, 2050-7496. DOI: 10.1039/C5TA04822B. URL: http://xlink.rsc.org/?DOI=C5TA04822B.

[91] Susanta Haldar et al. "Adsorption of Organic Electron Acceptors on Graphene-like Molecules: Quantum Chemical and Molecular Mechanical Study". en. In: *The Journal of Physical Chemistry C* 116.48 (Dec. 2012), pp. 25328–25336. ISSN: 1932-7447, 1932-7455. DOI: 10.1021/jp3071162. URL: https://pubs.acs.org/doi/10.1021/jp3071162.

[92] Markéta Stachová, Matúš Dubecký, and František Karlický. "Adsorption of atomic and molecular monolayers on Pt-supported graphene". en. In: *Chemical Physics* 564 (Jan. 2023), p. 111713. ISSN: 03010104. DOI: 10.1016/j.chemphys.2022.111713. URL: https://linkinghub.elsevier.com/retrieve/pii/S030101042200266X.

[93] Kaori Takeuchi et al. "Adsorption of CO_2 on Graphene: A Combined TPD, XPS, and vdW-DF Study". en. In: *The Journal of Physical Chemistry C* 121.5 (Feb. 2017), pp. 2807–2814. ISSN: 1932-7447, 1932-7455. DOI: 10.1021/acs.jpcc.6b11373. URL: https://pubs.acs.org/doi/10.1021/acs.jpcc.6b11373.

[94] R. Scott Smith and Bruce D. Kay. "Desorption Kinetics of Carbon Dioxide from a Graphene-Covered Pt(111) Surface". en. In: *The Journal of Physical Chemistry A* 123.15 (Apr. 2019), pp. 3248–3254. ISSN: 1089-5639, 1520-5215. DOI: 10.1021/acs.jpca.9b00674. URL: https://pubs.acs.org/doi/10.1021/acs.jpca.9b00674.

[95] John P. Perdew, Kieron Burke, and Matthias Ernzerhof. "Generalized Gradient Approximation Made Simple". en. In: *Physical Review Letters* 77.18 (Oct. 1996), pp. 3865–3868. ISSN: 0031-9007, 1079-7114. DOI: 10.1103/PhysRevLett.77.3865. URL: https://link.aps.org/doi/10.1103/PhysRevLett.77.3865.

[96] John P. Perdew, Kieron Burke, and Matthias Ernzerhof. "Generalized Gradient Approximation Made Simple [Phys. Rev. Lett. 77, 3865 (1996)]". en. In: *Physical Review Letters* 78.7 (Feb. 1997), pp. 1396–1396. ISSN: 0031-9007, 1079-7114. DOI: 10.1103/PhysRevLett.78.1396. URL: https://link.aps.org/doi/10.1103/PhysRevLett.78.1396 (visited on 12/19/2023).

[97] Axel D. Becke. "Density-functional thermochemistry. III. The role of exact exchange". en. In: *The Journal of Chemical Physics* 98.7 (Apr. 1993), pp. 5648–5652. ISSN: 0021-9606, 1089-7690. DOI: 10.1063/1.464913. URL: https://pubs.aip.org/jcp/article/98/7/5648/842114/Density-functional-thermochemistry-III-The-role-of.

[98] P. J. Stephens et al. "Ab Initio Calculation of Vibrational Absorption and Circular Dichroism Spectra Using Density Functional Force Fields". en. In: *The Journal of Physical Chemistry* 98.45 (Nov. 1994), pp. 11623–11627. ISSN: 0022-3654, 1541-5740. DOI: 10.1021/j100096a001. URL: https://pubs.acs.org/doi/abs/10.1021/j100096a001.

[99] You-Sheng Lin et al. "Long-Range Corrected Hybrid Density Functionals with Improved Dispersion Corrections". en. In: *Journal of Chemical Theory and Computation* 9.1 (Jan. 2013), pp. 263–272. ISSN: 1549-9618, 1549-9626. DOI: 10.1021/ct300715s. URL: https://pubs.acs.org/doi/10.1021/ct300715s.

[100] Narbe Mardirossian and Martin Head-Gordon. "ωB97X-V: A 10-parameter, range-separated hybrid, generalized gradient approximation density functional with nonlocal correlation, designed by a survival-of-the-fittest strategy". en. In: *Physical Chemistry Chemical Physics* 16.21 (2014), p. 9904. ISSN: 1463-9076, 1463-9084. DOI: 10.1039/c3cp54374a. URL: http://xlink.rsc.org/?DOI=c3cp54374a.

[101] Sebastian Kozuch, David Gruzman, and Jan M. L. Martin. "DSD-BLYP: A General Purpose Double Hybrid Density Functional Including Spin Component Scaling and Dispersion Correction". en. In: *The Journal of Physical Chemistry C* 114.48 (Dec. 2010), pp. 20801–20808. ISSN: 1932-7447, 1932-7455. DOI: 10.1021/jp1070852. URL: https://pubs.acs.org/doi/10.1021/jp1070852.

[102] Frank Neese. "Software update: the ORCA program system, version 4.0". en. In: *WIREs Computational Molecular Science* 8.1 (Jan. 2018), e1327. ISSN: 1759-0876, 1759-0884. DOI: 10.1002/wcms.1327. URL: https://wires.onlinelibrary.wiley.com/doi/10.1002/wcms.1327.

[103] Devin A. Matthews et al. "Coupled-cluster techniques for computational chemistry: The ¡span style="font-variant:small-caps;"¿CFOUR¡/span¿ program package". en. In: *The Journal of Chemical Physics* 152.21 (June 2020), p. 214108. ISSN: 0021-9606, 1089-7690. DOI: `10.1063/5.0004837`. URL: `https://pubs.aip.org/jcp/article/152/21/214108/198810/Coupled-cluster-techniques-for-computational` (visited on 12/19/2023).

[104] Christoph Riplinger et al. "Natural triple excitations in local coupled cluster calculations with pair natural orbitals". en. In: *The Journal of Chemical Physics* 139.13 (Oct. 2013), p. 134101. ISSN: 0021-9606, 1089-7690. DOI: `10.1063/1.4821834`. URL: `https://pubs.aip.org/jcp/article/139/13/134101/192939/Natural-triple-excitations-in-local-coupled`.

[105] Christoph Riplinger and Frank Neese. "An efficient and near linear scaling pair natural orbital based local coupled cluster method". en. In: *The Journal of Chemical Physics* 138.3 (Jan. 2013), p. 034106. ISSN: 0021-9606, 1089-7690. DOI: `10.1063/1.4773581`. URL: `https://pubs.aip.org/jcp/article/138/3/034106/192513/An-efficient-and-near-linear-scaling-pair-natural`.

[106] Robert M. Parrish et al. "¡span style="font-variant:small-caps;"¿Psi4¡/span¿ 1.1: An Open-Source Electronic Structure Program Emphasizing Automation, Advanced Libraries, and Interoperability". en. In: *Journal of Chemical Theory and Computation* 13.7 (July 2017), pp. 3185–3197. ISSN: 1549-9618, 1549-9626. DOI: `10.1021/acs.jctc.7b00174`. URL: `https://pubs.acs.org/doi/10.1021/acs.jctc.7b00174` (visited on 12/19/2023).

[107] Paolo Giannozzi et al. "Q ¡span style="font-variant:small-caps;"¿uantum¡/span¿ ESPRESSO toward the exascale". en. In: *The Journal of Chemical Physics* 152.15 (Apr. 2020), p. 154105. ISSN: 0021-9606, 1089-7690. DOI: `10.1063/5.0005082`. URL: `https://pubs.aip.org/jcp/article/152/15/154105/1058748/Quantum-ESPRESSO-toward-the-exascale` (visited on 12/20/2023).

[108] Andrea Dal Corso. "Pseudopotentials periodic table: From H to Pu". en. In: *Computational Materials Science* 95 (Dec. 2014), pp. 337–350. ISSN: 09270256. DOI: `10.1016/j.commatsci.2014.07.043`. URL: `https://linkinghub.elsevier.com/retrieve/pii/S0927025614005187`.

[109] A. Otero-de-la-Roza and Erin R. Johnson. "Non-covalent interactions and thermochemistry using XDM-corrected hybrid and range-separated hybrid density functionals". en. In: *The Journal of Chemical Physics* 138.20 (May 2013), p. 204109. ISSN: 0021-9606, 1089-7690. DOI: `10.1063/1.4807330`. URL: `https://pubs.aip.org/jcp/article/138/20/204109/566187/Non-covalent-interactions-and-thermochemistry`.

[110] M. Dion et al. "Van der Waals Density Functional for General Geometries". In: *Physical Review Letters* 92.24 (June 2004), p. 246401. DOI: `10.1103/PhysRevLett.92.246401`. URL: `https://link.aps.org/doi/10.1103/PhysRevLett.92.246401`.

[111] Kyuho Lee et al. "Higher-accuracy van der Waals density functional". en. In: *Physical Review B* 82.8 (Aug. 2010), p. 081101. ISSN: 1098-0121, 1550-235X. DOI: `10.1103/PhysRevB.82.081101`. URL: `https://link.aps.org/doi/10.1103/PhysRevB.82.081101`.

[112] Jiří Klimeš, David R Bowler, and Angelos Michaelides. "Chemical accuracy for the van der Waals density functional". In: *Journal of Physics: Condensed Matter* 22.2 (Jan. 2010), p. 022201. ISSN: 0953-8984, 1361-648X. DOI: `10.1088/0953-8984/22/2/022201`. URL: `https://iopscience.iop.org/article/10.1088/0953-8984/22/2/022201`.

[113] Jiří Klimeš, David R. Bowler, and Angelos Michaelides. "Van der Waals density functionals applied to solids". In: *Physical Review B* 83.19 (May 2011), p. 195131. DOI: `10.1103/PhysRevB.83.195131`. URL: `https://link.aps.org/doi/10.1103/PhysRevB.83.195131`.

[114] Bruce J Berne, Giovanni Ciccotti, and David F Coker. "Classical and Quantum Dynamics in Condensed Phase Simulations". en. In: *Classical and Quantum Dynamics in Condensed Phase Simulations*. LERICI, Villa Marigola: WORLD SCIENTIFIC, June 1998. ISBN: 9789810234980 9789812839664.

[115] Graeme Henkelman, Blas P. Uberuaga, and Hannes Jónsson. "A climbing image nudged elastic band method for finding saddle points and minimum energy paths". en. In: *The Journal of Chemical Physics* 113.22 (Dec. 2000), pp. 9901–9904. ISSN: 0021-9606, 1089-7690. DOI: 10.1063/1.1329672. URL: https://pubs.aip.org/jcp/article/113/22/9901/185050/A-climbing-image-nudged-elastic-band-method-for.

[116] Ask Hjorth Larsen et al. "The atomic simulation environment—a Python library for working with atoms". In: *Journal of Physics: Condensed Matter* 29.27 (July 2017), p. 273002. ISSN: 0953-8984, 1361-648X. DOI: 10.1088/1361-648X/aa680e. URL: https://iopscience.iop.org/article/10.1088/1361-648X/aa680e.

[117] Lars Goerigk et al. "A look at the density functional theory zoo with the advanced GMTKN55 database for general main group thermochemistry, kinetics and non-covalent interactions". en. In: *Physical Chemistry Chemical Physics* 19.48 (2017), pp. 32184–32215. ISSN: 1463-9076, 1463-9084. DOI: 10.1039/C7CP04913G. URL: http://xlink.rsc.org/?DOI=C7CP04913G.

[118] Frank Neese. "Prediction of molecular properties and molecular spectroscopy with density functional theory: From fundamental theory to exchange-coupling". en. In: *Coordination Chemistry Reviews* 253.5-6 (Mar. 2009), pp. 526–563. ISSN: 00108545. DOI: 10.1016/j.ccr.2008.05.014. URL: https://linkinghub.elsevier.com/retrieve/pii/S0010854508001197.

[119] David Feller and K. D. Jordan. "Estimating the Strength of the Water/Single-Layer Graphite Interaction". en. In: *The Journal of Physical Chemistry A* 104.44 (Nov. 2000), pp. 9971–9975. ISSN: 1089-5639, 1520-5215. DOI: 10.1021/jp001766o. URL: https://pubs.acs.org/doi/10.1021/jp001766o.

[120] Stefan Grimme, Christian Mück-Lichtenfeld, and Jens Antony. "Noncovalent Interactions between Graphene Sheets and in Multishell (Hyper)Fullerenes". en. In: *The Journal of Physical Chemistry C* 111.30 (Aug. 2007), pp. 11199–11207. ISSN: 1932-7447, 1932-7455. DOI: 10.1021/jp0720791. URL: https://pubs.acs.org/doi/10.1021/jp0720791.

[121] Jens Antony and Stefan Grimme. "Structures and interaction energies of stacked graphene–nucleobase complexes". en. In: *Physical Chemistry Chemical Physics* 10.19 (2008), p. 2722. ISSN: 1463-9076, 1463-9084. DOI: 10.1039/b718788b. URL: http://xlink.rsc.org/?DOI=b718788b (visited on 12/22/2023).

[122] Yoshifumi Nishimura et al. "Quantum Chemical Estimation of Acetone Physisorption on Graphene Using Combined Basis Set and Size Extrapolation Schemes". en. In: *The Journal of Physical Chemistry C* 121.16 (Apr. 2017), pp. 8999–9010. ISSN: 1932-7447, 1932-7455. DOI: 10.1021/acs.jpcc.6b13002. URL: https://pubs.acs.org/doi/10.1021/acs.jpcc.6b13002.

[123] Jan Gerit Brandenburg et al. "Physisorption of Water on Graphene: Subchemical Accuracy from Many-Body Electronic Structure Methods". en. In: *The Journal of Physical Chemistry Letters* 10.3 (Feb. 2019), pp. 358–368. ISSN: 1948-7185, 1948-7185. DOI: 10.1021/acs.jpclett.8b03679. URL: https://pubs.acs.org/doi/10.1021/acs.jpclett.8b03679 (visited on 12/22/2023).

[124] Kenneth D. Jordan and Andreas Heßelmann. "Comment on "Physisorption of Water on Graphene: Subchemical Accuracy from Many-Body Electronic Structure Methods"". en. In: *The Journal of Physical Chemistry C* 123.15 (Apr. 2019), pp. 10163–10165. ISSN: 1932-7447, 1932-7455. DOI: 10.1021/acs.jpcc.9b02326. URL: https://pubs.acs.org/doi/10.1021/acs.jpcc.9b02326.

[125] Christopher Ehlert, Anna Piras, and Ganna Gryn'ova. "CO_2 on Graphene: Benchmarking Computational Approaches to Noncovalent Interactions". en. In: *ACS Omega* 8.39 (Oct. 2023), pp. 35768–35778. ISSN: 2470-1343, 2470-1343. DOI: 10.1021/acsomega.3c03251. URL: https://pubs.acs.org/doi/10.1021/acsomega.3c03251.

[126] Kou-San Ju and Rebecca E. Parales. "Nitroaromatic Compounds, from Synthesis to Biodegradation". en. In: *Microbiology and Molecular Biology Reviews* 74.2 (June 2010), pp. 250–272. ISSN: 1092-2172, 1098-5557. DOI: 10.1128/MMBR.00006-10. URL: https://journals.asm.org/doi/10.1128/MMBR.00006-10 (visited on 12/24/2023).

[127] S Letzel. "Exposure to nitroaromatic explosives and health effects during disposal of military waste". en. In: *Occupational and Environmental Medicine* 60.7 (July 2003), pp. 483–488. ISSN: 1351-0711. DOI: 10.1136/oem.60.7.483. URL: https://oem.bmj.com/lookup/doi/10.1136/oem.60.7.483.

[128] Suman Singh. "Sensors—An effective approach for the detection of explosives". en. In: *Journal of Hazardous Materials* 144.1-2 (June 2007), pp. 15–28. ISSN: 03043894. DOI: 10.1016/j.jhazmat.2007.02.018. URL: https://linkinghub.elsevier.com/retrieve/pii/S0304389407002397.

[129] Leonardo C. Pacheco-Londono et al. "Vibrational spectroscopy standoff detection of explosives". en. In: *Analytical and Bioanalytical Chemistry* 395.2 (Sept. 2009), pp. 323–335. ISSN: 1618-2642, 1618-2650. DOI: 10.1007/s00216-009-2954-y. URL: http://link.springer.com/10.1007/s00216-009-2954-y.

[130] M Walsh. "Determination of nitroaromatic, nitramine, and nitrate ester explosives in soil by gas chromatography and an electron capture detector". In: *Talanta* 54.3 (May 2001), pp. 427–438. ISSN: 00399140. DOI: 10.1016/S0039-9140(00)00541-5. URL: https://linkinghub.elsevier.com/retrieve/pii/S0039914000005415.

[131] Christopher Mullen et al. "Detection of Explosives and Explosives-Related Compounds by Single Photon Laser Ionization Time-of-Flight Mass Spectrometry". en. In: *Analytical Chemistry* 78.11 (June 2006), pp. 3807–3814. ISSN: 0003-2700, 1520-6882. DOI: 10.1021/ac060190h. URL: https://pubs.acs.org/doi/10.1021/ac060190h.

[132] Avraham Bromberg and Richard A. Mathies. "Homogeneous Immunoassay for Detection of TNT and Its Analogues on a Microfabricated Capillary Electrophoresis Chip". en. In: *Analytical Chemistry* 75.5 (Mar. 2003), pp. 1188–1195. ISSN: 0003-2700, 1520-6882. DOI: 10.1021/ac020599g. URL: https://pubs.acs.org/doi/10.1021/ac020599g.

[133] Chun Kiang Chua, Martin Pumera, and Lubomír Rulíšek. "Reduction Pathways of 2,4,6-Trinitrotoluene: An Electrochemical and Theoretical Study". en. In: *The Journal of Physical Chemistry C* 116.6 (Feb. 2012), pp. 4243–4251. ISSN: 1932-7447, 1932-7455. DOI: 10.1021/jp209631x. URL: https://pubs.acs.org/doi/10.1021/jp209631x.

[134] Ying Teng Yew, Adriano Ambrosi, and Martin Pumera. "Nitroaromatic explosives detection using electrochemically exfoliated graphene". en. In: *Scientific Reports* 6.1 (Sept. 2016), p. 33276. ISSN: 2045-2322. DOI: 10.1038/srep33276. URL: https://www.nature.com/articles/srep33276 (visited on 12/24/2023).

[135] Hong-Xia Zhang et al. "Electrochemical Sensor for Detecting Ultratrace Nitroaromatic Compounds Using Mesoporous SiO_2-Modified Electrode". en. In: *Analytical Chemistry* 78.6 (Mar. 2006), pp. 1967–1971. ISSN: 0003-2700, 1520-6882. DOI: 10.1021/ac051826s. URL: https://pubs.acs.org/doi/10.1021/ac051826s (visited on 12/24/2023).

[136] Virendra Singh et al. "Graphene based materials: Past, present and future". en. In: *Progress in Materials Science* 56.8 (Oct. 2011), pp. 1178–1271. ISSN: 00796425. DOI: 10.1016/j.pmatsci.2011.03.003. URL: https://linkinghub.elsevier.com/retrieve/pii/S0079642511000442 (visited on 12/24/2023).

[137] Martin Pumera. "Electrochemistry of graphene, graphene oxide and other graphenoids: Review". en. In: *Electrochemistry Communications* 36 (Nov. 2013), pp. 14–18. ISSN: 13882481. DOI: 10.1016/j.elecom.2013.08.028. URL: https://linkinghub.elsevier.com/retrieve/pii/S1388248113003433.

[138] Xibin Zhou et al. "Pd Nanoparticles on Functionalized Graphene for Excellent Detection of Nitro aromatic Compounds". en. In: *Electrochimica Acta* 119 (Feb. 2014), pp. 243–250. ISSN: 00134686. DOI: 10.1016/j.electacta.2013.10.197. URL: https://linkinghub.elsevier.com/retrieve/pii/S0013468613021695.

[139] Tzu Hui Seah et al. "Towards Graphane Applications in Security: The Electrochemical Detection of Trinitrotoluene in Seawater on Hydrogenated Graphene". en. In: *Electroanalysis* 26.1 (Jan. 2014), pp. 62–68. ISSN: 1040-0397, 1521-4109. DOI: 10.1002/elan.201300228. URL: https://analyticalsciencejournals.onlinelibrary.wiley.com/doi/10.1002/elan.201300228.

[140] Beng Khong Ong et al. "Graphenes Prepared by Hummers, Staudenmaier and Hofmann Methods for Analysis of TNT-Based Nitroaromatic Explosives in Seawater". en. In: *Electroanalysis* 24.11 (Nov. 2012), pp. 2085–2093. ISSN: 1040-0397, 1521-4109. DOI: 10.1002/elan.201200474. URL: https://analyticalsciencejournals.onlinelibrary.wiley.com/doi/10.1002/elan.201200474.

[141] Ruizhong Zhang et al. "Nitrogen and sulfur co-doped graphene nanoribbons: A novel metal-free catalyst for high performance electrochemical detection of 2, 4, 6-trinitrotoluene (TNT)". en. In: *Carbon* 126 (Jan. 2018), pp. 328–337. ISSN: 00086223. DOI: 10.1016/j.carbon.2017.10.042. URL: https://linkinghub.elsevier.com/retrieve/pii/S0008622317310436 (visited on 12/27/2023).

[142] Ti-Wei Chen et al. "Enhanced electrocatalytic activity of nitrogen-doped graphene for the reduction of nitro explosives". en. In: *Electrochemistry Communications* 16.1 (Mar. 2012), pp. 30–33. ISSN: 13882481. DOI: 10.1016/j.elecom.2011.12.016. URL: https://linkinghub.elsevier.com/retrieve/pii/S1388248111005133.

[143] Shu Min Tan, Chun Kiang Chua, and Martin Pumera. "Graphenes prepared from multi-walled carbon nanotubes and stacked graphene nanofibers for detection of 2,4,6-trinitrotoluene (TNT) in seawater". en. In: *The Analyst* 138.6 (2013), p. 1700. ISSN: 0003-2654, 1364-5528. DOI: 10.1039/c3an00089c. URL: http://xlink.rsc.org/?DOI=c3an00089c.

[144] Madeline Shuhua Goh and Martin Pumera. "Graphene-based electrochemical sensor for detection of 2,4,6-trinitrotoluene (TNT) in seawater: the comparison of single-, few-, and multilayer graphene nanoribbons and graphite microparticles". en. In: *Analytical and Bioanalytical Chemistry* 399.1 (Jan. 2011), pp. 127–131. ISSN: 1618-2642, 1618-2650. DOI: 10.1007/s00216-010-4338-8. URL: http://link.springer.com/10.1007/s00216-010-4338-8.

[145] Hwee Ling Poh et al. "Graphenes prepared by Staudenmaier, Hofmann and Hummers methods with consequent thermal exfoliation exhibit very different electrochemical properties". en. In: *Nanoscale* 4.11 (2012), p. 3515. ISSN: 2040-3364, 2040-3372. DOI: 10.1039/c2nr30490b. URL: http://xlink.rsc.org/?DOI=c2nr30490b (visited on 12/27/2023).

[146] Jisoo Park et al. "Band gap engineering of graphene oxide for ultrasensitive NO2 gas sensing". en. In: *Carbon* 159 (Apr. 2020), pp. 175–184. ISSN: 00086223. DOI: 10.1016/j.carbon.2019.11.063. URL: https://linkinghub.elsevier.com/retrieve/pii/S0008622319311959.

[147] Sindy J. Rodríguez and Eduardo A. Albanesi. "Electronic transport in a graphene single layer: application in amino acid sensing". en. In: *Physical Chemistry Chemical Physics* 21.2 (2019), pp. 597–606. ISSN: 1463-9076, 1463-9084. DOI: 10.1039/C8CP05093G. URL: http://xlink.rsc.org/?DOI=C8CP05093G (visited on 12/28/2023).

[148] S.J. Rodríguez, L. Makinistian, and E.A. Albanesi. "Graphene for amino acid biosensing: Theoretical study of the electronic transport". en. In: *Applied Surface Science* 419 (Oct. 2017), pp. 540–545. ISSN: 01694332. DOI: 10.1016/j.apsusc.2017.05.031. URL: https://linkinghub.elsevier.com/retrieve/pii/S016943321731334X.

[149] Xiaoxiao Chen and Baoliang Chen. "Macroscopic and Spectroscopic Investigations of the Adsorption of Nitroaromatic Compounds on Graphene Oxide, Reduced Graphene Oxide, and Graphene Nanosheets". en. In: *Environmental Science & Technology* 49.10 (May 2015), pp. 6181–6189. ISSN: 0013-936X, 1520-5851. DOI: 10.1021/es5054946. URL: https://pubs.acs.org/doi/10.1021/es5054946 (visited on 12/28/2023).

[150] Tugce Irfan Akay, Daniele Toffoli, and Hande Ustunel. "Combined effect of point defects and layer number on the adsorption of benzene and toluene on graphene". en. In: *Applied Surface Science* 480 (June 2019), pp. 1063–1069. ISSN: 01694332. DOI: 10.1016/j.apsusc.2019.02.040. URL: https://linkinghub.elsevier.com/retrieve/pii/S0169433219303721.

[151] Øyvind Borck and Elsebeth Schröder. "Methylbenzenes on graphene". en. In: *Surface Science* 664 (Oct. 2017), pp. 162–167. ISSN: 00396028. DOI: 10.1016/j.susc.2017.06.012. URL: https://linkinghub.elsevier.com/retrieve/pii/S003960281730362X.

[152]   Dalia Daggag, Taylor Dorlus, and Tandabany Dinadayalane. "Binding of histidine and pro-
        line with graphene: DFT study". en. In: *Chemical Physics Letters* 730 (Sept. 2019), pp. 147–
        152. ISSN: 00092614. DOI: 10.1016/j.cplett.2019.05.043. URL: https://linkinghub.
        elsevier.com/retrieve/pii/S000926141930449X.

[153]   Aniruddha Molla et al. "Selective adsorption of organic dyes on graphene oxide: Theoretical
        and experimental analysis". en. In: *Applied Surface Science* 464 (Jan. 2019), pp. 170–177.
        ISSN: 01694332. DOI: 10.1016/j.apsusc.2018.09.056. URL: https://linkinghub.
        elsevier.com/retrieve/pii/S0169433218324735.

[154]   Junsu Lee et al. "Ab initio study of adsorption properties of hazardous organic molecules
        on graphene: Phenol, phenyl azide, and phenylnitrene". en. In: *Chemical Physics Letters*
        618 (Jan. 2015), pp. 57–62. ISSN: 00092614. DOI: 10.1016/j.cplett.2014.10.064. URL:
        https://linkinghub.elsevier.com/retrieve/pii/S0009261414009233.

[155]   Diego López Carballeira et al. "A computational study of the interaction of graphene
        structures with biomolecular units". en. In: *Physical Chemistry Chemical Physics* 18.22
        (2016), pp. 15312–15321. ISSN: 1463-9076, 1463-9084. DOI: 10.1039/C6CP00545D. URL:
        http://xlink.rsc.org/?DOI=C6CP00545D (visited on 12/28/2023).

[156]   C. Tarrio and S. E. Schnatterly. "Interband transitions, plasmons, and dispersion in hexag-
        onal boron nitride". en. In: *Physical Review B* 40.11 (Oct. 1989), pp. 7852–7859. ISSN:
        0163-1829. DOI: 10.1103/PhysRevB.40.7852. URL: https://link.aps.org/doi/10.
        1103/PhysRevB.40.7852.

[157]   Kenji Watanabe, Takashi Taniguchi, and Hisao Kanda. "Direct-bandgap properties and
        evidence for ultraviolet lasing of hexagonal boron nitride single crystal". en. In: *Nature Ma-
        terials* 3.6 (June 2004), pp. 404–409. ISSN: 1476-1122, 1476-4660. DOI: 10.1038/nmat1134.
        URL: https://www.nature.com/articles/nmat1134 (visited on 01/29/2024).

[158]   B. Hourahine et al. "DFTB+, a software package for efficient approximate density functional
        theory based atomistic simulations". en. In: *The Journal of Chemical Physics* 152.12 (Mar.
        2020), p. 124101. ISSN: 0021-9606, 1089-7690. DOI: 10.1063/1.5143190. URL: https:
        //pubs.aip.org/jcp/article/152/12/124101/953756/DFTB-a-software-package-
        for-efficient-approximate.

[159]   Edward G. Hohenstein et al. "Large-scale symmetry-adapted perturbation theory compu-
        tations via density fitting and Laplace transformation techniques: Investigating the funda-
        mental forces of DNA-intercalator interactions". en. In: *The Journal of Chemical Physics*
        135.17 (Nov. 2011), p. 174107. ISSN: 0021-9606, 1089-7690. DOI: 10.1063/1.3656681. URL:
        https://pubs.aip.org/jcp/article/135/17/174107/189720/Large-scale-symmetry-
        adapted-perturbation-theory (visited on 12/30/2023).

[160]   G. Te Velde et al. "Chemistry with ADF". en. In: *Journal of Computational Chemistry*
        22.9 (July 2001), pp. 931–967. ISSN: 0192-8651, 1096-987X. DOI: 10.1002/jcc.1056. URL:
        https://onlinelibrary.wiley.com/doi/10.1002/jcc.1056 (visited on 12/30/2023).

[161]   M. J. Frisch et al. *Gaussian 16 Rev. C.01*. Wallingford, CT, 2016.

[162]   Filipe Menezes and Grzegorz Maria Popowicz. "How to Catch the Ball: Fullerene Binding to
        the Corannulene Pincer". en. In: *Molecules* 27.12 (June 2022), p. 3838. ISSN: 1420-3049. DOI:
        10.3390/molecules27123838. URL: https://www.mdpi.com/1420-3049/27/12/3838.

[163]   Wei Shao and Xiaodong Zhang. "Atomic-level engineering of two-dimensional electrocata-
        lysts for CO$_2$ reduction". en. In: *Nanoscale* 13.15 (2021), pp. 7081–7095. ISSN: 2040-3364,
        2040-3372. DOI: 10.1039/D1NR00649E. URL: http://xlink.rsc.org/?DOI=D1NR00649E.

[164]   Qiaofeng Yao et al. "Engineering Functional Metal Materials at the Atomic Level". en.
        In: *Advanced Materials* 30.47 (Nov. 2018), p. 1802751. ISSN: 0935-9648, 1521-4095. DOI:
        10.1002/adma.201802751. URL: https://onlinelibrary.wiley.com/doi/10.1002/
        adma.201802751.

[165]   Harry L. Tuller and Sean R. Bishop. "Point Defects in Oxides: Tailoring Materials Through
        Defect Engineering". en. In: *Annual Review of Materials Research* 41.1 (Aug. 2011), pp. 369–
        398. ISSN: 1531-7331, 1545-4118. DOI: 10.1146/annurev-matsci-062910-100442. URL:
        https://www.annualreviews.org/doi/10.1146/annurev-matsci-062910-100442.

[166] Steven G. Louie et al. "Discovering and understanding materials through computation". en. In: *Nature Materials* 20.6 (June 2021), pp. 728–735. ISSN: 1476-1122, 1476-4660. DOI: 10.1038/s41563-021-01015-1. URL: https://www.nature.com/articles/s41563-021-01015-1.

[167] Nicola Marzari, Andrea Ferretti, and Chris Wolverton. "Electronic-structure methods for materials design". en. In: *Nature Materials* 20.6 (June 2021), pp. 736–749. ISSN: 1476-1122, 1476-4660. DOI: 10.1038/s41563-021-01013-3. URL: https://www.nature.com/articles/s41563-021-01013-3.

[168] Jacob Fish, Gregory J. Wagner, and Sinan Keten. "Mesoscopic and multiscale modelling in materials". en. In: *Nature Materials* 20.6 (June 2021), pp. 774–786. ISSN: 1476-1122, 1476-4660. DOI: 10.1038/s41563-020-00913-0. URL: https://www.nature.com/articles/s41563-020-00913-0.

[169] Chenru Duan, Aditya Nandy, and Heather J. Kulik. "Machine Learning for the Discovery, Design, and Engineering of Materials". en. In: *Annual Review of Chemical and Biomolecular Engineering* 13.1 (June 2022), pp. 405–429. ISSN: 1947-5438, 1947-5446. DOI: 10.1146/annurev-chembioeng-092320-120230. URL: https://www.annualreviews.org/doi/10.1146/annurev-chembioeng-092320-120230 (visited on 12/30/2023).

[170] Xien Liu and Liming Dai. "Carbon-based metal-free catalysts". en. In: *Nature Reviews Materials* 1.11 (Sept. 2016), p. 16064. ISSN: 2058-8437. DOI: 10.1038/natrevmats.2016.64. URL: https://www.nature.com/articles/natrevmats201664.

[171] Phaedon Avouris, Zhihong Chen, and Vasili Perebeinos. "Carbon-based electronics". en. In: *Nature Nanotechnology* 2.10 (Oct. 2007), pp. 605–615. ISSN: 1748-3387, 1748-3395. DOI: 10.1038/nnano.2007.300. URL: https://www.nature.com/articles/nnano.2007.300.

[172] L. A. Ponomarenko et al. "Chaotic Dirac Billiard in Graphene Quantum Dots". en. In: *Science* 320.5874 (Apr. 2008), pp. 356–358. ISSN: 0036-8075, 1095-9203. DOI: 10.1126/science.1154663. URL: https://www.science.org/doi/10.1126/science.1154663 (visited on 12/30/2023).

[173] Ahmadreza Ghaffarkhah et al. "Synthesis, Applications, and Prospects of Graphene Quantum Dots: A Comprehensive Review". en. In: *Small* 18.2 (Jan. 2022), p. 2102683. ISSN: 1613-6810, 1613-6829. DOI: 10.1002/smll.202102683. URL: https://onlinelibrary.wiley.com/doi/10.1002/smll.202102683.

[174] Kisuk Kang et al. "Electrodes with High Power and High Capacity for Rechargeable Lithium Batteries". en. In: *Science* 311.5763 (Feb. 2006), pp. 977–980. ISSN: 0036-8075, 1095-9203. DOI: 10.1126/science.1122152. URL: https://www.science.org/doi/10.1126/science.1122152 (visited on 01/01/2024).

[175] Jun Lu et al. "A lithium–oxygen battery based on lithium superoxide". en. In: *Nature* 529.7586 (Jan. 2016), pp. 377–382. ISSN: 0028-0836, 1476-4687. DOI: 10.1038/nature16484. URL: https://www.nature.com/articles/nature16484 (visited on 01/01/2024).

[176] Miao Zhong et al. "Accelerated discovery of CO2 electrocatalysts using active machine learning". en. In: *Nature* 581.7807 (May 2020), pp. 178–183. ISSN: 0028-0836, 1476-4687. DOI: 10.1038/s41586-020-2242-8. URL: https://www.nature.com/articles/s41586-020-2242-8.

[177] Ryan T. Hannagan et al. "First-principles design of a single-atom–alloy propane dehydrogenation catalyst". en. In: *Science* 372.6549 (June 2021), pp. 1444–1447. ISSN: 0036-8075, 1095-9203. DOI: 10.1126/science.abg8389. URL: https://www.science.org/doi/10.1126/science.abg8389 (visited on 01/01/2024).

[178] Xiaoling Guo et al. "Conjugated polymers with defined chemical structure as model carbon catalysts for nitro reduction". en. In: *RSC Advances* 6.101 (2016), pp. 99570–99576. ISSN: 2046-2069. DOI: 10.1039/C6RA18201A. URL: http://xlink.rsc.org/?DOI=C6RA18201A.

[179] Peng Zhang et al. "Biomass-Derived Carbon Nanospheres with Turbostratic Structure as Metal-Free Catalysts for Selective Hydrogenation of o-Chloronitrobenzene". en. In: *ACS Sustainable Chemistry & Engineering* 5.9 (Sept. 2017), pp. 7481–7485. ISSN: 2168-0485, 2168-0485. DOI: 10.1021/acssuschemeng.7b01280. URL: https://pubs.acs.org/doi/10.1021/acssuschemeng.7b01280.

[180] Nasuha Rohaizad, Zdeněk Sofer, and Martin Pumera. "Boron and nitrogen dopants in graphene have opposite effects on the electrochemical detection of explosive nitroaromatic compounds". en. In: *Electrochemistry Communications* 112 (Mar. 2020), p. 106660. ISSN: 13882481. DOI: 10.1016/j.elecom.2020.106660. URL: https://linkinghub.elsevier.com/retrieve/pii/S1388248120300102 (visited on 01/01/2024).

[181] Cesar Gabriel Vera de la Garza, Esau Martínez Olmedo, and Serguei Fomine. "Electronic structure of boron and nitrogen doped isomeric graphene nanoflakes". en. In: *Computational and Theoretical Chemistry* 1151 (Mar. 2019), pp. 12–23. ISSN: 2210271X. DOI: 10.1016/j.comptc.2019.01.022. URL: https://linkinghub.elsevier.com/retrieve/pii/S2210271X19300301.

[182] P Mocci et al. "Opto-Electronic properties of BN-ring insertions in Circumacenes: the case of Coronene and Ovalene". In: *Journal of Physics: Conference Series* 1548.1 (May 2020), p. 012028. ISSN: 1742-6588, 1742-6596. DOI: 10.1088/1742-6596/1548/1/012028. URL: https://iopscience.iop.org/article/10.1088/1742-6596/1548/1/012028.

[183] Shun-Chiao Chan et al. "DFT calculation in design of near-infrared absorbing nitrogen-doped graphene quantum dots". en. In: *Physical Chemistry Chemical Physics* 24.3 (2022), pp. 1580–1589. ISSN: 1463-9076, 1463-9084. DOI: 10.1039/D1CP04572E. URL: http://xlink.rsc.org/?DOI=D1CP04572E.

[184] Jeffrey B. Schriber et al. "A Combined Selected Configuration Interaction and Many-Body Treatment of Static and Dynamical Correlation in Oligoacenes". en. In: *Journal of Chemical Theory and Computation* 14.12 (Dec. 2018), pp. 6295–6305. ISSN: 1549-9618, 1549-9626. DOI: 10.1021/acs.jctc.8b00877. URL: https://pubs.acs.org/doi/10.1021/acs.jctc.8b00877.

[185] Wataru Mizukami, Yuki Kurashige, and Takeshi Yanai. "More Electrons Make a Difference: Emergence of Many Radicals on Graphene Nanoribbons Studied by *Ab Initio* DMRG Theory". en. In: *Journal of Chemical Theory and Computation* 9.1 (Jan. 2013), pp. 401–407. ISSN: 1549-9618, 1549-9626. DOI: 10.1021/ct3008974. URL: https://pubs.acs.org/doi/10.1021/ct3008974 (visited on 01/30/2024).

[186] C. David Sherrill and Henry F. Schaefer. "The Configuration Interaction Method: Advances in Highly Correlated Approaches". en. In: *Advances in Quantum Chemistry*. Vol. 34. Elsevier, 1999, pp. 143–269. ISBN: 9780120348343. DOI: 10.1016/S0065-3276(08)60532-8. URL: https://linkinghub.elsevier.com/retrieve/pii/S0065327608605328.

[187] Zhendong Li. "Stochastic many-body perturbation theory for electron correlation energies". en. In: *The Journal of Chemical Physics* 151.24 (Dec. 2019), p. 244114. ISSN: 0021-9606, 1089-7690. DOI: 10.1063/1.5128719. URL: https://pubs.aip.org/jcp/article/151/24/244114/597210/Stochastic-many-body-perturbation-theory-for.

[188] Péter G. Szalay et al. "Multiconfiguration Self-Consistent Field and Multireference Configuration Interaction Methods and Applications". en. In: *Chemical Reviews* 112.1 (Jan. 2012), pp. 108–181. ISSN: 0009-2665, 1520-6890. DOI: 10.1021/cr200137a. URL: https://pubs.acs.org/doi/10.1021/cr200137a.

[189] K. Suzuki and R. Okamoto. "Perturbation Theory for Quasidegenerate System in Quantum Mechanics". en. In: *Progress of Theoretical Physics* 72.3 (Sept. 1984), pp. 534–548. ISSN: 0033-068X, 1347-4081. DOI: 10.1143/PTP.72.534. URL: https://academic.oup.com/ptp/article-lookup/doi/10.1143/PTP.72.534.

[190] Vladimir V. Ivanov, Dmitry I. Lyakh, and Ludwik Adamowicz. "Multireference state-specific coupled-cluster methods. State-of-the-art and perspectives". en. In: *Physical Chemistry Chemical Physics* 11.14 (2009), p. 2355. ISSN: 1463-9076, 1463-9084. DOI: 10.1039/b818590p. URL: http://xlink.rsc.org/?DOI=b818590p.

[191] Hong Jiang. "First-principles approaches for strongly correlated materials: A theoretical chemistry perspective". en. In: *International Journal of Quantum Chemistry* 115.11 (June 2015), pp. 722–730. ISSN: 0020-7608, 1097-461X. DOI: 10.1002/qua.24905. URL: https://onlinelibrary.wiley.com/doi/10.1002/qua.24905.

[192] Jeng-Da Chai. "Density functional theory with fractional orbital occupations". en. In: *The Journal of Chemical Physics* 136.15 (Apr. 2012), p. 154104. ISSN: 0021-9606, 1089-7690. DOI: 10.1063/1.3703894. URL: https://pubs.aip.org/jcp/article/136/15/154104/941635/Density-functional-theory-with-fractional-orbital (visited on 01/19/2024).

[193] Aron J. Cohen, Paula Mori-Sánchez, and Weitao Yang. "Challenges for Density Functional Theory". en. In: *Chemical Reviews* 112.1 (Jan. 2012), pp. 289–320. ISSN: 0009-2665, 1520-6890. DOI: 10.1021/cr200107z. URL: https://pubs.acs.org/doi/10.1021/cr200107z.

[194] Noèlia Pueyo Bellafont et al. "Assessing the ability of DFT methods to describe static electron correlation effects: CO core level binding energies as a representative case". en. In: *The Journal of Chemical Physics* 147.2 (July 2017), p. 024106. ISSN: 0021-9606, 1089-7690. DOI: 10.1063/1.4991833. URL: https://pubs.aip.org/jcp/article/147/2/024106/1062482/Assessing-the-ability-of-DFT-methods-to-describe.

[195] Eloy Ramos-Cordoba and Eduard Matito. "Local Descriptors of Dynamic and Nondynamic Correlation". en. In: *Journal of Chemical Theory and Computation* 13.6 (June 2017), pp. 2705–2711. ISSN: 1549-9618, 1549-9626. DOI: 10.1021/acs.jctc.7b00293. URL: https://pubs.acs.org/doi/10.1021/acs.jctc.7b00293.

[196] Wei Chen and H. Bernhard Schlegel. "Evaluation of $\mathbf{S}$ 2 for correlated wave functions and spin projection of unrestricted Mo/ller–Plesset perturbation theory". en. In: *The Journal of Chemical Physics* 101.7 (Oct. 1994), pp. 5957–5968. ISSN: 0021-9606, 1089-7690. DOI: 10.1063/1.467312. URL: https://pubs.aip.org/jcp/article/101/7/5957/165132/Evaluation-of-S2-for-correlated-wave-functions-and.

[197] Stefan Grimme and Andreas Hansen. "A Practicable Real-Space Measure and Visualization of Static Electron-Correlation Effects". en. In: *Angewandte Chemie International Edition* 54.42 (Oct. 2015), pp. 12308–12313. ISSN: 1433-7851, 1521-3773. DOI: 10.1002/anie.201501887. URL: https://onlinelibrary.wiley.com/doi/10.1002/anie.201501887.

[198] Timothy J. Lee et al. "Theoretical investigations of molecules composed only of fluorine, oxygen and nitrogen: determination of the equilibrium structures of FOOF, (NO)2 and FNNF and the transition state structure for FNNF cis-trans isomerization". en. In: *Theoretica Chimica Acta* 75.2 (1989), pp. 81–98. ISSN: 0040-5744, 1432-2234. DOI: 10.1007/BF00527711. URL: http://link.springer.com/10.1007/BF00527711 (visited on 01/30/2024).

[199] Jeng-Da Chai and Martin Head-Gordon. "Long-range corrected hybrid density functionals with damped atom–atom dispersion corrections". en. In: *Physical Chemistry Chemical Physics* 10.44 (2008), p. 6615. ISSN: 1463-9076, 1463-9084. DOI: 10.1039/b810189b. URL: http://xlink.rsc.org/?DOI=b810189b.

[200] Bin Zhou et al. "Benchmark study of ionization potentials and electron affinities of armchair single-walled carbon nanotubes using density functional theory". In: *Journal of Physics: Condensed Matter* 30.21 (May 2018), p. 215501. ISSN: 0953-8984, 1361-648X. DOI: 10.1088/1361-648X/aabd18. URL: https://iopscience.iop.org/article/10.1088/1361-648X/aabd18.

[201] Stefan Grimme, Stephan Ehrlich, and Lars Goerigk. "Effect of the damping function in dispersion corrected density functional theory". en. In: *Journal of Computational Chemistry* 32.7 (May 2011), pp. 1456–1465. ISSN: 0192-8651, 1096-987X. DOI: 10.1002/jcc.21759. URL: https://onlinelibrary.wiley.com/doi/10.1002/jcc.21759.

[202] Jianmin Tao et al. "Climbing the Density Functional Ladder: Nonempirical Meta–Generalized Gradient Approximation Designed for Molecules and Solids". en. In: *Physical Review Letters* 91.14 (Sept. 2003), p. 146401. ISSN: 0031-9007, 1079-7114. DOI: 10.1103/PhysRevLett.91.146401. URL: https://link.aps.org/doi/10.1103/PhysRevLett.91.146401 (visited on 12/30/2023).

[203] Yan Zhao and Donald G. Truhlar. "The M06 suite of density functionals for main group thermochemistry, thermochemical kinetics, noncovalent interactions, excited states, and transition elements: two new functionals and systematic testing of four M06-class functionals and 12 other functionals". en. In: *Theoretical Chemistry Accounts* 120.1-3 (May 2008), pp. 215–241. ISSN: 1432-881X, 1432-2234. DOI: 10.1007/s00214-007-0310-x. URL: https://link.springer.com/10.1007/s00214-007-0310-x.

[204] Steven E. Wheeler and K. N. Houk. "Integration Grid Errors for Meta-GGA-Predicted Reaction Energies: Origin of Grid Errors for the M06 Suite of Functionals". en. In: *Journal of Chemical Theory and Computation* 6.2 (Feb. 2010), pp. 395–404. ISSN: 1549-9618, 1549-9626. DOI: 10.1021/ct900639j. URL: https://pubs.acs.org/doi/10.1021/ct900639j.

[205] Johannes Hachmann et al. "The radical character of the acenes: A density matrix renormalization group study". en. In: *The Journal of Chemical Physics* 127.13 (Oct. 2007), p. 134309. ISSN: 0021-9606, 1089-7690. DOI: 10.1063/1.2768362. URL: https://pubs.aip.org/jcp/article/127/13/134309/567089/The-radical-character-of-the-acenes-A-density.

[206] Christoph Alexander Bauer, Andreas Hansen, and Stefan Grimme. "The Fractional Occupation Number Weighted Density as a Versatile Analysis Tool for Molecules with a Complicated Electronic Structure". en. In: *Chemistry – A European Journal* 23.25 (May 2017), pp. 6150–6164. ISSN: 0947-6539, 1521-3765. DOI: 10.1002/chem.201604682. URL: https://chemistry-europe.onlinelibrary.wiley.com/doi/10.1002/chem.201604682.

[207] T Koopmans. "Über die Zuordnung von Wellenfunktionen und Eigenwerten zu den Einzelnen Elektronen Eines Atoms". de. In: *Physica* 1.1-6 (Jan. 1934), pp. 104–113. ISSN: 00318914. DOI: 10.1016/S0031-8914(34)90011-2. URL: https://linkinghub.elsevier.com/retrieve/pii/S0031891434900112.

[208] J. F. Janak. "Proof that $delta$ E δn_i = ϵ in density-functional theory". en. In: *Physical Review B* 18.12 (Dec. 1978), pp. 7165–7168. ISSN: 0163-1829. DOI: 10.1103/PhysRevB.18.7165. URL: https://link.aps.org/doi/10.1103/PhysRevB.18.7165.

[209] Gang Zhang and Charles B. Musgrave. "Comparison of DFT Methods for Molecular Orbital Eigenvalue Calculations". en. In: *The Journal of Physical Chemistry A* 111.8 (Mar. 2007), pp. 1554–1561. ISSN: 1089-5639, 1520-5215. DOI: 10.1021/jp061633o. URL: https://pubs.acs.org/doi/10.1021/jp061633o.

[210] Junming Ho and Mehmed Z. Ertem. "Calculating Free Energy Changes in Continuum Solvation Models". en. In: *The Journal of Physical Chemistry B* 120.7 (Feb. 2016), pp. 1319–1329. ISSN: 1520-6106, 1520-5207. DOI: 10.1021/acs.jpcb.6b00164. URL: https://pubs.acs.org/doi/10.1021/acs.jpcb.6b00164.

Appendix A

Appendix

Additional data, including molecular structures, is available in the Supporting Information of the paper and preprints corresponding to the relative chapters of this thesis. References to these data are included in the **Conclusions** section of each Chapter.

A.1   Chapter 3

Table A.1: Size dependency of the B3LYP-D3/def2-TZVP interaction energies (in kJ mol^{-1}) of CO_2 on various graphene nanoflakes models. Size is expressed as the number of carbon atoms in the model.

Model	Size	Global minima	Constrained optimisation					
			Parallel			Orthogonal		
			Bridge	Top	Hollow	Bridge	Top	Hollow
Benzene	6	-10.9	-10.5	-10.2	-10.0	-0.9	-0.9	-1.3
Coronene	24	-15.3	-16.4	-15.5	-14.9	-6.4	-6.1	-7.6
Circumcoronene	54	-15.6	-18.5	-17.5	-16.7	-8.3	-8.2	-9.1
2×2-zigzag	16	-16.5	-15.3	-14.2	-12.9	-5.3	-5.1	-4.9
3×3-zigzag	30	-17.1	-16.8	-16.1	-15.7	-6.7	-6.9	\
4×4-zigzag	48	-17.0	-18.3	-17.4	-16.2	-8.1	-8.0	-8.6
2×2-armchair	20	-18.3	-15.6	-15.1	-14.0	-5.4	-5.3	-6.7
3×2-armchair	28	-18.5	-17.1	-16.3	-15.0	-7.2	-6.9	-7.5
5×3-armchair	66	-18.7	-18.6	-17.7	-16.5	-8.4	-8.3	-9.3
Extrapolated		-19.8	-19.8	-18.8	-18.0	-9.5	-9.5	-10.6

Table A.2: Size dependency of the ωB97X-D3/def2-TZVP interaction energies (in kJ mol^{-1}) of CO_2 on various graphene nanoflakes models. Size is expressed as the number of carbon atoms in the model.

| Model | Size | Global minima | Constrained optimisation | | | | | |
| | | | Parallel | | | Orthogonal | | |
			Bridge	Top	Hollow	Bridge	Top	Hollow
Benzene	6	-11.3	-10.9	-10.5	-10.3	-1.0	-1.0	-1.5
Coronene	24	-15.6	-15.6	-16.0	-13.6	-5.7	-5.5	-6.9
Circumcoronene	54	-16.9	-16.9	-15.7	-15.0	-7.3	-7.3	-8.1
2×2-zigzag	16	-15.0	-15.0	-13.6	-12.3	-4.8	-4.6	-4.6
3×3-zigzag	30	-16.1	-15.9	-14.7	-14.3	-6.0	-6.1	-7.2
4×4-zigzag	48	-16.9	-16.9	-15.7	-14.7	-7.2	-7.1	-7.7
2×2-armchair	20	-15.1	-15.0	-14.6	-13.2	-4.9	-4.8	-6.3
3×2-armchair	28	-16.1	-16.1	-15.1	-13.6	-6.5	-6.1	-6.9
5×3-armchair	66	-17.2	-17.2	-16.0	-14.6	-7.5	-7.4	-8.5
Extrapolated		-17.8	-16.6	-15.8	-8.4	-8.4	-9.5	-17.8

Table A.3: Size dependency of the ωB97X-D/def2-TZVP interaction energies (in kJ mol^{-1}) of CO_2 on various graphene nanoflakes models. Size is expressed as the number of carbon atoms in the model.

| Model | Size | Global minima | Constrained optimisation | | | | | |
| | | | Parallel | | | Orthogonal | | |
			Bridge	Top	Hollow	Bridge	Top	Hollow
Benzene	6	-10.6	-10.2	-9.8	-9.8	-1.2	-1.2	-1.8
Coronene	24	-15.7	-15.6	-14.6	-13.8	-6.6	-6.3	-7.8
Circumcoronene	54	-17.4	-17.3	-16.2	-15.7	-8.5	-8.4	-8.5
2×2-zigzag	16	-14.7	-14.7	-13.5	-12.2	-5.5	-5.3	-5.5
3×3-zigzag	30	-16.2	-16.0	-15.0	-14.6	-6.9	-7.0	-8.1
4×4-zigzag	48	-17.3	-17.3	-16.1	-15.3	-8.3	-8.2	-8.8
2×2-armchair	20	-15.0	-14.9	-14.5	-13.3	-5.6	-5.5	-7.1
3×2-armchair	28	-16.3	-16.3	-15.3	-13.9	-7.5	-7.0	-7.9
5×3-armchair	66	-17.7	-17.7	-16.5	-15.3	-8.7	-8.5	-9.7
Extrapolated		-18.6	-18.6	-17.4	-16.7	-9.7	-9.7	-10.4

Table A.4: Size dependency of the DSD-BLYP-D3/def2-TZVP interaction energies (in kJ mol^{-1}) of CO_2 on various graphene nanoflakes models. Size is expressed as the number of carbon atoms in the model.

| Model | Size | Global minima | Constrained optimisation | | | | | |
| | | | Parallel | | | Orthogonal | | |
			Bridge	Top	Hollow	Bridge	Top	Hollow
Benzene	6	-9.2	-8.8	-8.4	-8.4	-0.8	-0.8	-1.1
Coronene	24	-14.8	-14.7	-13.9	-13.3	-6.4	-6.2	-7.7
Circumcoronene	54	-17.1	-17.1	-16.2	-15.3	-8.7	-8.6	-9.7
2×2-zigzag	16	-13.5	-13.5	-12.5	-11.3	-5.2	-4.9	-4.9
3×3-zigzag	30	-15.4	-15.2	-14.6	-14.2	-6.9	-7.0	-8.7
4×4-zigzag	48	-17.0	-17.0	-16.5	-15.3	-8.5	-8.5	-9.2
2×2-armchair	20	-13.8	-13.7	-13.3	-12.2	-5.4	-5.2	-6.8
3×2-armchair	28	-15.6	-15.5	-14.7	-13.4	-7.8	-7.1	-7.8
5×3-armchair	66	-17.9	17.9	-16.7	-15.9	-10.1	-8.9	-10.1
Extrapolated		-18.9	-18.9	-18.0	-17.3	-10.8	-11.6	-18.9

A.2   Chapter 4

Table A.5: SAPT0/jun-cc-pVDZ//GFN2-xTB interaction energies (in kJ mol^{-1}).

GBM	Size	DNT	TNT
pristine graphene	1	-104.6	-110.6
	2	-117.4	-123.9
B,N-codoped graphene	1	-114.9	-120.5
	2	-130.3	-154.0
BH-doped graphene	1	-89.5	-97.4
	2	-101.6	-123.2
NH-doped graphene	1	-85.9	-82.8
	2	-96.5	-111.1
hBN	1	-58.4	-58.8
	2	-58.3	-60.3
rGO-HU,HO	1	-88.6	-102.0
	2	\	\
rGO-ST	1	-112.0	-125.3
	2	\	\

Table A.6: PBE-D3/def2-TZVP//GFN2-xTB interaction energies (in kJ mol^{-1}).

GBM	Size	DNT	TNT
pristine graphene	0	-16.2	-13.6
	1	-28.0	-13.2
	2	-30.5	-20.4
	3	-33.4	-20.3
B,N-codoped graphene	0	-28.5	-17.9
	1	-33.6	-17.4
	2	-35.7	-24.1
	3	-43.9	-33.4
BH-doped graphene	0	-31.7	-30.0
	1	-34.6	-21.3
	2	-34.8	-21.1
	3	-35.3	-30.7
NH-doped graphene	0	-3.6	-20.3
	1	-27.6	-16.3
	2	-29.7	-25.7
	3	-42.4	-26.9
hBN	0	-14.5	1.3
	1	-26.0	-10.8
	2	-26.0	-8.9
	3	-30.8	-16.1
rGO-HU,HO	0	-20.1	-25.7
	1	-32.5	-26.9
	2	-35.1	-23.8
	3	-31.7	-25.3
rGO-ST	0	-34.4	-42.0
	1	-47.7	-34.7
	2	-47.2	-6.6
	3	-31.0	-16.0

Table A.7: B3LYP-D3/def2-TZVP//GFN2-xTB interaction energies (in kJ mol^{-1}).

GBM	Size	DNT	TNT
pristine graphene	0	-30.77	-30.27
	1	-48.43	-35.15
	2	-52.07	-43.13
B,N-codoped graphene	0	-40.83	-29.88
	1	-52.90	-36.66
	2	-55.94	-44.92
BH-doped graphene	0	-38.86	-40.49
	1	-42.11	-28.33
	2	-47.09	-33.64
NH-doped graphene	0	4.13	-28.36
	1	-37.97	-21.91
	2	-40.79	-35.56
hBN	0	-28.52	-14.35
	1	-46.39	-33.05
	2	-46.19	-31.70
rGO-HU,HO	0	-27.87	-37.26
	1	-47.85	-45.39
	2	-53.05	-41.95
rGO-ST	0	-41.11	-57.12
	1	-61.38	-50.67
	2	-69.14	-30.08

Table A.8: Interaction energies of DNT with GBMs computed at different levels of theory in conjunction with B3LYP-D3/def2-TZVP (size 0) and PBE0-D3/def2-TZVP (size 1) geometries (in kJ mol^{-1}).

GBM	Size	PBE-D3/def2-TZVP	B3LYP-D3/def2-TZVP	SAPT0/jun-cc-pVDZ
pristine graphene	0		-78.4	-89.5
	1	-72.6	-85.9	-104.8
B,N-codoped graphene	0		-81.7	-94.3
	1	-78.7	-94.8	-114.3
BH-doped graphene	0		-72.6	-75.1
	1	-70.0	-80.1	-107.7
NH-doped graphene	0		-66.6	-72.3
	1	-70.7	-81.6	-80.1
hBN	0		-67.7	-55.9
	1	-60.9	-73.0	-73.7
rGO-HU,HO	0		-53.6	-56.3
	1	-75.7	-74.6	-111.2

Table A.9: GFN2-xTB interaction energies (in kJ mol^{-1}).

GBM	Size	DNT	TNT
pristine graphene	0	-65.95	-75.87
	1	-75.67	-89.90
	2	-78.15	-97.49
	3	-80.78	-101.97
	4	-81.96	-95.14
	5	-82.32	-101.89
	6	-82.95	-106.20
B,N-codoped graphene	0	-74.40	-86.30
	1	-81.30	-97.50
	2	-85.00	-115.20
	3	-98.90	-126.00
	4	-104.00	-134.60
	5	-103.60	-134.30
	6	-104.80	-136.50
BH-doped graphene	0	-49.87	-68.83
	1	-61.46	-82.21
	2	-70.37	-84.62
	3	-86.02	-111.67
	4	-85.19	-122.13
	5	-87.49	-122.80
	6	-89.14	-127.40
NH-doped graphene	0	-77.02	-96.40
	1	-82.14	-102.30
	2	-93.02	-119.20
	3	-98.22	-125.10
	4	-93.46	-127.50
	5	-95.54	-130.60
	6	-96.66	-131.10
hBN	0	-81.96	-98.63
	1	-101.44	-123.81
	2	-107.50	-132.17
	3	-113.86	-137.82
	4	-116.90	-141.93
	5	-120.86	-145.83
	6	-122.12	-147.23
rGO-HU,HO	0	-56.53	-75.03
	1	-71.07	-86.07
	2	-83.15	-93.69
	3	-86.49	-98.24
	4	-88.72	-101.08
	5	-88.76	-99.60
	6	-90.89	-103.10
rGO-ST	0	-72.20	-88.00
	1	-90.80	-98.40
	2	-97.40	-98.30
	3	-79.80	-100.10
	4	-87.00	-106.90
	5	-85.40	-106.10
	6	-89.14	-110.30

Table A.10: Periodic PBE-D3 interaction energies (in kJ mol^{-1}).

GBM	DNT	TNT
Pristine G	-66.1	-72.5
rGO-ST	-83.9	-89.4
rGO-HU-HO	-68.7	-73.0
B-doped	-74.6	-80.0
N-doped	-72.7	-64.1
B,N-codoped	-64.1	-65.0
hBN	-132.9	-136.5

Table A.11: PCM- UAKS/PBE0/6-31G(d)//PBE0-D3-RIJCOSX/def2-TZVP free energies of solvation in water at 25°C for size 1 models (in kJ mol^{-1}).

	GBM	ΔG
	pristine graphene	7.59
	rGO-ST	-1.24
	rGO-HU-HO	-0.26
DNT	BH-doped	8.47
	NH-doped	5.82
	B,N-codoped	8.66
	hBN	11.54
	pristine graphene	9.60
	rGO-ST	-1.91
	rGO-HU-HO	2.26
TNT	BH-doped	9.97
	NH-doped	8.45
	B,N-codoped	10.01
	hBN	14.99
	DNT	-4.86
	TNT	-5.37
	pristine graphene	-3.41
	rGO-HU-HO	-7.76
ISOLATED	B-N-codoped	-0.62
	rGO-ST	-6.53
	BH-doped	-4.14
	NH-doped	-5.75
	hBN	9.74

A.3   Chapter 5

Table A.12: Vertical EAs and IEs computed at the ωB97X-D/def2-TZVP level of theory (in eV). # atoms represents the number of non-hydrogen atoms in the nanoflake.

GBM	Size	# atoms	EA	IE
Pristine graphene	0	24	0.2	7.3
	1	54	1.1	6.5
	2	96	1.7	6.0
	3	150	2.2	5.6
Epoxide rGO	0	25	0.9	7.1
	1	55	1.5	6.4
	2	98	2.1	5.8
	3	153	2.3	5.7
BH-doped graphene	0	24	0.8	7.0
	1	54	1.6	6.3
	2	96	2.1	5.9
	3	150	2.2	5.4
1,1-B,N-codoped graphene	0	24	0.5	6.9
	1	54	1.3	6.3
	2	96	1.9	5.7
	3	150	2.2	5.5
NH-doped graphene	0	24	0.4	6.0
	1	54	1.2	5.8
	2	96	2.0	5.3
	3	150	2.2	5.1
PH-doped graphene	0	24	0.8	6.8
	1	54	1.4	6.2
	2	96	2.0	5.7
	3	150	2.4	5.4

Table A.13: Vertical IEs computed at different level of theory (in eV), with def2-TZVP basis set.

GBM	Size	PBE-D3BJ	TPSSh-D3BJ	B3LYP-D3BJ	MO6-2X
	0	7.0	7.0	7.1	7.5
Pristine graphene	1	6.1	6.1	6.2	6.6
	2	no convergence	5.6	5.7	6.1
	3	no convergence	5.3	5.3	5.8
	0	6.8	6.8	6.9	7.2
Epoxide rGO	1	6.1	6.0	6.1	6.6
	2	5.6	5.5	5.6	6.0
	3	5.3	5.3	5.4	5.9
	0	6.8	6.8	6.9	7.2
BH-doped graphene	1	6.0	6.0	6.1	6.5
	2	5.6	5.6	5.6	6.0
	3	5.2	5.2	5.3	5.7
	0	6.8	6.7	6.8	7.1
1,1-B,N-codoped graphene	1	6.0	6.0	6.1	6.5
	2	5.5	5.5	5.6	5.9
	3	5.2	5.2	5.3	5.7
	0	6.0	5.9	6.0	6.3
NH-doped graphene	1	5.6	5.6	5.7	6.0
	2	5.1	5.0	5.1	5.4
	3	5.0	4.9	5.0	5.3
	0	6.4	6.4	6.6	7.0
PH-doped graphene	1	5.9	5.9	6.0	6.4
	2	5.4	5.4	5.5	5.9
	3	5.2	5.1	5.2	5.6

Table A.14: Vertical EAs computed at different level of theory (in eV), with def2-TZVP basis set.

GBM	Size	PBE-D3BJ	TPSSh-D3BJ	B3LYP-D3BJ	MO6-2X
	0	0.6	0.4	0.4	0.3
Pristine graphene	1	1.6	1.4	1.4	1.3
	2	no convergence	2.0	2.0	2.0
	3	no convergence	2.4	2.4	2.4
	0	1.1	1.0	1.0	0.9
Epoxide rGO	1	1.8	1.7	1.7	1.6
	2	2.4	2.3	2.3	2.3
	3	2.7	2.5	2.5	2.5
	0	1.0	0.8	0.9	0.9
BH-doped graphene	1	1.8	1.7	1.7	1.7
	2	2.3	2.2	2.2	2.2
	3	2.6	2.5	2.5	2.5
	0	0.8	0.6	0.7	0.6
1,1-B,N-codoped graphene	1	1.7	1.5	1.5	1.4
	2	2.3	2.1	2.1	2.1
	3	2.6	2.5	2.4	2.4
	0	0.8	0.6	0.6	0.5
NH-doped graphene	1	1.6	1.4	1.4	1.4
	2	2.3	2.2	2.2	2.2
	3	2.6	2.5	2.4	2.4
	0	1.2	1.0	1.0	0.9
PH-doped graphene	1	1.8	1.6	1.6	1.6
	2	2.4	2.2	2.2	2.2
	3	2.7	2.6	2.6	2.6

Table A.15: ωB97X-D/def2-TZVP vertical and adiabatic EAs and IEs (in eV).

GBM	Size	Vertical EA	Adiabatic EA	Vertical IE	Adiabatic IE
Pristine graphene	0	0.2	0.3	7.3	7.2
	1	1.1	1.2	6.5	6.4
	2	1.7	1.8	6.0	5.9
	3	2.2	2.3	5.6	5.5
Epoxide rGO	0	0.9	1.2	7.1	6.9
	1	1.5	1.6	6.4	6.3
	2	2.1	2.2	5.8	5.7
	3	2.3	2.4	5.7	5.6
1,1-B,N-codoped graphene	0	0.5	0.7	6.9	6.7
	1	1.3	1.4	6.3	6.2
	2	1.9	2.0	5.7	5.7
	3	2.2	2.3	5.5	5.4
NH-doped graphene	0	0.4	0.6	6.0	5.8
	1	1.2	1.3	5.8	5.7
	2	2.0	2.1	5.3	5.1
	3	2.2	2.4	5.1	5.0

Table A.16: ωB97X-D/def2-TZVP HOMO and LUMO energies (in eV).

GBM	Size	HOMO	LUMO
Pristine graphene	0	-7.0	-0.6
	1	-6.5	-1.1
	2	-6.1	-1.7
	3	-5.9	-2.0
Epoxide rGO	0	-7.2	-0.7
	1	-6.6	-1.2
	2	-6.1	-1.8
	3	-6.0	-2.0
BH-doped graphene	0	-7.2	-0.6
	1	-6.6	-1.3
	2	-6.2	-1.7
	3	-5.8	-2.0
1,1-B,N-codoped graphene	0	-7.1	-0.4
	1	-6.5	-1.1
	2	-6.0	-1.7
	3	-5.8	-1.9
NH-doped graphene	0	-6.3	-0.2
	1	-6.1	-1.0
	2	-5.6	-1.7
	3	-5.5	-1.8
PH-doped graphene	0	-7.0	-0.6
	1	-6.5	-1.1
	2	-6.1	-1.7
	3	-5.9	-2.0